

**Al₂O₃ Thin Films: Relation between Structural Evolution, Mechanical
Properties, and Stability**

Von der Fakultät für Georessourcen und Materialtechnik
der Rheinisch -Westfälischen Technischen Hochschule Aachen

zur Erlangung des akademischen Grades eines
Doktors der Ingenieurwissenschaften

genehmigte Dissertation

vorgelegt von **M. Sc.**

Kaiyun Jiang

aus Zhejiang, China

Berichter: Univ.-Prof. Jochen M. Schneider, Ph.D.
Univ.-Prof. Dr.-Ing. Kirsten Bobzin

Tag der mündlichen Prüfung: 11. November 2011

Diese Dissertation ist auf den Internetseiten der Hochschulbibliothek online verfügbar

Materials Chemistry Dissertation

No.: 14 (2011)

Kaiyun Jiang

**Al₂O₃ Thin Films: Relation between Structural
Evolution, Mechanical Properties, and Stability**

Shaker Verlag
Aachen 2011

Bibliographic information published by the Deutsche Nationalbibliothek

The Deutsche Nationalbibliothek lists this publication in the Deutsche Nationalbibliografie; detailed bibliographic data are available in the Internet at <http://dnb.d-nb.de>.

Zugl.: D 82 (Diss. RWTH Aachen University, 2011)

Copyright Shaker Verlag 2011

All rights reserved. No part of this publication may be reproduced, stored in a retrieval system, or transmitted, in any form or by any means, electronic, mechanical, photocopying, recording or otherwise, without the prior permission of the publishers.

Printed in Germany.

ISBN 978-3-8440-0617-9

ISSN 1861-0595

Shaker Verlag GmbH • P.O. BOX 101818 • D-52018 Aachen

Phone: 0049/2407/9596-0 • Telefax: 0049/2407/9596-9

Internet: www.shaker.de • e-mail: info@shaker.de

Abstract

In this thesis the relation between structure evolution, mechanical properties, and stability was investigated for Al_2O_3 thin films. The existence of different polymorphs of this material offers a range of properties for applications, but also meets the process control challenges when the formation of phase pure material is desired. The aim of this work is to affect the phase structure evolution and the stability of vapor deposited alumina thin films, especially for the case of PECVD. This goal is achieved by experimental investigations of the PECVD process which show that $\alpha\text{-Al}_2\text{O}_3$ phase is obtained only at conditions with a low precursor ratio, a long pulse length and a high power density. These allow for more efficient precursor dissociation as suggested from plasma OES data as well as larger ion bombardment. When these conditions are not fulfilled, only $\gamma\text{-Al}_2\text{O}_3$ or $\alpha\text{-}\gamma$ -mixture is formed. Due to the use of chloridic precursor, it is found that less Cl content is incorporated in $\alpha\text{-Al}_2\text{O}_3$ films with < 1.0 at.% than in $\gamma\text{-Al}_2\text{O}_3$ films (~ 2.0 at.%). This observation is consistent with a high precursor dissociation and significant surface bombardment for the α -phase. Smooth and dense $\alpha\text{-Al}_2\text{O}_3$ films with negligible Cl incorporation and elastic properties similar to those of the bulk $\alpha\text{-Al}_2\text{O}_3$ are deposited at a growth temperature of 560 ± 10 °C, applying a novel generator that allows for the operation of a PECVD discharge at approx. 4 times larger power

density than those utilized conventionally. Up-scaling of a lab-scale PECVD process to an industrial reactor has been successfully conducted allowing the growth of crystalline alumina on large thixocasting tools at substrate temperatures of 590 °C. Steel thixocasting operations on the coated moulds indicate that coatings are intact after thixocasting. No evidence for adhesive or cohesive failure of the coatings was obtained, indicating efficient protecting of the tools during thixocasting.

Investigation of thermal stabilities of $\gamma\text{-Al}_2\text{O}_3$ films suggest that the $\gamma\text{-Al}_2\text{O}_3$ to $\alpha\text{-Al}_2\text{O}_3$ transformation in the PECVD films is faster and occurs at lower temperatures in comparison to the FCA films. This could be due to the porous structure of the PECVD grown films which enhance diffusion processes during the phase transformation. The porous structure of PECVD films further enables the oxidation of a TiAlN interlayer and the extrusion of TiO_2 towards the film surface due to large volume expansion from TiO_2 , leading to a complete failure of the coating system. The relative stability of $\gamma\text{-Al}_2\text{O}_3$ with respect to $\alpha\text{-Al}_2\text{O}_3$ with 2.5 at% of Si, Cr, Ti, Sc, and Y additives is also explored using *ab initio* calculations, indicating that Si stabilizes $\gamma\text{-Al}_2\text{O}_3$, while Cr stabilizes $\alpha\text{-Al}_2\text{O}_3$. This is explained by electronic structure changes induced by the alloying element. As Si is added, a bond length increase in $\alpha\text{-Al}_2\text{O}_3$ is observed, while strong and short Si-O bonds are formed in $\gamma\text{-Al}_2\text{O}_3$, consequently stabilizing this phase. On the other hand, Cr

additions induce a smaller bond length increase in $\alpha\text{-Al}_2\text{O}_3$ than in $\gamma\text{-Al}_2\text{O}_3$, therefore stabilizing the $\alpha\text{-Al}_2\text{O}_3$.

Zusammenfassung

Im Rahmen dieser Arbeit wurde die Korrelation zwischen der Strukturevolution, den mechanischen Eigenschaften und der Stabilität von Al_2O_3 -Dünnschichten untersucht. Aufgrund seiner Polymorphie besitzt Al_2O_3 vielfältige Eigenschaften für unterschiedlichste Anwendungen. Allerdings stellt das Auftreten der Polymorphen bei der Synthese von phasenreinem Al_2O_3 eine große Herausforderung hinsichtlich der Prozesssteuerung dar. Ziel dieser Arbeit ist die Beeinflussung der Strukturevolution und der Phasenstabilität von Aluminiumoxiddünnschichten die mittels PECVD abgeschieden wurden. Die hier durchgeführten experimentellen Untersuchungen zeigen, dass phasenreines $\alpha\text{-Al}_2\text{O}_3$ nur bei einer niedrigen Präkursorenpopulation, einer großen Pulslänge und einer hohen Leistungsdichte synthetisiert werden kann. Plasma-OES-Daten lassen darauf schließen, dass diese Bedingungen eine effizientere Präkursorendissoziation ermöglichen. Die Nichterfüllung dieser Bedingungen führt zur Bildung von $\gamma\text{-Al}_2\text{O}_3$ oder einer $\alpha\text{-}\gamma$ -Mischung. Die Verwendung eines chlorhaltigen Präkursors führt zur Cl-Inkorporation in den Al_2O_3 -Dünnschichten, wobei der Cl-Gehalt mit < 1.0 at.% in $\alpha\text{-Al}_2\text{O}_3$ - geringer ist als in $\gamma\text{-Al}_2\text{O}_3$ -Schichten (~ 2.0 at.%). Diese Beobachtung steht im Einklang mit einer hohen Präkursorendissoziation und einem starken Ionenbeschuss im Fall der α -Phase. Unter Verwendung eines neuartigen

Generators, der den Einsatz einer PECVD-Entladung mit einer annähernd vervierfachen Leistungsdichte im Vergleich zu konventionellen Generatoren ermöglicht, wurden bei Temperaturen von $560 \pm 10 \text{ }^\circ\text{C}$ glatte und dichte $\alpha\text{-Al}_2\text{O}_3$ -Schichten mit vernachlässigbarer Cl-Inkorporation und elastischen Eigenschaften ähnlich denen von massivem $\alpha\text{-Al}_2\text{O}_3$ abgeschieden. Eine Aufskalierung des Labor-PECVD-Prozesses auf einen industriellen Reaktor wurde erfolgreich durchgeführt. Dies ermöglicht die Abscheidung von kristallinem Aluminiumoxid bei Substrattemperaturen von $590 \text{ }^\circ\text{C}$ auf großen Thixoguss-Werkzeugen. Probeabgüsse von Stahlteilen mittels Thixoguss zeigten, dass die mittels PECVD aufgetragenen $\alpha\text{-Al}_2\text{O}_3$ -Schichten auf den Gussformen auch nach dem Abguss intakt waren. Es wurden weder Anzeichen für adhäsives noch für kohäsives Versagen der Beschichtung festgestellt. Somit stellen die mittels PECVD aufgetragenen $\alpha\text{-Al}_2\text{O}_3$ -Schichten einen effizienten Schutz der Werkzeuge während des Thixogusses dar.

Untersuchungen der thermischen Stabilität von $\gamma\text{-Al}_2\text{O}_3$ -Schichten weisen darauf hin, dass die $\gamma\text{-}\alpha$ -Umwandlung in PECVD-, verglichen mit FCA-Schichten, schneller und bei niedrigeren Temperaturen abläuft. Einen möglichen Grund hierfür könnte die poröse Struktur der PECVD-Schichten darstellen, die die Diffusionsprozesse während der Phasenumwandlung verstärkt. Ferner ermöglicht die poröse Al_2O_3 -Struktur die Oxidation der TiAlN-Zwischenschicht, was letztendlich aufgrund

der starken Volumenausdehnung des TiO_2 zu einem vollständigen Versagen des Beschichtungssystems führt. Die relative Stabilität des $\gamma\text{-Al}_2\text{O}_3$ in Bezug auf $\alpha\text{-Al}_2\text{O}_3$ mit je 2,5 at.% Si-, Cr-, Ti-, Sc- und Y-Zugaben wurde des weiteren mittels *ab initio*-Berechnungen untersucht. Es zeigte sich, dass Si $\gamma\text{-Al}_2\text{O}_3$ bzw. Cr $\alpha\text{-Al}_2\text{O}_3$ stabilisiert. Dieses Verhalten kann basierend auf legierungselementinduzierten Änderungen der elektronischen Struktur verstanden werden. Die Zugabe von Si führt zu einer Zunahme der Bindungslänge in $\alpha\text{-Al}_2\text{O}_3$, wohingegen in $\gamma\text{-Al}_2\text{O}_3$ starke, kurze Si-O-Bindungen gebildet werden und somit diese Phase stabilisiert wird. Andererseits induzieren Cr-Zugaben in $\alpha\text{-Al}_2\text{O}_3$, verglichen mit $\gamma\text{-Al}_2\text{O}_3$, eine geringere Bindungslängenzunahme und führen somit zu einer Stabilisierung des $\alpha\text{-Al}_2\text{O}_3$.

Preface

The work presented in this thesis is a part of the project funded by the Deutsche Forschungsgemeinschaft (DFG) within the collaborative research centre (TFB) 289 “Angewandte Formgebung im teilerstarrten Zustand und deren Werkzeuge” as well as under the project numbers Schn 735/14-2 and MA 1280/30-1 “Nanokristalline γ -Al₂O₃ Schichten”. It was carried out at Materials Chemistry, RWTH Aachen University, from August 2007 until October 2010 under the supervision of Prof. Jochen M. Schneider.

Publications

Papers as part of the thesis

PAPER I

K. Jiang, K. Sarakinos, S. Konstantinidis and J.M. Schneider, “*Low temperature synthesis of alpha-Al₂O₃ thin films using high-power plasma chemical vapor deposition*”, Journal of Physics D: Applied Physics 43 (32) 325202 (2010).

PAPER II

K. Jiang, D. Music, K. Sarakinos and J.M. Schneider, “*Ab initio study of effects of substitutional additives on the phase stability of γ -alumina*”, Journal of Physics: Condensed Matter, 22 505502 (2010).

PAPER III

K. Jiang, K. Sarakinos, A. Atiser, and J.M. Schneider, “*On the thermal stability of vapor deposited γ -Al₂O₃ thin films*”, submitted to International Journal of Materials Research.

PAPER IV

K. Jiang, S. Münstermann, H. J. Günther and J.M. Schneider, “*Up-scaling of a low temperature PACVD process for the deposition of α/γ -nanocrystalline alumina films on thixocasting tools*”, Steel Research International, 81 (7), 597-602 (2010).

PAPER V

S. Konstantinidis, K. Jiang, A. Roobroek, F. Renaux, and J.M. Schneider, “*Pulsed Plasma Enhanced Chemical Vapor Deposition of Alumina Thin Films, Influence of the Duty Cycle on Structure and Elastic Properties*”, Plasma Processes and Polymers, 8 (7), 651-657 (2011)

Papers related to the topics of the thesis

PAPER VI

R. Snyders, K. Jiang, D. Music, A. Reinholdt, S. Konstantinidis, T. Markus, and J.M. Schneider, “*Composition-constitution-morphology relationship of Al_2O_3 thin films deposited by plasma assisted chemical vapor deposition*”, Surface & Coating Technology, 204, 215-221 (2009).

PAPER VII

K. Sarakinos, D. Music, F. Nahif, K. Jiang, A. Braun, C. Zilkens, and J.M. Schneider; “*Ionized physical vapor deposited Al_2O_3 films: Does subplantation favor formation of $\alpha-Al_2O_3$?*”, Phys. Status Solidi (Rapid Research Letter), 4 (7), 154-156 (2010).

PAPER VIII

M. Bünck, A.B. Polaczek, K. Jiang, S. Münstermann, J.M. Schneider, K. Fickert, H. J. Günther, “*Thixocasting hand tools using Al₂O₃-coated steel and molybdenum dies*”, Steel Research International, 81 (7), 581-588 (2010).

Other papers

PAPER IX

J. Emmerlich, S. Mráz, R. Snyders, K. Jiang, and J.M. Schneider, “*The physical reason for the apparently low deposition rate during high-power pulsed magnetron sputtering*”, Vacuum, 82 (8) 867-870 (2008).

PAPER X

K. Sarakinos, D. Music, S. Mráz, M. to Baben, K. Jiang, F. Nahif, A. Braun, C. Zilkens, S. Konstantinidis, F. Munnik, and J.M. Schneider; “*On the phase formation of sputtered hafnium oxide and oxynitride films*”, Journal of Applied Physics, 108, 014904 (2010).

Acknowledgements

Foremost, I would like to express my sincere gratitude and appreciation to Professor Jochen Schneider for offering me this interesting research theme, invaluable guidance, and constant support.

Special thanks are dedicated to Kostas, and Stephanos for enormous ideas and discussion. Without your help I would not have been able to finish this work in such a short time. I am thankful to Denis for introducing the DFT theory to me. I am always motivated by your patience and encouragement. Besides, your great personality always brings smiles to me. My appreciation is also devoted to Mr. M. Kaiser and Mr. D. Horbach for your various technical supports, which helped to make my research more efficient. What I want to say to all the members of MCh (Tetsuya, Simon, Thomas G, Farwah, Adil, Florain, Moritz, Yan, Jens, Thomas R,) is thank you for bringing me so much enjoyable time in the last 4 years. You left me too many unforgettable moments in my life.

The present work is also greatly supported by the external partners that were involved in the some common research projects: Dr. A. Reinholdt, Ms. M. Ewering, and Ms. S, Cordes for work in the Gamma project as well as Matthias and Mr. Günther are appreciated for friendly collaboration and valuable discussion.

My most important gratitude is dedicated to my lovely wife Yuan, who has always

encouraged me and stood by me whenever and whatever obstacles were encountered.

TABLE OF CONTENTS

Abstract

Preface

Publications

Acknowledgments

1	INTRODUCTION & OUTLINE	1
2	STATE OF ART	5
2.1	Alumina (Al ₂ O ₃)	5
2.1.1	Structures and properties	5
2.1.2	Growth of alumina thin films	8
2.1.3	Stability of γ - and other metastable Al ₂ O ₃	10
2.2	Plasma thin film technology	12
2.2.1	Plasma-surface interactions	12
2.2.2	Plasma-Enhanced CVD	15
2.2.3	Other PVD approaches	16
3	METHODS OF RESEARCH.....	22
3.1	Film Synthesis by PECVD	22
3.1.1	Deposition system	22
3.1.2	Coating synthesis strategy	24
3.1.3	Coating synthesis procedures	25
3.2	Analytical Methods	27
3.2.1	Plasma characterization: Optical Emission Spectroscopy OES	27
3.2.2	X-Ray Diffraction (XRD)	29
3.2.3	Simultaneous Thermal Analysis (STA).....	31
3.2.4	Morphology and chemical composition	34
3.2.5	Elastic properties: Nanoindentation.....	35
3.3	Density Functional Theory (DFT)	36

4	PROCESS-PROPERTIES RELATION IN PECVD ALUMINA THIN FILM.....	42
4.1	Introduction.....	42
4.2	Influence of precursor ratio on the composition-constitution-morphology relationship of PECVD Al ₂ O ₃ thin films.....	43
4.2.1	On the plasma composition.....	43
4.2.2	On the film composition and phase constitutions	44
4.2.3	On the film morphology: role of chlorine content	47
4.3	Influence of the pulse width	53
4.3.1	On the plasma composition.....	53
4.3.2	On the film composition and phase constitutions	54
4.4	Low temperature synthesis of α-Al ₂ O ₃ films by high power plasma assisted chemical vapor deposition.....	58
4.4.1	Plasma characterization and modeling.....	58
4.4.2	Structure and elastic properties of films	62
4.5	Conclusions.....	66
5	ON THE STABILITY OF γ-ALUMINA	70
5.1	Introduction.....	70
5.2	On the high temperature stability of vapor deposited γ-Al ₂ O ₃ films.....	71
5.2.1	Thermal stability of the film/substrate system	71
5.2.2	Thermal stability of the γ-Al ₂ O ₃ film.....	78
5.2.3	Effect of morphology on the γ to α-Al ₂ O ₃ transformation.....	80
5.3	<i>Ab initio</i> study of effects of substitutional additives on the phase stability of γ-alumina.....	81
5.3.1	Crystal structure.....	81
5.3.2	Influence of additives on the phase stability.....	84
5.3.3	Influence of additives on the electronic structure	86
5.3.4	Influence of additives on the elastic properties	89
5.4	Conclusions.....	90
6	UP-SCALING OF A LOW TEMPERATURE PECVD PROCESS	94
6.1	Introduction	94
6.2	Industrial PECVD deposition system.....	95
6.3	Results and discussions.....	96
6.4	Conclusions.....	105
7	SUMMARY & FUTURE WORK.....	107

1 INTRODUCTION & OUTLINE

Although alumina (Al_2O_3), a traditional ceramic material, has been known and employed in different fields for centuries, it constitutes today an active research area in materials science. This is due to the interesting properties of Al_2O_3 , e.g. transparency over a wide range of wavelengths^{1,2}, electrical insulation with a band gap over 6 eV, mechanical advantages, and chemical inertness that makes it a promising candidate for different high-technology applications. Apart from the thermodynamically stable α -phase (hexagonal), Al_2O_3 also exhibits several other metastable polymorphs, e.g. γ -, θ -, δ - and κ -phases³⁻⁷. One specific alumina polymorph can be more efficient than another. For example, γ - and δ - Al_2O_3 polymorphs exhibit low surface energy and, therefore, are used in catalyst applications for which a large surface area is of importance^{8,9}. κ - Al_2O_3 is the phase showing the largest hardness as an alternative to α - Al_2O_3 ¹⁰. To understand the formation of these different phases and further control thereof is of great interest for the researchers.

α - Al_2O_3 films are used in high temperature applications, such as steel thixoforming^{11,12} and metal cutting^{3,4} due to their high thermal resistance (melting point $T_m = 2054 \text{ }^\circ\text{C}$) and superior mechanical properties (elastic modulus $E = 440 \text{ GPa}$ ¹³, hardness $H = 30 \text{ GPa}$ ¹³). The growth of this phase usually demands for extreme conditions to fulfil the high activation energy of the α -phase formation, i.e. high substrate temperatures in the excess of $1000 \text{ }^\circ\text{C}$ using thermal chemical vapor

deposition (CVD) or a large plasma density and a bias potential in the range of several hundred volts in plasma-enhanced physical (PEPVD) or chemical vapor deposition (PECVD). These requirements are often incompatible with heat sensitive substrates. Furthermore, using plasma assisted depositions, a decrease of the temperature required for the α -Al₂O₃ formation has been reported.^{14,15} However, the deposited films have been found to exhibit porosity^{14,15} and hence inferior elastic properties¹⁵ compared to bulk and CVD α -Al₂O₃. It is therefore a challenge to develop a synthesis strategy which allows for the growth of dense α -Al₂O₃ films at low substrate temperatures.

Another research direction is the expansion of the stability range of metastable phases such as γ - or κ -phase which possess similar or comparable mechanical properties as α -Al₂O₃.¹⁶ In general, the growth temperatures and discharge power input required for these metastable phases are much lower than those for the α -phase. Nevertheless, the metastable nature of these phases makes the stability an important issue in high temperature applications. The transition from the γ - to the α -phase is accompanied by a volume change of ~8% which, in the case of thin films attached on a substrate, causes mechanical stresses. The mechanical stresses in turn may result in crack formation and adhesive failure and thus deteriorate the performance of the film/substrate system at elevated temperatures. It is therefore evident that the understanding of the effect of the temperature on the phase stability of γ -Al₂O₃ films and their interactions with the underlying substrate is of key importance for designing novel γ -Al₂O₃/substrate systems with superior high temperature performance.

The objective of this thesis is to investigate the low-temperature growth of α -Al₂O₃ and high-temperature stability of metastable γ -Al₂O₃ in order to understand and

control the phase structure evolution and the stability of vapor deposited alumina thin films.

In chapter 2, the material system, synthesis techniques, as well as the thermal stability of metastable alumina is reviewed. In chapter 3, the methods of research are outlined. The deposition system as well as the analysis techniques for the plasma characterizations and film characterizations are presented. In the same chapter, a basic description of the theoretical tools used in this investigation using DFT theory is also provided. The main results and discussions are divided into three chapters: chapter 4 addresses the thin film synthesis / properties relationship, chapter 5 presents the investigation of the thermal stability of γ -Al₂O₃ both experimentally and theoretically, and chapter 6 presents the implementation of a lab-scale PECVD process to an industrial reactor with new perspectives. In chapter 7, a short summary of experimental and theoretical results of this thesis is presented and further research is proposed.

- ¹ M. Aguilar-Frutis, M. Garcia, and C. Falcony, *Applied Physics Letters* **72**, 1700-1702 (1998).
- ² B. Holm, R. Ahuja, Y. Yourdshahyan, B. Johansson, and B. I. Lundqvist, *Physical Review B* **59**, 12777 (1999).
- ³ J. M. Andersson, E. Wallin, and U. Helmersson *Thin Solid Films* **513**, 57 (2006).
- ⁴ M. Sridharan, M. Sillassen, J. Bottiger, J. Chevallier, and H. Birkedal, *Surface & Coatings Technology* **202**, 920-924 (2007).
- ⁵ S. K. Pradhan, P. J. Reucroft, and Y. K. Ko, *Surface & Coatings Technology* **176**, 382-384 (2004).
- ⁶ M. Delmas, D. Poquillon, Y. Kihn, and C. Vahlas, *Surface & Coatings Technology* **200**, 1413-1417 (2005).
- ⁷ A. Khanna and D. G. Bhat, *Surface & Coatings Technology* **201**, 168-173 (2006).

- ⁸ N. K. Nag, *Catalysis Letters* **24**, 37-46 (1994).
- ⁹ T. Takahashi, S. Tanaka, and M. Esashi, *J. Micromech. Microeng.* **16**, s206-s210 (2006).
- ¹⁰ M. Kathrein, W. Schintlmeister, W. Wallgram, and U. Schleinkofer, *Surface & Coatings Technology* **163**, 181-188 (2003).
- ¹¹ R. Kopp, *Steel Research International* **75**, 491-491 (2004).
- ¹² R. Kopp, H. Shimahara, J. M. Schneider, D. Kurapov, R. Telle, S. Munstermann, E. Lugscheider, K. Bobzin, and M. Maes, *Steel Research International* **75**, 569-576 (2004).
- ¹³ W. H. Gitzen, *Alumina as a Ceramic Material* (The American Ceramic Society, Columbus, 1970).
- ¹⁴ R. Snyders, K. Jiang, D. Music, S. Konstantinidis, T. Markus, A. Reinholdt, J. Mayer, and J. M. Schneider, *Surface & Coatings Technology* **204**, 215-221 (2009).
- ¹⁵ D. Kurapov, J. Reiss, D. H. Trinh, L. Hultman, and J. M. Schneider, *Journal of Vacuum Science & Technology A* **25**, 831-836 (2007).
- ¹⁶ C. Täschner, B. Ljungberg, V. Alfredsson, I. Endler, and A. Leonhardt, *Surface & Coatings Technology* **108-109**, 257-264 (1998).

2 STATE OF ART

In this chapter, the structure, properties and vapor phase based synthesis strategies of Al_2O_3 are reviewed.

2.1 Alumina (Al_2O_3)

2.1.1 Structures and properties

Alumina, Al_2O_3 , exhibits several polymorphs, such as κ -, γ -, δ -, θ - Al_2O_3 besides the thermodynamically stable α - Al_2O_3 (corundum)^{1,2}. These are all metastable phases, commonly also called “transition alumina” phases. The crystal structure of α - Al_2O_3 is the corundum structure which consists of a hexagonal close packed (hcp) O anion arrangement with Al cations filling up 2/3 of the central octahedral sites (see Fig. 2-1) with the lattice parameters $a = 0.476$ nm and $c = 1.299$ nm. These metastable phases are generally divided into two categories depending on the O anion arrangement: namely the structures based on a face centered cubic (fcc) O sublattice ($\dots ABCABC\dots$ stacking sequence) like γ -, η -, δ -, θ - Al_2O_3 and the structures based on an hcp O sublattice ($\dots ABAB\dots$ stacking sequence) such as κ - Al_2O_3 . Although most metastable aluminas have been utilized in industry for long time, the exact structure of some metastable alumina is still in controversy with respect to the Al cation position, etc. One of the examples is γ - Al_2O_3 , that is generally reported as a defect spinel $Al_{8/3}O_4$ with a space group $Fd\bar{3}m$ due to the close structural relationship with $MgAl_2O_4$ ³⁻⁵. The unit cell contains 32 oxygen ions on 32e Wyckoff fcc positions with $\dots ABCABC\dots$ stacking sequence, while 64/3 Al cations together with 8/3

vacancies occupy 8a tetrahedral and 16d octahedral positions (Fig. 2-2a). Recently, a tetragonal based structure (space group $I4_1/amd$), where Al cations occupy nonspinel positions, was also proposed (Fig. 2-2b)⁶⁻⁸. The tetragonal description suggested by Paglia *et al.* has been argued to agree better with neutron diffraction data⁷.

A brief summary on the structures and properties of common alumina polymorphs is presented in Table 2-1. Based on the standard formation enthalpy from calorimetric data, these phases consist of several metastable alumina phases by the sequence of γ , κ , δ , and θ . Compared to the α -phase, the metastable phases present lower densities.

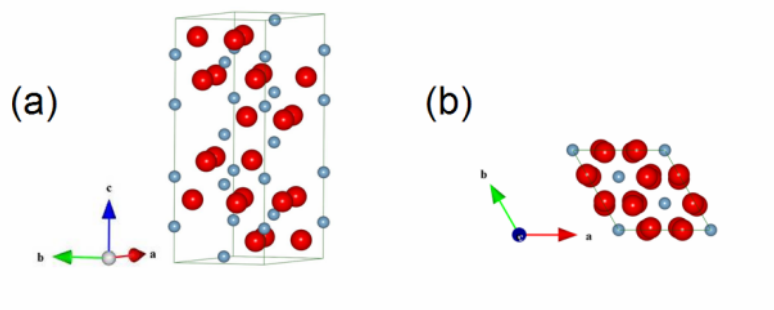


Fig. 2-1 Hexagonal unit cell of α - Al_2O_3 with (a) side view and (b) (0001) projection.

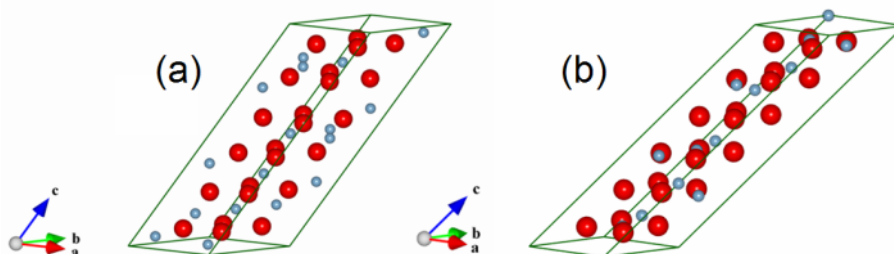


Fig. 2-2 Primitive cell of γ - Al_2O_3 based on the (a) spinel description suggested by Gutiérrez *et al.*⁴ and the (b) tetragonal hausmannite description

The choice of an alumina polymorph for a given application depends on their intrinsic properties. For example, the low surface energy of γ - and δ - Al_2O_3 ($< 1.0 \text{ J}\cdot\text{m}^{-2}$, while

2.04 J·m⁻² for α-Al₂O₃⁹) enables catalyst applications where a high surface area is of importance¹⁰⁻¹². On the other hand, it has extensively been demonstrated that α-Al₂O₃ coatings possess many desirable properties, such as extreme hardness, transparency over a wide range of wavelengths^{13,14}, high electrical resistivity, chemical inertness and thermal stability^{1,14,15}. A lot of attention has therefore been drawn to this material, which is suitable for coatings used in wear protection, for example in the cutting tool industry, or for the protection of die surfaces during the semi-solid processing of steel¹⁶⁻¹⁸ as well as for microelectronics and optics applications^{13,14}.

Tab. 2-1 Structures and properties of alumina polymorphs

Phases	Structure (arrangement of oxygen)	Space group ²	Density ¹⁹ [g/cm ³]	Young's modulus [GPa]	E-E _α ^(a) [meV/atom]
γ	fcc	Fd $\bar{3}$ m	3.65 – 3.67	253 - 275 ²⁰	46
κ	hcp	Pna2 ₁	3.98	362 ²¹	32
δ	fcc	P $\bar{4}$ m2	3.60 - 3.65		24
θ	fcc	C2/m	3.60 - 3.65		< 24
α	hcp	R- $\bar{3}$ c	3.96 - 3.99	409 - 441 ¹	

(a) Calorimetric measurement of enthalpy difference between metastable alumina and α alumina in eV/atom extracted from Ref.1.

2.1.2 Growth of alumina thin films

Al₂O₃ thin films are usually obtained by chemical vapor deposition (CVD) or physical vapor deposition (PVD), where a vapor is deposited by condensation or chemical

reaction to form a solid material on the substrate surface. Some plasma based vapor deposition techniques are introduced in the following section of this chapter.

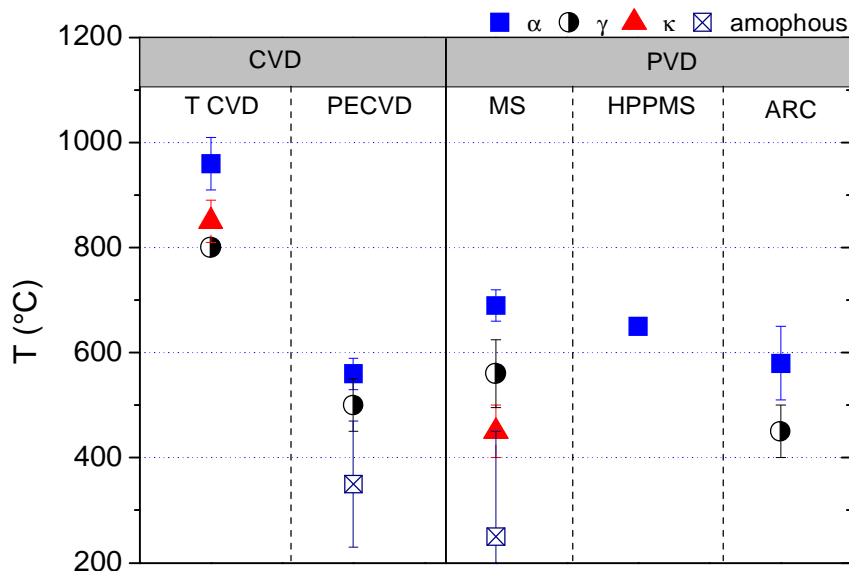
2.1.2.1 Growth of α -Al₂O₃ films

In the industrial practice α -Al₂O₃ is grown by thermal chemical vapor deposition (CVD). A common feature of CVD grown α -Al₂O₃ is that substrate temperatures of more than 1000 °C are necessary to provide the film forming species with the energy required for α -Al₂O₃ phase formation²². These high deposition temperatures may cause the build up of thermal stresses as well as interface reactions²² and may thus lead to poor adhesion and thermally induced crack formation and growth²³. Furthermore, the metallurgical properties of the substrate material may be altered by substrate heating, severely limiting the choice of substrate materials. An alternative way to provide energy to the growing film and decreasing the temperature limit for the deposition of α -Al₂O₃ is by bombardment of energetic species which are available in plasma based physical and chemical vapor deposition techniques. For instance, Wallin *et al.*²⁴ demonstrated the deposition of α -Al₂O₃ on hard metal substrates at a temperature of about 650 °C using high power pulsed magnetron sputtering, while Takamura *et al.*²⁵ obtained this phase at a temperature of ~ 500 °C employing filtered cathodic arc with a large substrate bias of 200 V. Jin *et al.*²⁶ reduced the temperature limit further for the growth of α -Al₂O₃ down to 280 °C by depositing Al₂O₃ films on a Cr₂O₃ seed layer by RF magnetron sputtering. Kyrlov *et al.*²⁷ demonstrated the growth of α -Al₂O₃ at 560 °C by plasma enhanced chemical vapor deposition (PECVD).

2.1.2.2 Growth of metastable Al₂O₃ films

Deposition at lower temperatures and/or smaller ion energy leads to the growth of various metastable phases²⁸⁻³², i.e. κ -, γ -, θ -Al₂O₃. Andersson *et al.* reported that in

reactive sputtering of alumina films, the γ -phase was formed at lower O_2 pressure or higher total pressure. This can be understood by low energy of the depositing species and low energetic bombardment of the growth surface.²⁸ Temperature is usually the crucial parameter to control the phase formation. As the growth temperature is increased, a clear trend of the phase evaluation from amorphous (350-550 °C) films to crystalline ones consisting of κ - and γ - Al_2O_3 (750-950 °C) and crystalline κ - Al_2O_3 films at 950 °C were obtained in the case of MOCVD films³¹. Similar formation sequences at increased temperatures were reported for other deposition techniques. Fig. 2-3 summarizes selected reported data on the growth temperatures of different Al_2O_3 polymorphs using various vapor deposition techniques. Besides the ion energy and the growth temperature the phase formation is also influenced by the presence of the substrates such as Cr_2O_3 seed layers which enable the growth of α - Al_2O_3 at 280°C^{26,33}.



T CVD : thermal CVD (Ruppi *et al.*^{34,35}, Kornmann *et al.*³⁶, Chatfield *et al.*³⁷)
 PECVD : (Finka *et al.*³⁸, Kyrylov *et al.*²⁷, Lin *et al.*³⁹, Täschner *et al.*⁴⁰)
 MS : magnetron sputtering (Zywitzki *et al.*^{41,42}, Schneider *et al.*^{43,44})
 HPPMS : high power pulsed magnetron sputtering (Wallin *et al.*²⁴)
 ARC : cathodic arc (Yanada *et al.*²⁵, Brill *et al.*⁴⁵, Sarakinos *et al.*⁴⁶)

Fig. 2-3 Synthesis methods and growth temperatures for alumina polymorphs

2.1.3 Stability of γ - and other metastable Al_2O_3

2.1.3.1 Experimental investigation

Most phase stability studies of $\gamma\text{-Al}_2\text{O}_3$ have been performed for powders and report indirect $\gamma \rightarrow \delta \rightarrow \theta \rightarrow \alpha\text{-Al}_2\text{O}_3$ ^{2,47,48} transformations. Wefers *et al.*⁴⁹ showed that $\gamma\text{-Al}_2\text{O}_3$ powder transforms to $\delta\text{-Al}_2\text{O}_3$ at a temperature of 750 °C, $\delta\text{-}$ to $\theta\text{-Al}_2\text{O}_3$ at a temperature of 930 °C, while the $\theta\text{-}$ to $\alpha\text{-Al}_2\text{O}_3$ transformation occurred at 1050 °C. McHale *et al.*⁹ showed that the powder morphology is decisive for the stability of the $\gamma\text{-Al}_2\text{O}_3$ phase. In particular, it was demonstrated that $\gamma\text{-Al}_2\text{O}_3$ exhibits a surface energy of $0.79 \text{ J}\cdot\text{m}^{-2}$ compared to $\alpha\text{-Al}_2\text{O}_3$ with a value of $2.04 \text{ J}\cdot\text{m}^{-2}$ ⁹. As a consequence, when the specific surface area of the powder (which is determined by the powder particle size) exceeds a certain critical value, the contribution of the surface energy governs the contribution of the bulk energy to the total energy and thus $\gamma\text{-Al}_2\text{O}_3$ becomes thermodynamically stable. Another factor that affects the phase stability is the composition of the $\gamma\text{-Al}_2\text{O}_3$ powder. For instance, the doping of cation sites by La in a $\gamma\text{-Al}_2\text{O}_3$ powder has been found to increase the $\gamma \rightarrow \alpha$ transformation temperature by 150 °C⁵⁰. In the case of $\gamma\text{-Al}_2\text{O}_3$ films direct $\gamma \rightarrow \alpha$ transformation at temperatures higher than those for the powders are commonly observed^{51,52}. Trinh *et al.*⁵¹ showed that $\gamma\text{-Al}_2\text{O}_3$ films deposited on cemented carbide cutting inserts by bipolar pulsed dual magnetron sputtering transformed into $\alpha\text{-Al}_2\text{O}_3$ at temperatures ranging from 950 to 975 °C, while radio frequency magnetron sputtered $\gamma\text{-Al}_2\text{O}_3$ films were found to transform into $\alpha\text{-Al}_2\text{O}_3$ after annealing at 1200 °C for 2 hours⁵². Bobzin *et al.*⁵³ showed that $\gamma\text{-Al}_2\text{O}_3$ films on $\text{Ti}_{0.33}\text{Al}_{0.67}\text{N}$ coated cutting inserts exhibited a stable phase composition up to 900°C in air without significant change of crystallite size and hardness. A $\gamma \rightarrow \alpha\text{-Al}_2\text{O}_3$ transformation was observed at 1000 °C and the authors suggested that the transformation could be

initiated at the $\text{Ti}_{0.33}\text{Al}_{0.67}\text{N}/\text{Al}_2\text{O}_3$ interface⁵³. Eldmayr *et al.*⁵⁴ studied the phase stability of reactively sputtered $\gamma\text{-Al}_2\text{O}_3$ films deposited on Si substrates and found that $\gamma\text{-Al}_2\text{O}_3$ transforms at a temperature of 1000 °C. Other studies have shown that doping of electron beam evaporated $\gamma\text{-Al}_2\text{O}_3$ films by Y, Er, and Cr affects the transformation kinetics⁵⁵, resulting in a lower transformation velocity. Y and Er decrease the transformation velocity, while Cr promotes the transformation to $\alpha\text{-Al}_2\text{O}_3$ ⁵⁵. However, systematic studies regarding the effects of additives on the stability of $\gamma\text{-Al}_2\text{O}_3$ have not yet been conducted and the mechanisms that determine the phase stability especially at the atomic scale of $\gamma\text{-Al}_2\text{O}_3$ are far from being understood. On the other hand, studies of additives affecting the phase stability of other metastable polymorphs have been reported. Mekasuwandumrong *et al.* reported that the Si additions in $\chi\text{-Al}_2\text{O}_3$ caused an increase of 100 K for the $\chi \rightarrow \alpha\text{-Al}_2\text{O}_3$ transformation⁵⁶. The authors suggested that the incorporation of Si in the alumina lattice supplies an extra charge which in turn inhibits the nucleation of the α -phase⁵⁶. The presence of Ti or B in the chemical vapor deposited $\kappa\text{-Al}_2\text{O}_3$ thin films was found to retard the $\kappa \rightarrow \alpha\text{-Al}_2\text{O}_3$ transformation and to improve its wear resistance⁵⁷.

2.1.3.1 Theoretical investigation

Ab initio studies on $\theta\text{-Al}_2\text{O}_3$, structurally similar to γ , revealed that Mo, As, W, Sc, Si, N, S, Cu, and Co influence the stability of the θ -phase^{58,59}. With ~5 at.% of additives at the substitutional sites of either Al cations or O anions, the total energy of the doped and undoped alumina were calculated. It was reported that Mo, As, W, Sc, Si, N, and S decrease the total energy difference between α - and $\theta\text{-Al}_2\text{O}_3$ and therefore increase the relative stability of the θ -phase^{58,59}. In contrast, Cu and Co increase the energy difference thus stabilizing the α -phase^{58,59}. However, the role of Cr as alloying agent remains illusive since Cr appears to stabilize the α -phase in Ref. 52, while it is reported to stabilize the θ -phase in Ref. 53.

2.2 Plasma thin film technology

A plasma is an ionized gaseous entirety which consists of equal concentrations of positively and negatively charged species, and different concentrations of ground-state and excited species⁶⁰. Often, in industrial applications, non-equilibrium plasmas such as the ones produced by glow discharges are used. Glow discharge plasmas are activated using external electrical fields and sometimes additional magnetic fields to accelerate the electrons. This gives rise to collisions with the gas atoms or molecules (excitation, ionization, dissociation of the gas particles...). The source of the first accelerated electron may be from the omnipresent cosmic radiation. These plasmas do not require high temperatures of the gas particles and are therefore called "cold plasma". Glow discharges are widely utilized in thin film technology for vapor generation and/or modification due to the energy distribution function of the particles striking the film surface. For example, in PECVD processes, the temperature for corresponding reactions can be dramatically decreased in a glow discharge media compared to that of thermal CVD. In magnetron sputtering, the glow discharge offers ions which are accelerated to the cathode and further knocked out target atoms for film deposition.

2.2.1 Plasma-surface interactions

The energetic particle bombardment of the growing film surface plays a significant role during the film growth process. If a solid is placed into a glow discharge, both ions and electrons would hit the surface. Nevertheless, electrons can move significantly faster than ions. For example, in an Ar discharge, the speed of electrons is about 7×10^4 times higher than that of Ar^+ . Therefore, the plasma charges up so that an electric field opposes electron escape and reduces the total electric current to zero. An intermediate region, the so-called sheath, is thus formed. As shown in Fig.

2-4, the plasma potential is more positive than the ground potential due to the formation of the sheath.

Due to the high potential drop in the cathode sheath positive ions can acquire high energy (see Fig. 2-4). The maximum ion energy is expected to be $E_{i_{max}} = e \cdot (V_p - V_{dc})$ with e as the electron charge. The actual ion energy (E_i) can be significantly lower than $E_{i_{max}}$ in a collisional plasma sheath, depending on the ratio of the mean free path of the ions to the sheath thickness⁶¹. Actually in a collisional cathode sheath, the energetic ions can collide with other heavy particles (Ar, precursor molecules, ...) which lead to a decrease of the energy. The energy of the ions arriving at the substrate can be described by the ion energy distribution function (IEDF).

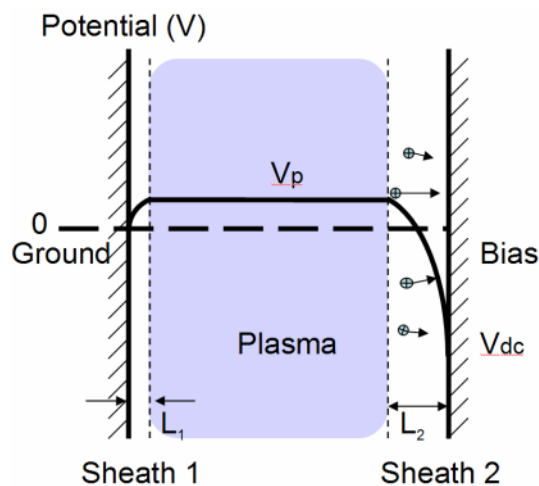


Fig. 2-4 Spatial distribution of the electrical potential in the plasma and sheath

In order to simplify the question, it is assumed that the average energy of the ions, as they reach the substrate, is proportional to V_{dc} divided by the number of collisions they had in the sheath. As already mentioned, the number of collisions with atoms or molecules is proportional to the thickness of the cathode sheath and inversely proportional to the mean free path of ions⁶². It can be described by the following relation:

$$\bar{E} = \frac{2}{n \times s \times L_s} \times V_{dc} , \quad (\text{eq. 2-1})$$

where \bar{E} is the average ion energy, and n , s , and L_s represent the ion density, the collision cross section and the sheath width, respectively.

Depending on the mass, flux, energy and angle of incidence, energetic ions or energetic atoms bombard the substrate surface and can cause numerous effects such as emission of secondary electrons, photon, sputtering, reflection, physical implantations, and lattice defects generation. If the ion energy is high enough, ion implantation may be responsible for the incorporation of impurities into the growing film⁶³.

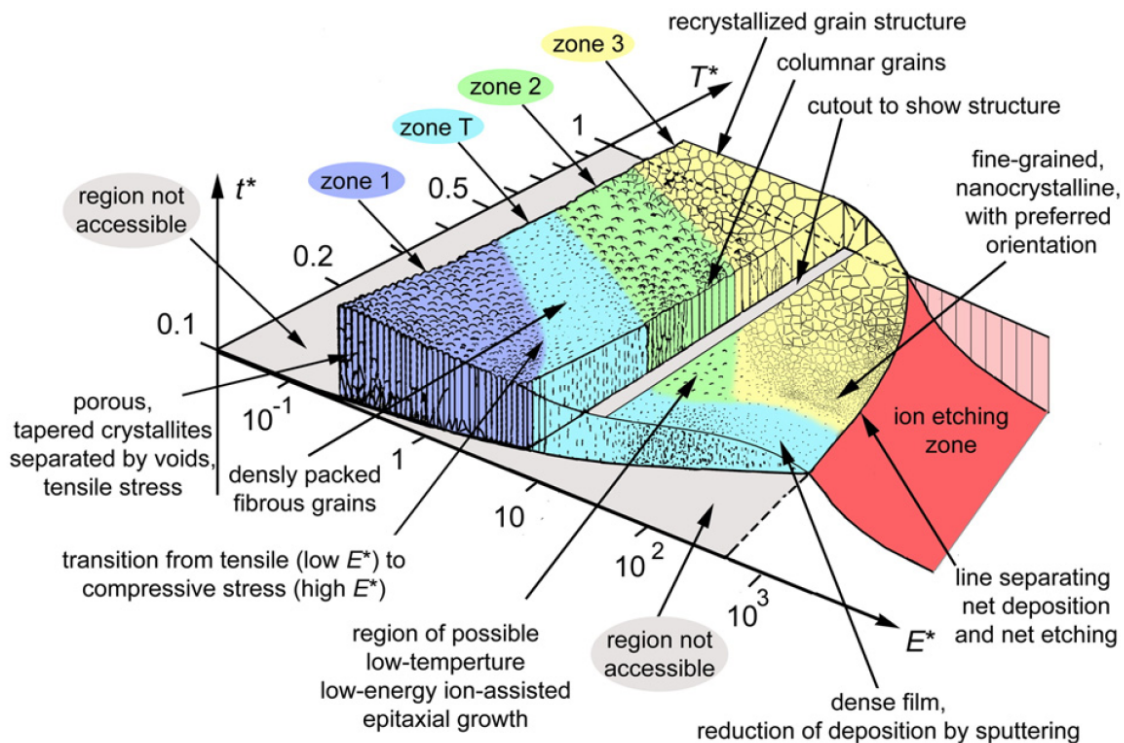


Fig. 2-5 Structure zone diagram applicable to energetic deposition. The axes are the generalized temperature T^* , the normalized energy flux E^* , and the net thickness t^* ⁶⁴.

The influences of energetic ion bombardment on the microstructure evolution of the growing film can be illustrated by an extended Structure Zone Model (SZM) proposed by Anders⁶⁴. In the previously reported SZM⁶⁵ the different microstructure zones are

generally determined by the normalized temperature T^* , which is the ratio between substrate temperature and melting temperature of the film material. With increasing T^* , transitions from fibrous grain with voided boundaries to dense column and ultimately to equiaxed grains are observed. Taking the energy of species into account, this model was modified by introducing of an additional process parameter namely the total pressure⁶⁶. Recently, Anders⁶⁴ further generalized the SZM (Fig. 2-5) by considering another axes of normalized energy flux E^* . The E^* brought by particles to the surface will ultimately contribute to broad, non-local heating of the film and thereby shift the zone boundaries to higher homologous temperatures⁶⁴. Ion etching is also predicted at even higher E^* .

2.2.2 Plasma-enhanced CVD

Using plasmas, gaseous species are highly activated (molecules, charged particles, ...) and may hence overcome the activation energy for the phase formation at growing film surface at considerably lower temperatures than during conventional thermal CVD⁶⁷. However, the effect of plasma enhancement on the CVD process is difficult to evaluate quantitatively. Actually, the reactants undergo numerous and complex interactions within the plasma which are rather complicated to describe. During the process, the precursor molecules undergo electron impact dissociation and excitation and consequently become highly reactive. They are subsequently transported to the substrate surface via gas phase diffusion. Adsorbed species may migrate on the surface as a consequent excitation and/or energetic particles bombardment and form finally the solid reaction product at the growing film surface. A schematic illustration is presented in Fig. 2-6.

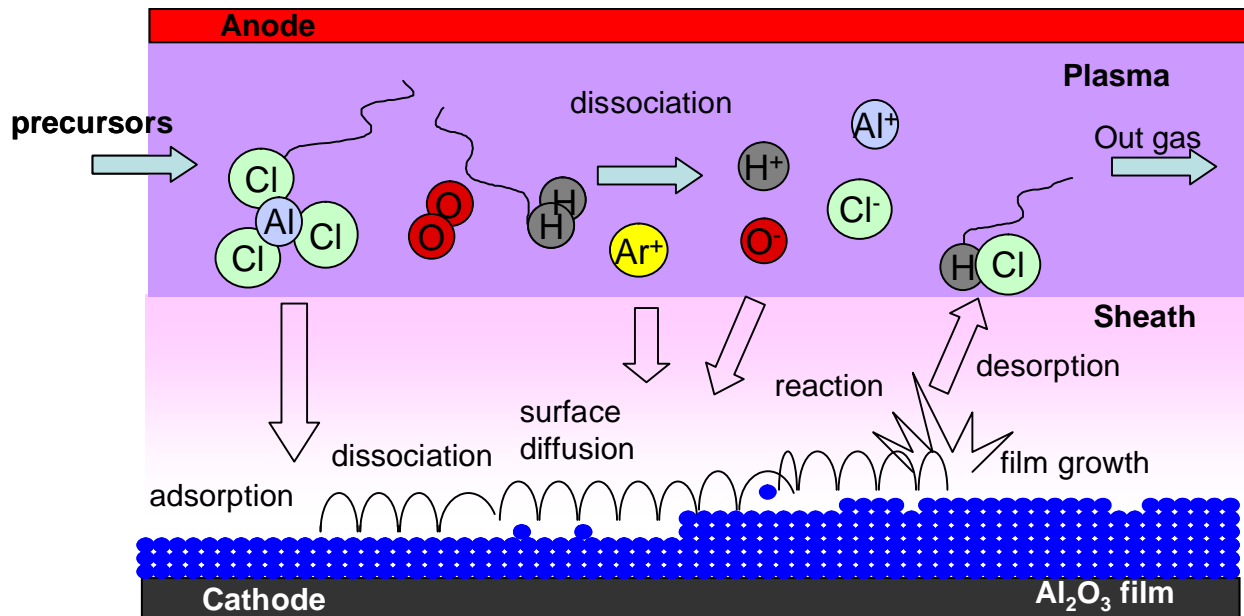


Fig. 2-6 Schemes of PECVD process of Al_2O_3 from $\text{AlCl}_3 + \text{O}_2$ precursors

In the currently employed PECVD system, a pulsed DC source was chosen to sustain the glow discharge. By a periodically switching negative potential on the two electrodes, the accumulated positive charges attracted on the cathode are neutralized by electrons drawn from the plasma. Since the substrate was located on the bottom cathode, the ion-irradiation phase of the growth process corresponds to the negative pulse. The latter is followed by a positive pulse in which the growing films are under electrons bombardment and, as a consequence, where the insulating layer is discharged. Therefore, arc-free deposition of insulating compounds is obtained.

2.2.3 Other synthesis approaches

Magnetron sputtering deposition is one of most used plasma based physical vapor deposition processes. In sputtering, the vapor is formed by energetic particles bombardment of a target material, causing ejection of atoms and clusters from the target surface. These predominately neutral particles are transported from the target region to the substrate and are deposited on the substrate forming a thin film. A

typical metallic sputtering process has an ionization degree of a few percents⁶⁸. The composition of the film is usually identical to the target material. An isolating compound thin film can be deposited by RF sputtering or by reactive sputtering, where additional gas that is reactive to the elemental targets, is introduced. Normally the reactive gas may be in the molecular state (e.g., N₂, O₂) or may be activated to form a more chemically reactive or more easily adsorbed species. For instance alumina films can be formed by sputtering of an aluminum target in the presence of oxygen and argon. One typical challenge of reactive sputtering is the “poisoning” of the sputtering target. This is due to the reaction between the reactive gas and the target surface. The formation of an insulating compound layer on the target surface is the result which may cause subsequent arcing. Hence, sophisticated process control strategies are required to enable stable processing.

Cathodic arc deposition is widely used in industry due to its high deposition rate and large degree of ionization compared to sputtering. The plasma is formed in so called cathode spots. The arc discharge is characterized by low voltage and high current, where the generated plasma can exhibit an ionization degree up to 100%⁶⁹. Nevertheless, a common drawback of cathodic arc deposition is the generation and presence of droplets originating from the cathode. These particles may in turn deteriorate the quality of the as deposited films. Magnetic filters are employed to reduce the particles⁷⁰, since only ions are able to follow the electron trajectory that is defined by the magnetic field arrangement, while the expansion direction of the neutral and macro particles is unaffected by the magnetic field.

- 1 W. H. Gitzen, *Alumina as a Ceramic Material* (The American Ceramic Society, Columbus, 1970).
- 2 I. Levin and D. Brandon, *Journal of the American Ceramic Society* **81**, 1995-2012 (1998).
- 3 K. E. Sickafus and R. Hughes, *Journal of the American Ceramic Society* **82**, 3277-3278 (1999).
- 4 G. Gutiérrez, A. Taga, and B. Johansson, *Physical Review B* **65**, 012101 (2002).
- 5 C. Wolverton and K. C. Hass, *Physical Review B* **63**, 024102 (2001).
- 6 G. Paglia, E. S. Bozin, and S. J. L. Billinge, *Chemistry of Materials* **18**, 3242-3248 (2006).
- 7 G. Paglia, A. L. Rohl, C. E. Buckley, and J. D. Gale, *Physical Review B* **71**, 224115 (2005).
- 8 J. M. Knaup, C. Kohler, T. Frauenheim, A. T. Blumenau, M. Amkreutz, P. Schiffels, B. Schneider, and O. D. Hennemann, *Journal of Physical Chemistry B* **110**, 20460-20468 (2006).
- 9 J. M. McHale, A. Auroux, A. J. Perrotta, and A. Navrotsky, *Science* **277**, 788-791 (1997).
- 10 Z. Wu, H. S. Kim, P. C. Stair, S. Rugmini, and S. D. Jackson, *Journal of Physical Chemistry B* **109**, 2793 (2005).
- 11 T. Takahashi, S. Tanaka, and M. Esashi, *J. Micromech. Microeng.* **16**, s206-s210 (2006).
- 12 N. K. Nag, *Catalysis Letters* **24**, 37-46 (1994).
- 13 M. Aguilar-Frutis, M. Garcia, and C. Falcony, *Applied Physics Letters* **72**, 1700-1702 (1998).
- 14 B. Holm, R. Ahuja, Y. Yourdshahyan, B. Johansson, and B. I. Lundqvist, *Physical Review B* **59**, 12777 (1999).
- 15 B. M. Kramer and P. K. Judd, *Journal of Vacuum Science & Technology A* **3**, 2439-2444 (1985).
- 16 R. Kopp, H. Shimahara, J. M. Schneider, D. Kurapov, R. Telle, S. Munstermann, E. Lugscheider, K. Bobzin, and M. Maes, *Steel Research International* **75**, 569-576 (2004).
- 17 D. Kurapov and J. M. Schneider, *Steel Research International* **75**, 577-580 (2004).

- 18 K. Jiang, S. Münstermann, H.-J. Günther, and J. M. Schneider, *Steel Research International*, Accepted (2010).
- 19 T. Yokokawa and O. J. Kleppa, *Journal of Physical Chemistry* **68**, 3246 (1964).
- 20 M. R. Gallas and G. J. Piermarini, *Journal of the American Ceramic Society* **77**, 2917-2920 (1994).
- 21 R. A. B. Holm, Y. Yourdshahyan, B. Johansson, B. I. Lundqvist, *Phys. Rev. B* **59**, 12777 (1999).
- 22 J. Müller, M. Schierling, E. Zimmermann, and D. Neuschütz, *Surface & Coatings Technology* **120-121**, 16-21 (1999).
- 23 T. Göbel, S. Menzel, M. Hecker, W. Bruckner, K. Wetzig, and C. Genzel, *Surface & Coatings Technology* **142-144**, 861-867 (2001).
- 24 E. Wallin, T. I. Selinder, M. Elfving, and U. Helmersson, *Epl* **82**, 36002 (2008).
- 25 Y. Yamada-Takamura, F. Koch, H. Maier, and H. Bolt, *Surface & Coatings Technology* **142-144**, 260-264 (2001).
- 26 P. Jin, G. Xu, M. Tazawa, K. Yoshimura, D. Music, J. Alami, and U. Helmersson, *Journal of Vacuum Science & Technology A* **20**, 2134-2136 (2002).
- 27 O. Kyrilov, D. Kurapov, and J. M. Schneider, *Applied Physics A* **80**, 1657-1660 (2005).
- 28 J. M. Andersson, E. Wallin, U. Helmersson, U. Kreissig, and E. P. Munger, *Thin Solid Films* **513**, 57-59 (2006).
- 29 M. Delmas, D. Poquillon, Y. Kihn, and C. Vahlas, *Surface & Coatings Technology* **200**, 1413-1417 (2005).
- 30 A. Khanna and D. G. Bhat, *Surface & Coatings Technology* **201**, 168-173 (2006).
- 31 S. K. Pradhan, P. J. Reucroft, and Y. K. Ko, *Surface & Coatings Technology* **176**, 382-384 (2004).
- 32 M. Sridharan, M. Sillassen, J. Bottiger, J. Chevallier, and H. Birkedal, *Surface & Coatings Technology* **202**, 920-924 (2007).
- 33 J. M. Andersson, Z. Czigany, P. Jin, and U. Helmersson, *Journal of Vacuum Science & Technology A* **22**, 117-121 (2004).
- 34 S. Rупpi and A. Larsson, *Thin Solid Films* **388**, 50 (2001).
- 35 S. Rупpi, *International Journal of Refractory Metals & Hard Materials* **23**, 306-316 (2005).

- 36 M. Kornmann, H. Schachner, R. Funk, and B. Lux, *Journal of Crystal Growth* **28** (1975).
- 37 C. Chatfield, J. N. Lindstrom, and M. E. Sjöstrand, *Journal De Physique* **50**, 377-387 (1989).
- 38 M. Finka, C. Lfckerb, J. Laimera, C. Mittererb, and H. Stoeri, *Surface & Coatings Technology* **188–189**, 281–286 (2004).
- 39 C. H. Lin, H. L. Wang, and M. H. Hon, *Surface & Coatings Technology* **90**, 102-106 (1997).
- 40 C. Täschner, B. Ljungberg, V. Alfredsson, I. Endler, and A. Leonhardt, *Surface & Coatings Technology* **108-109**, 257-264 (1998).
- 41 O. Zywitzki and G. Hoetzsch, *Surface & Coatings Technology* **94-5**, 303-308 (1997).
- 42 O. Zywitzki and G. Hoetzsch, *Surface & Coatings Technology* **86-7**, 640-647 (1996).
- 43 J. M. Schneider and A. M. W.D. Sproul, *Surface & Coatings Technology* **94-95**, 179 (1997).
- 44 J. M. Schneider, W. D. Sproul, and A. Matthews, *Surface & Coatings Technology* **98 (1/3)**, 1473 (1998).
- 45 R. Brill, F. Koch, J. Mazurelle, D. Levchuk, M. Balden, Y. Yamada-Takamura, H. Maier, and H. Bolt, *Surface & Coatings Technology* **174**, 606-610 (2003).
- 46 K. Sarakinos, D. Music, F. Nahif, K. Jiang, A. Braun, C. Zilkens, and J. M. Schneider, *physica status solidi (RRL) - Rapid Research Letters* **4**, 154-156 (2010).
- 47 C. C. Stephen, *Journal of the American Ceramic Society* **66**, 495-500 (1983).
- 48 R. S. Zhou and R. L. Snyder, *Acta Crystallographica, Section B: Structural Science* **47**, 617-630 (1991).
- 49 K. Wefers and C. Misra, *Alcoa Laboratories*, Vol. No. 19 (PA, USA, Pittsburg, 1987).
- 50 S. W. Wang, A. Y. Borisevich, S. N. Rashkeev, M. V. Glazoff, K. Sohlberg, S. J. Pennycook, and S. T. Pantelides, *Nature Materials* **3**, 143-146 (2004).
- 51 D. H. Trinh, K. Back, G. Pozina, H. Blomqvist, T. Selinder, M. Collin, I. Reineck, L. Hultman, and H. Högberg, *Surface & Coatings Technology* **203**, 1682-1688 (2009).

- 52 T. C. Chou and T. G. Nieh, *Journal of the American Ceramic Society* **74**, 2270-2279 (1991).
- 53 K. Bobzin, N. Bagcivan, P. Immich, and M. Ewering, *Advanced Engineering Materials* **11**, 590-594 (2009).
- 54 V. Edlmayr, M. Moser, C. Walter, and C. Mitterer, *Surface & Coatings Technology* **204**, 1576-1581 (2010).
- 55 D. D. Ragan, T. Mates, and D. R. Clarke, *Journal of the American Ceramic Society* **86**, 541-545 (2003).
- 56 O. Mekasuwandumrong, P. Tantichuwet, C. Chaisuk, and P. Praserttham, *Materials Chemistry and Physics* **107**, 208-214 (2008).
- 57 M. Kathrein, W. Schintlmeister, W. Wallgram, and U. Schleinkofer, *Surface & Coatings Technology* **163**, 181-188 (2003).
- 58 J. M. Andersson, E. Wallin, V. Chirita, E. P. Munger, and U. Helmersson, *Physical Review B* **71**, 014101 (2005).
- 59 E. Wallin, J. M. Andersson, V. Chirita, and U. Helmersson, *Journal of Physics: Condensed Matter* **16**, 8971-8980 (2004).
- 60 B. Chapman, *Glow discharge process* (John Wiley & Sons, New York, 1980).
- 61 A. D. Glew, R. Sahaa, J. S. Kim, and M. A. Cappelli, *Surface & Coatings Technology* **114**, 224-229 (1999).
- 62 J. M. Lourenco, A. M. Maliska, A. N. Klein, and J. L. R. Muzart, *Materials Research* **7**, 269-275 (2004).
- 63 R. Kelly and P. Sigmund, *Surface & Coatings Technology* **50**, 7261 (1979).
- 64 A. Anders, *Thin Solid Films* **518**, 4087-4090 (2010).
- 65 B. A. Movchan and Demchish.AV, *Physics of Metals and Metallography-Ussr* **28**, 83-& (1969).
- 66 J. A. Thornton, *Annual Review of Materials Science* **7**, 239-260 (1977).
- 67 S. M. Rossnagel, J. J. Cuomo, and W. D. Westwod, *Handbook of plasma processing technology* (Noyers Publications, New Jersey, 1989).
- 68 P. J. Kelly and R. D. Arnell, *Vacuum* **56**, 159-172 (2000).
- 69 I. G. Brown, *Review of Scientific Instruments* **65**, 3061-3082 (1994).
- 70 I. G. Brown, *Annual Review of Materials Science* **28**, 243-269 (1998).

3 METHODS OF RESEARCH

This chapter presents the methods which were employed for the investigations of the relationship between synthesis, structure, mechanical properties, and stability. Besides a description of the experimental tools used for film synthesis and characterizations, also an introduction to DFT is provided.

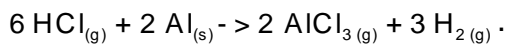
3.1 Film Synthesis by PECVD

3.1.1 Deposition system

The bipolar pulsed PECVD system as shown in Fig. 3-1 is equipped with a cylindrical vacuum chamber that has a volume of 28 liter with 300 mm in diameter and 400 mm in height. The chamber seal is installed with auxiliary heating elements and a fan cooling system to control the wall temperature. To monitor the temperature variation during the processes NiCrNi thermocouples are placed at the chamber wall as well as at the substrate holder with a height corresponding to the substrate location. Two stainless steel electrodes (160 mm in diameter), separated by tubular ceramic supports (170 mm), are mounted in the centre of the chamber. The bottom electrode is the cathode and the upper electrode is the anode. Hence the plasma is confined to the region between the two electrodes. The substrates are placed on the lower cathode, where the negative pulse is applied and thus experiences the maximum ion bombardment (See Fig. 3-2). The pulsed discharge source is generated by a combination of a DC generator (MDX, Advanced Energy) and a pulse switch unit

3. Methods of research

(SPIK1000A, MELEC). A novel generator developed by Ganciu et al. at Materia Nova R&D centre^{1,2} is also implemented to study High Power Pulsed PECVD that is abbreviated as HPPCVD in the flowing text. The alumina deposition processes are performed in an AlCl₃-Ar-H₂-O₂ atmosphere at a total pressure of 175 Pa. Apart from O₂, which is introduced into the chamber from the top, the other gases H₂, Ar, and AlCl₃ are mixed and introduced into the chamber through the gas shower located between the two electrodes. Using two separated gas inlets, reactions inside or in the vicinity of the gas shower can be avoided, thus inhibiting blocking of the gas inlet. The AlCl₃ precursor is produced in-situ through reaction between HCl and heated Al pellets (> 300 °C). At that temperature, HCl reacts completely with aluminum. The chemical reaction is:



Therefore, the AlCl₃ gas flow rate is regulated by 1/3 flow rate of HCl.

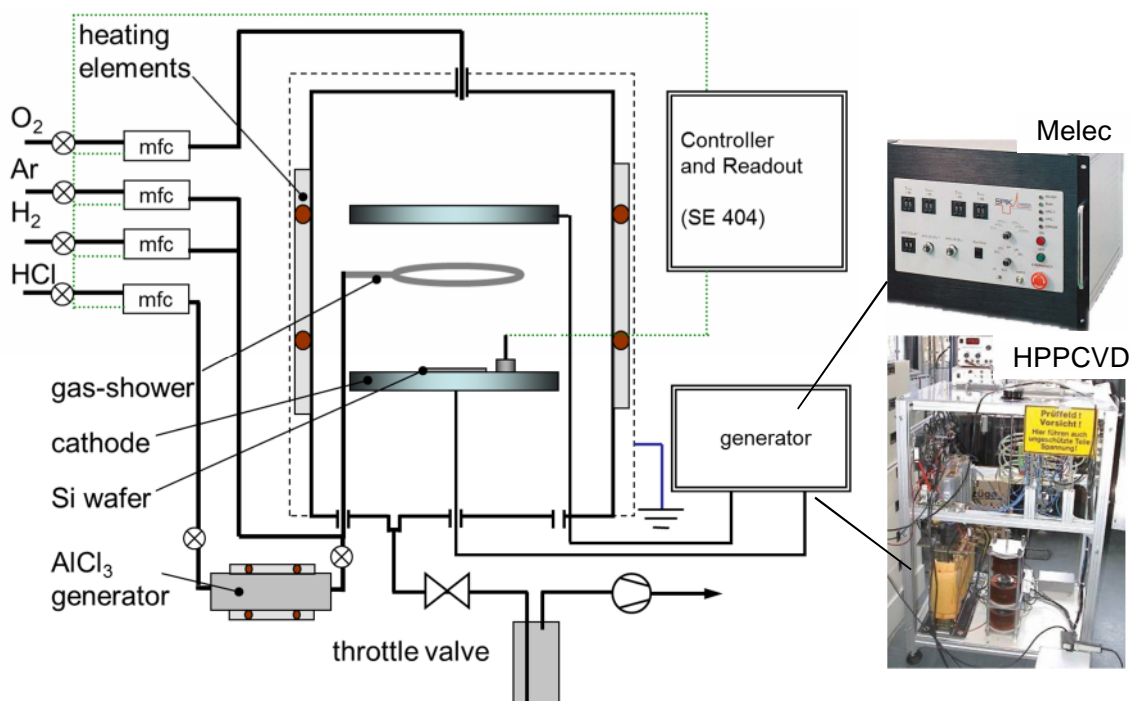


Fig. 3-1 Schematic of the PECVD system with the two different power supplies employed for plasma generation

3.1.2 Coating synthesis strategy

In this thesis, a systematic study of the process-properties-relationship has been carried out for (I) the precursors AlCl_3/O_2 ratio Γ_G , (II) duration of the negative pulse, namely $T_{\text{ON}}/T_{\text{OFF}}$ Ω , and (III) the plasma power density using HPPCVD. By modifying the O_2 gas flow while adjusting the Ar/H_2 ratio to keep the total flow rate constant (20 slh), Γ_G was varied from 0.5 to 1.28. To investigate the effect of the negative pulse length on the film properties, Γ_G of 1.2 was chosen yielding a relatively high deposition rate (see Ref. ³) as compared to other Γ_G values. The T_{ON} time is the period used to negatively bias the bottom electrode which holds the substrate, while the T_{OFF} time is the sum of the reverse time and the dead time (T_d). The reverse time corresponds to the time employed to negatively bias the upper electrode. At that moment, the bottom electrode is grounded and current keeps flowing. The dead time is the period while no voltage is applied at all, that is always kept at 10 μs (i.e. 5 + 5 μs). The sum of the T_{ON} and T_{OFF} periods is set to 90 μs , while Ω was varied from 1.6 to 10. For the case of HPPCVD, unipolar voltage pulses up to 1.4 kV with a nominal duration in the range of 80 to 100 μs and a frequency of 5 kHz were employed that yields a discharge at approx. four times larger power density than those utilized conventionally. A typical time dependent current and voltage waveform, measured using an ELDITEST GE 8115 voltage and Tektronik A6303 current probe, respectively, and recorded with a Tektronik TDS 3014B digital oscilloscope, is presented in Fig. 3-2

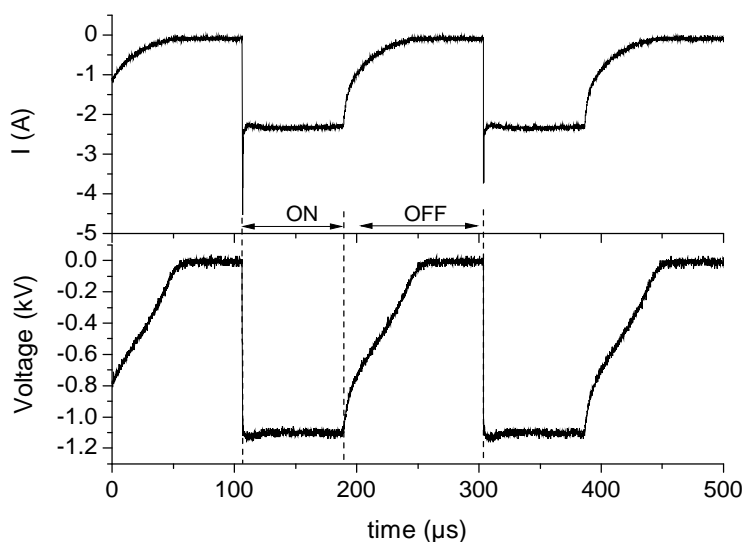


Fig. 3-2 Time dependent cathode voltage $V(t)$ and time dependent discharge current $I(t)$ of a discharge operating at a pulse width of $80 \mu\text{s}$ and a frequency of 5 kHz.

Tab. 3-1 Parameters used for alumina coating deposition

Standard parameters							
Frequency	Voltage	Pressure	gas flow (l/h)				$T_{\text{deposition}}$
(kHz)	(V)	(Pa)	Ar	H_2	O_2	HCl	($^{\circ}\text{C}$)
11	900	175	3.10	16.40	0.28	0.69	560
Variation I precursor ratio		Variation II pulse length		Variation III high pulse power			
O_2 (l/h)	AlCl_3/O_2 (Γ_G)	T_{ON}	$T_{\text{ON}}/T_{\text{OFF}}$	Voltage (kV)	Power (W/cm^2)		
0.2-1.2	0.4-2.5	50-73	1.6-10	0.7-1.4	up to 19		

3.1.3 Coating synthesis procedures

Single crystal silicon wafers with a (001) orientation as well as hot work tool steel X38CrMoV5 (1.2343) and the molybdenum alloy TZM were chosen as substrate materials in the present work. The steel substrates were ultrasonically cleaned prior

3. Methods of research

to the chamber loading. After reaching a base pressure of 8 Pa achieved by a rotary vane pump (Edwards 2012A), the substrates were heated up to the deposition temperature by means of resistance and Ar-H₂ plasma heatings. Prior to the Al₂O₃ deposition, plasma etching, namely Ar⁺ bombardment, was performed to clean the surface and fine tune the substrate temperature. After 3 minutes of this procedure, the reaction gas was introduced into the chamber and the deposition started. A nitriding process was performed additionally for the metallic substrates in order to provide a load support zone, and hence better adhesion. The standard deposition time was 4 hours. After deposition, a gradual cooling process was performed in order to avoid film delamination caused by thermal shock. The whole process is illustrated in Table 3-2.

Tab. 3-2 Process procedure of PECVD Al₂O₃

Procedures	Time period	Remarks
Pumping	About 1 h	A base pressure of 8 Pa
Heating	About 2 h	Substrate about 500 °C
Etching	About 3 min	Flow ratio Ar : H ₂ =15:5, 175Pa
Nitriding (metallic substrates)	About 12 h	N ₂ H ₂ Ar
Depositing	About 4 h	The other parameters vary Cooling in a Ar circumstance
Cooling	About 3 h	at pressure of 500 Pa and interval pumping

3.2 Analytical Methods

3.2.1 Plasma characterization: Optical Emission Spectroscopy OES

Emission is a process by which two quantum mechanical states of a particle (atom, ion or molecular), become coupled to one another through a photon, resulting in the production of light.⁴ This process transition is also demonstrated in Fig. 3-3a. An electron transits from a higher state q into the low state k by emitting a photon with a characteristic wavelength. The photon energy hu is equal to the energy gap between these two quantum mechanical states. Here the optical emission spectroscopy refers to the detected photons with wavelengths roughly in the optical region, namely from ~200 to ~900 nm. As each element's emission spectrum is unique, the spectroscopy can be utilized to identify the elements in the matter of unknown composition. Similarly, the emission spectra of molecules can be used in chemical analysis of substances.

The measured intensity of an emission line can be expressed according to the equation:⁴

$$I = A_{pk} \times n_p, \quad (\text{eq. 3-1})$$

where A_{pk} is the transition probability from level p to level k , n_p is the population density of the excited level p . This equation shows that the line intensity depends only on the density of the excited level n_p , which is determined by the plasma conditions.

Regarding the production of the excited species, the electron excitation is assumed as one of the most important processes,



The transition probability A_{pk} is contributed by the electron density n_e and the electron excitation coefficient X_{ext} , which is a function of the electron impact excitation cross section $\sigma(E)$, the threshold energy of E_{thr} and the electron energy distribution function $f(E)$:⁴

$$A_{pk} \propto n_e \cdot X_{ext} , \quad (\text{eq. 3-3})$$

$$X_{ext} = \int_{E_{thr}}^{\infty} \sigma(E)(2/me)^{1/2} \sqrt{E} \cdot f(E)dE . \quad (\text{eq. 3-4})$$

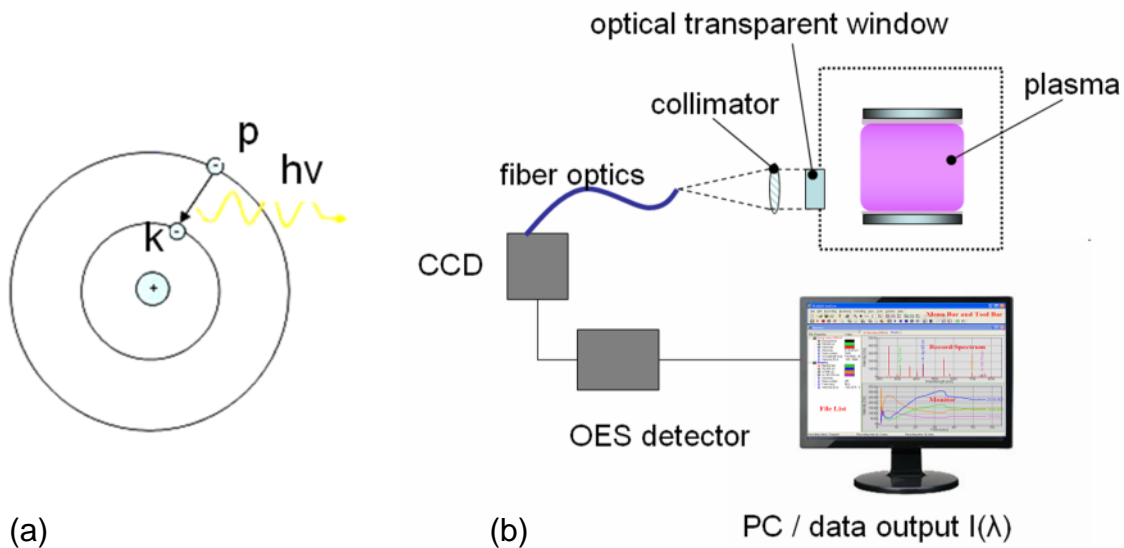


Fig. 3-3 Schematic diagrams of (a) atomic spontaneous emission and (b) the OES system

The OES experiments were carried out in this work to detect excited plasma species and therefore to gain insight of the plasma composition. They were carried out by probing a window at ~ 1 cm above the bottom electrode (see Fig. 3-1). Several line intensities corresponding to H (656 nm), Ar (750 nm), Ar^+ (476 nm), Al (396 nm), and AlCl (261 nm) were recorded. Cl emission lines could not be followed because they overlap with those emitted by the Ar atoms. The spectrometer is equipped with a 600 lines/mm grating and 2048-element silicon array detector. The analyzed spectral

region ranges from 200 to 900 nm. The resolution of the device is 0.4 nm. The optical collimator with a CCD camera is fixed on a quartz window which is located at 1 cm from the surface of the bottom cathode. The OES system (PLASUS EmiCon) setup is shown in Fig. 3-3b.

3.2.2 X-Ray Diffraction (XRD)

XRD is a powerful characterization tool utilized for structure analysis, such as identification of phase constitutions, lattice parameter, and crystallite size etc. The incident x-ray beam with a wavelength exhibit ranged from 0.1 to 10 nm⁵. Diffraction occurs when the incident X-ray beam interacts with the crystalline lattice planes. The principle of the diffraction phenomenon is described by Bragg's law⁵, that is also illustrated in Fig. 3-4c.

$$n\lambda = 2d \times \sin\theta \quad (\text{eq. 3-5})$$

where n is the diffraction order, λ is the wavelength of the characteristic X-ray beam, d is the lattice plane distance and θ is the diffraction angle.

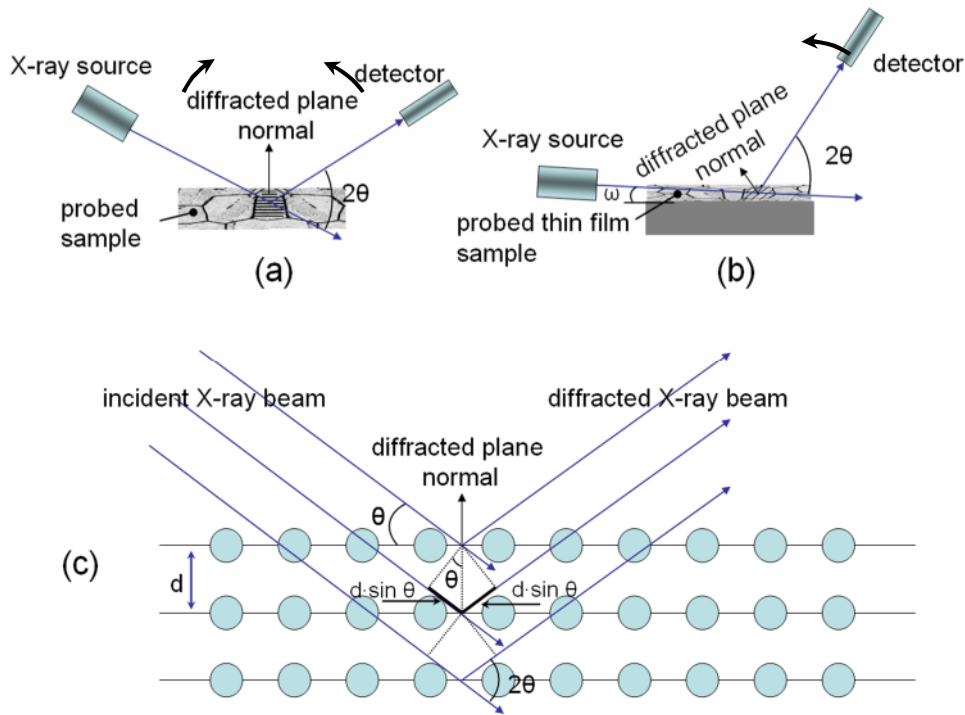


Fig. 3-4 Scheme of (a) XRD measurement under Bragg-Brentano configuration, (b) XRD measurement under grazing incidence configuration, (c) diffraction condition under Bragg's law.

d can be determined based on the known λ and the measured θ . There are several scanning modes or geometries for XRD measurements, providing different information with respect to the structure. The Bragg-Brentano (BB) geometry, also called $\theta - 2\theta$, is normally employed for polycrystalline samples, as illustrated in Fig. 3-4a. In this geometry, only diffraction from lattice planes parallel to the sample surface can be detected. Although this geometry offers the highest accuracy and finest resolution, it has a limitation especially for thin film samples. Due to the limited thickness of thin films and the theta-dependent X-ray penetration depth a significant fraction of the diffracted intensity may be from the substrate. Using the grazing incidence (GI) geometry (Fig. 3-4b), the low incident angle of the X-ray allows for diffraction in the vicinity of the sample surface, thus yielding a significant fraction of

the diffracted intensity from thin film. However, diffraction planes are not parallel to sample surface, but in different orientation (see Fig. 3-4b).

In this study, both two geometries were employed for the XRD measurements using a Siemens D5000 diffractometer. The X-ray source was a Cu anode with a Ni filter which was operated at 40 kV, 40 mA. 2θ ranged from 20° to 80° at a scanning speed of 1 s/step and a step size of 0.02° . The incident angle for the GI-XRD measurements was 1° . The BB-XRD measurements were employed to identify the structure and the phase composition of the powders for thermal stability investigations. Furthermore, the phase analysis at the interface was also carried out by conventional TEM diffraction measurements. The experimental Debye-Scherrer ring patterns were simulated using the Electron Microscopy Software – Java Version (jems) by P. Stadelmann⁶. For calibration, the diffraction pattern of a poly-crystalline gold sample was used.

3.2.3 Simultaneous Thermal Analysis (STA)

Simultaneous Thermal Analysis (STA) combines thermogravimetry (TGA) and differential scanning calorimetry (DSC). Mass changes and caloric effects are simultaneously measured with respect to the temperature or time. As illustrated in Fig. 3-5a, a typical TGA apparatus consists of a sensitive temperature and mass measurement technology. Besides, the system allows for the measurement under vacuum conditions or with protective purge gas. The principle of the STA measurement is illustrated in Fig. 3-5b. There are two crucibles inserted into the furnace (Fig. 3-5a) with precise heating and cooling rates. One crucible is empty serving as a reference crucible, while the other one contains the measured sample. By measuring the temperature difference between these crucibles, the heat flow can

be calculated. This DSC measurement is commonly employed to study thermal transitions such as physical or chemical reactions. Simultaneously, the mass change of these two crucibles is also measured for TGA analysis, by which a possible mass gain or loss during physical or chemical reactions can be monitored.

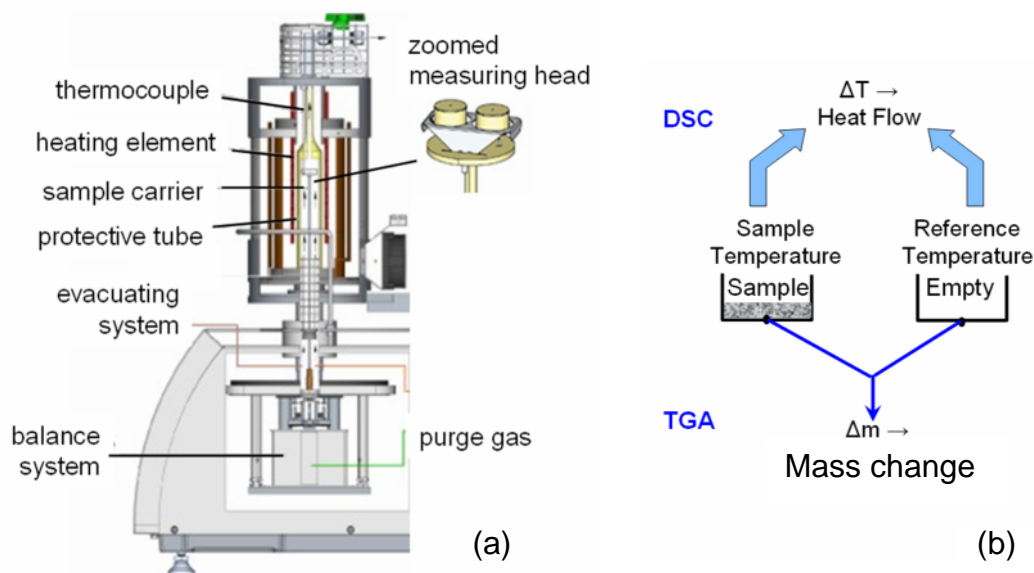


Fig. 3-5 Schematic of the (a) STA apparatus⁷ and the (b) principle of STA measurement.

In the present work, the STA measurements were carried out using a Netzsch-STA Jupiter 449C simultaneous thermal analyzer in a 99.9997 % pure Ar atmosphere with a constant flow rate of $\sim 50 \text{ ml}\cdot\text{min}^{-1}$. The powder samples for the STA measurements were prepared by depositing the films on the iron foils and were subsequently dissolved in a dilute HNO_3 solution. After filtering the solution, the coating particles were collected, dried and grinded to powders with a particle size ranging from 5 to 10 μm . Powder mass of $\sim 10 \text{ mg}$ was used to fill an alumina crucible which was preheated up to $1500 \text{ }^\circ\text{C}$ to avoid surface contamination. The heating and cooling rates were kept constant at $20 \text{ K}\cdot\text{min}^{-1}$. The temperature cycle of heating up to

1600 °C and subsequent cooling to 150 °C was performed twice and the second heating run was used as a baseline to the first one.

3.2.4 Morphology and chemical composition

The film surface topography and morphology were evaluated by analyzing the surface and cross section of the sample using a scanning electron microscope (SEM) (JEOL JSM-6480). The composition of the film was analyzed by energy dispersive X-ray analysis (EDX) using an EDAX Genesis2000 detector implemented in the SEM apparatus. For the chemical analysis, a constant accelerating voltage of 6 kV was applied. Transmission electron microscopy (TEM) was employed to obtain spatially resolved information such as the microstructure and the composition at the film/substrate interface and along the growth direction. Thin cross-sections of the coatings were prepared using the focused ion beam (FIB) technique in a FEI Strata FIB 205 workstation. TEM measurements were performed in a FEI Tecnai F20 transmission electron microscope operated at an acceleration voltage of 200 kV. In order to determine the nanoscale chemical composition at the interface as well as along the growth direction of films, EDX line scans were performed in scanning mode (STEM) with a step width of 2 nm and 8 s acquisition time per data point. Z-contrast images were taken by the high angle annular dark field (HAADF) detector at a camera length of 50 mm. The acquired STEM and STEM EDX data were evaluated using the TEM Imaging & Analysis software package by FEI.

3.2.5 Elastic properties: Nanoindentation

Nanoindentation has been utilized for the characterization of the mechanical properties of materials. From the load-displacement curve of the indentation stiffness, reduced modulus and hardness can be extracted⁹. The stiffness is the slope of the initial unloading curve which is directly linked to the reduced modulus of the sample and contact area. This relationship is expressed in eq. 3-6:

$$E_r = \frac{1}{2} \sqrt{\frac{\pi}{A}} \times \left(\frac{dP}{dh} \right)_{\text{initial unloading}} = \frac{\sqrt{\pi}}{2} \frac{S}{\sqrt{A}}, \quad (\text{eq. 3-6})$$

where E_r is the reduced modulus, A the contact area, P the load, h the displacement, and S the stiffness.

After knowing E_r , the elastic modulus can be calculated if Poisson's ratio is known using eq.3-7.

$$\frac{1}{E_r} = \frac{(1-\nu^2)}{E} + \frac{(1-\nu_i^2)}{E_i}, \quad (\text{eq. 3-7})$$

where ν and E are Poisson's ratio and elastic modulus of the measured sample, respectively, and ν_i and E_i are the Poisson's ratio and elastic modulus of the indenter. The nanoindentation measurements in the current work were carried out using a Berkovich tip in a Hysitron nanoindentation system. Fuse silica is used as a standard sample for calibrating the tip area function. The maximum load was 2500 μN to keep the contact depth ≤ 80 nm. The film thickness was $\geq \sim 1.0$ μm . The recorded data were analyzed using the method of Oliver and Pharr⁹.

3.3 Density Functional Theory (DFT)

Using a quantum mechanical description of a material system, DFT provides the ground state electronic structure of materials based on their electron density. On one hand, the results of DFT simulations for solid-state systems agree satisfactorily with experimental data as the approximations used in the theory were improved to better model the exchange and correlation interactions in the 1990s. The elastic properties of the materials can be determined within $\sim 15\%$ ¹⁰⁻¹², while cohesive energy as well as equilibrium volume (mass density) can be reproduced within $\sim 5\%$ ¹³. Based on DFT, understanding chemical bonding in terms of charge density is available. On the other hand, with the enormous development of computers, this computational method offers a powerful tool for the quantum mechanical design of new materials, which shows low expenditure compared to experimental cost and time.

The fundamental basis of DFT was provided by Hohenberg and Kohn who presented two theorems.

1. The total energy of a system is a unique functional of the ground-state electron density. A ground electronic state is described by a wave function $\psi(\mathbf{r}_1, \mathbf{r}_2 \dots \mathbf{r}_N)$ satisfying the many-electron time-independent Schrödinger equation

$$H\psi = E\psi \quad (\text{eq. 3-8})$$

Hamiltonian H consists of kinetic energy of the system T , the potential energy from the external field due to positively charged nuclei V , and electron-electron interaction energy W . After obtaining the electron density $n(\mathbf{r})$ from the solution of eq. 3-8, the total energy functional is expressed as:

$$E[n(\mathbf{r})] = T[n(\mathbf{r})] + V[n(\mathbf{r})] + W[n(\mathbf{r})] \quad (\text{eq. 3-9})$$

2. The exact ground state density minimizes functional $E[n(\mathbf{r})]$:

$$E[n(\mathbf{r})] = T_1[n(\mathbf{r})] + \int V(\mathbf{r}) \cdot n(\mathbf{r}) d^3r + E_{\text{Hartree}}[n(\mathbf{r})] + E_{\text{xc}}[n(\mathbf{r})] \quad (\text{eq. 3-10})$$

T_1 represents single the particle kinetic energy, the second term designates the interaction between electrons and nuclei and $E_{\text{Hartree}}[n(\mathbf{r})]$ is the Hartree electrostatic electron-electron interaction. The term $E_{\text{xc}}[n(\mathbf{r})]$ is the exchange-correlation energy describing all many-body interactions. Since $E_{\text{xc}}[n(\mathbf{r})]$ cannot be calculated exactly in general, different approximations are applied to obtain the exchange-correlation energy. Two of the most popular approximations of this exchange-correlation functional are the local density approximation (LDA)¹⁴ and generalized gradient approximation (GGA)¹⁵.

The computational DFT study in this thesis was performed using the Vienna *ab initio* simulation package (VASP)¹⁶. Projector augmented wave potentials¹⁷ and general gradient approximation by Perdew and Wang¹⁸ were employed in these calculations. Energy cut-off of 500 eV was used. Brillouin-zone integrations were performed using Monkhorst-Pack k-point meshes of 7x7x7. Electronic and ionic relaxations were converged at energies of 0.01 and 0.1 meV, respectively. The total energy was used as a measure of phase stability, since the same chemical compositions were always compared between the α - and the γ -Al₂O₃ phase. The bulk modulus was then obtained by fitting the energy-volume curve with Birch-Murnaghan¹⁹ equation of state. The lattice constants were obtained by fitting the energy-lattice constants curve with the third ordered polynomial equation. The electronic structure was studied by evaluating electron density distributions.

Two types of γ -Al₂O₃ cells (40 atoms) with both cubic spinel and tetragonal hausmannite structures were employed in this thesis. The spinel γ -Al₂O₃ configuration was constructed applying the approach suggested by Gutiérrez *et al.*¹⁰

where the supercell is built by stacking three primitive cells based on the spinel structure, space group $Fd\bar{3}m$ (see Fig. 3-7a). In this structure, the energy is minimized with the cation vacancies are located on octahedral sites, at positions that are most far away from each other, namely $(1/2, 1/2, 1/6)$ and $(1/2, 1/2, 2/3)$. For the tetragonal $\gamma\text{-Al}_2\text{O}_3$ configuration, the primitive cell of hausmannite Mn_3O_4 structure, space group $I4_1/amd$, was applied and the c direction was extended to $3c$, accounting for 42 atoms. Two vacancies were then introduced in order to obtain stoichiometric Al_2O_3 , either the octahedral site 8d or the tetrahedral site 4a of Al as a possible vacancy site. The vacancy distance was also probed as follows: two octahedral Al vacancies at the shortest and the largest distance (O+O close and O+O apart, respectively) as well as one tetrahedral and one octahedral vacancy at the shortest and the largest distance (T+O close and T+O apart, respectively) as illustrated in Fig. 3-7b-e. Fig. 3-7b illustrates the tetragonal hausmannite $\gamma\text{-Al}_2\text{O}_3$ supercell (O+O apart) with two vacancies at $(0.3750, 0.1250, 0.0833)$ and $(0.8750, 0.6250, 0.5833)$. To compare the relative stability the corresponding calculations on $\alpha\text{-Al}_2\text{O}_3$ were also carried out. The unit cell of hexagonal $\alpha\text{-Al}_2\text{O}_3$ with space group $R\bar{3}c$ contains 30 atoms and hence the cell along the c direction was extended by $1/3c$ to obtain the 40 atoms configuration, comparable to the $\gamma\text{-Al}_2\text{O}_3$ description. This supercell configuration breaks the crystalline symmetry. Therefore, an $\alpha\text{-Al}_2\text{O}_3$ unit cell containing 30 atoms was further calculated to correct the total energy due to this symmetry breaking. The total energy of the $\alpha\text{-Al}_2\text{O}_3$ supercell with M additives (E_α) was obtained from:

$$E_\alpha = \frac{E(40, M) + \Delta E}{40}, \quad (\text{eq. 3-11})$$

where

$$\Delta E = \frac{4}{3} E(30) - E(40) \quad . \quad (\text{eq.3-12})$$

$E(40)$, $E(40,M)$, and $E(30)$ designate the total energy without and with additives (40 atoms) as well as the total energy of original $\alpha\text{-Al}_2\text{O}_3$ (30 atoms), respectively. The additives were placed at substitutional positions of the octahedral Al site. Considering the supercell of 40 atoms, an additive atom M in the supercell yields a composition of $\text{Al}_{15}\text{O}_{24}\text{M}$ (2.5 at.% of M).

For the calculation of Cl incorporation in γ - and $\alpha\text{-Al}_2\text{O}_3$, one Cl atom was firstly inserted in these cells at interstitial sites (octahedral for α -alumina; tetrahedral and octahedral for $\gamma\text{-Al}_2\text{O}_3$) or by substituting an O atom. This corresponds to a Cl content of 2.44 and 2.50 at.%, respectively, which is close to the Cl content measured in our coatings. Table 3-3 summarizes the Cl position in these two alumina polymorphs. In a second step, the pore formation mechanism in $\gamma\text{-Al}_2\text{O}_3$ was addressed. The reference configuration was the original $\gamma\text{-Al}_2\text{O}_3$ cell with two vacancies: one at octahedral $(\frac{1}{2}, \frac{1}{2}, \frac{2}{3})$ and one at tetrahedral $(0, \frac{1}{2}, \frac{1}{6})$ site. This configuration was compared to a cell where the tetrahedral $(0, \frac{1}{2}, \frac{1}{6})$ vacancy is exchanged with an Al atom at $(0.88312, 0.87855, 0.61993)$, so as to minimize the distance between the vacancies. Then, the same configurations were used with the vacancies replaced by Cl atoms to evaluate if this impurity agglomeration is energetically favorable.

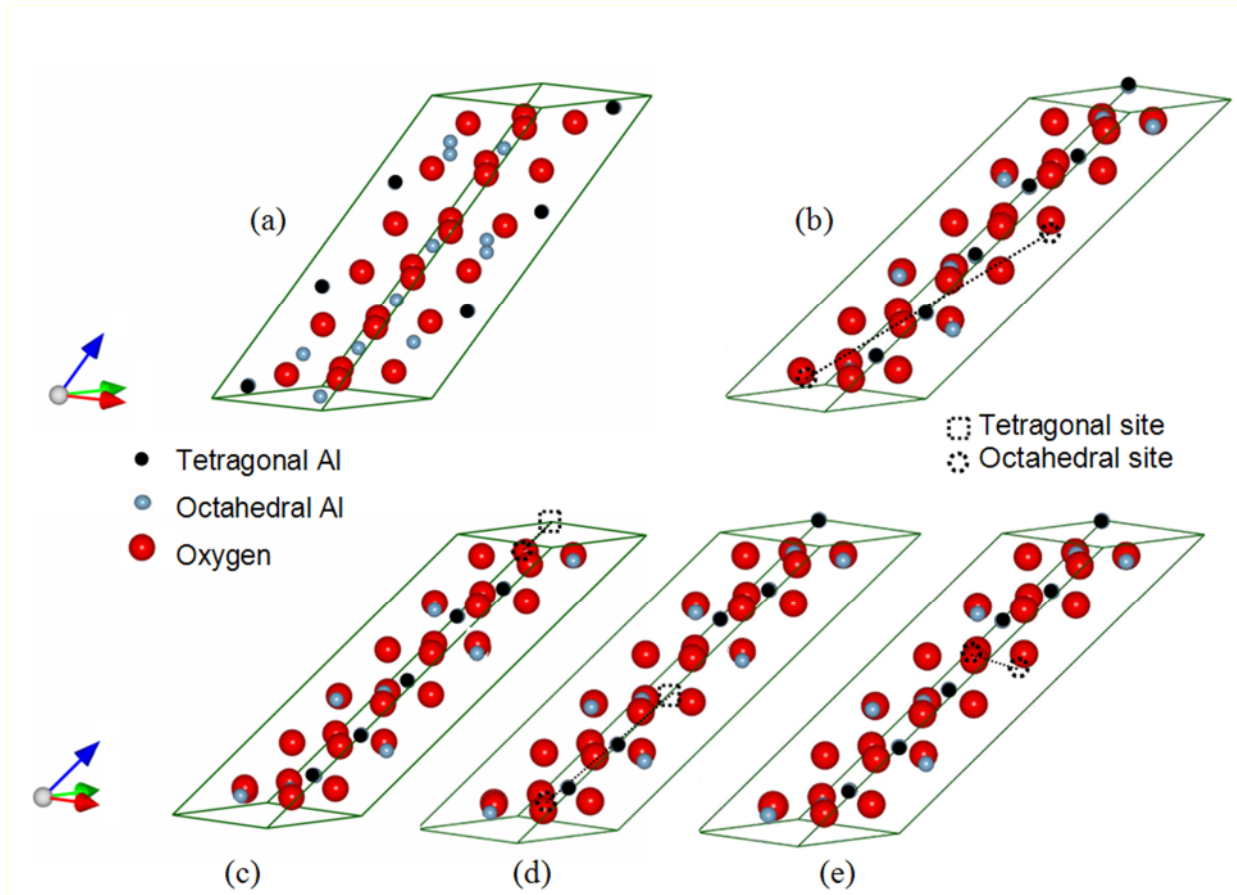


Fig. 3-6 $\gamma\text{-Al}_2\text{O}_3$ structure calculated based on (a) spinel description suggested by Gutiérrez *et al.*,¹⁰ and on tetragonal hausmannite description with (b) O+O separated, (c) T+O close, (d) T+O separated and (e) O+O close. Large and small spheres represent oxygen and aluminum atoms, respectively. O and T stand for octahedral and tetrahedral vacancies, respectively.

Tab. 3-3 Cl positions in the alumina cells

Polymorph	Stoichiometry	Cl position
α -Al ₂ O ₃	Al ₁₆ O ₂₄ Cl	Octahedral void: $(\frac{1}{3}, \frac{2}{3}, 0.47583)$
	Al ₁₆ O ₂₃ Cl	Oxygen site: (0.34643, 0.99715, 0.18190)
γ -Al ₂ O ₃	Al ₁₆ O ₂₄ Cl	Tetrahedral void: $(0, \frac{1}{2}, \frac{1}{6})$
	Al ₁₆ O ₂₄ Cl	Octahedral void: $(\frac{1}{2}, \frac{1}{2}, \frac{2}{3})$
	Al ₁₆ O ₂₃ Cl	Oxygen site: (0.34643, 0.99715, 0.18190)

- ¹ M. Ganciu, M. Hecq, S. Konstantinidis, J. P. Dauchot, M. Touzeau, L. de Poucques, J. Bretagne, in *World Patent No. WO 2005/090632; Vol. No. WO 2005/090632* (2004).
- ² M. Ganciu, S. Konstantinidis, Y. Paint, J. P. Dauchot, M. Hecq, L. de Poucques, P. Vasina, M. Mesko, J. C. Imbert, J. Bretagne, M. Touzeau, J. Optoelectron. Adv. Mater. **7**, 2481-2484 (2005).
- ³ D. Kurapov, J. M. Schneider, Plasma Chem. Plasma Process. **25**, 613-623 (2005).
- ⁴ U. Fantz, Plasma Sources Science & Technology **15**, 137-147 (2006).
- ⁵ B. D. Cullity, *Elements of X-ray Diffraction*, 2nd ed. (Addison-Wesley Publishing Company, Inc., London, 1978).
- ⁶ <http://cimewww.epfl.ch/people/stadelmann/jemswebsite/jems.html>.
- ⁷ <http://www.netzsch-thermal-analysis.com>.
- ⁸ N. C. Parasnis, K. Ramani, J. Therm. Anal. Calorim. **55**, 709-719 (1999).
- ⁹ W. C. Oliver, G. M. Pharr, J. Mater. Res. **7**, 1564-1583 (1992).
- ¹⁰ G. Gutiérrez, A. Taga, B. Johansson, Phys. Rev. B **65**, 012101 (2002).

- ¹¹ J. M. Schneider, R. Mertens, D. Music, J. Appl. Phys. **99**, - (2006).
- ¹² J. M. Soler, E. Artacho, J. D. Gale, A. Garcia, J. Junquera, P. Ordejon, D. Sanchez-Portal, Journal of Physics-Condensed Matter **14**, 2745-2779 (2002).
- ¹³ O. Eriksson, K. H. J. Buschow, W. C. Robert, C. F. Merton, I. Bernard, J. K. Edward, M. Subhash, V. Patrick, in *Encyclopedia of Materials: Science and Technology* (Elsevier, Oxford, 2003), p. 1-11.
- ¹⁴ W. Kohn, L. J. Sham, Physical Review **140**, A1133 (1965).
- ¹⁵ P. Hohenberg, W. Kohn, Phys. Rev. B **136**, B864-& (1964).
- ¹⁶ G. Kresse, J. Hafner, Phys. Rev. B **48**, 13115-13118 (1993).
- ¹⁷ P. E. Blöchl, Phys. Rev. B **50**, 17953 (1994).
- ¹⁸ J. P. Perdew, Y. Wang, Phys. Rev. B **46**, 12947 (1992).
- ¹⁹ F. Birch, Phys. Rev. **71**, 809-824 (1947).

4 PROCESS-PROPERTIES RELATION IN PECVD ALUMINA THIN FILM

This chapter addresses the relationship between synthesis conditions, structure, and properties of PECVD grown Al_2O_3 thin films. The effect of the precursor ratio, pulse length, and power density on the phase formation and elastic properties was investigated.

4.1 Introduction

As already mentioned in chapter 2, it is still a challenge to produce phase pure α - Al_2O_3 films at low growth temperature ($<600\text{ }^\circ\text{C}$) with dense structure. Although the substantial decrease of the temperature limit for the α - Al_2O_3 formation has been achieved recently, the deposited films have been found to exhibit porosity^{1,2} and hence inferior elastic properties² compared to bulk and CVD α - Al_2O_3 ⁶, especially for the case of PECVD α - Al_2O_3 films. Therefore our goals for this study are firstly to contribute to a better understanding of the role of plasma chemistry in the correlation between chemical composition, constitution, and morphology of Al_2O_3 , more precisely, to investigate the porosity formation mechanism in the PECVD films. To achieve this goal the influence of the pulse ON/OFF time ratio on the composition, morphology, phase constitution, and elastic properties of pulsed PECVD alumina films was investigated. On the other hand, a novel pulsed plasma generator which is able to deliver voltages up to 1.4 kV allowing for approx. 4 times larger power densities than those achieved in the conventional PECVD processes was utilized.

Using plasma characterization tools and plasma modeling, it is shown that increasing the discharge power density values from 5 W/cm² to 19 W/cm² results in an increase of the energy and the flux of the bombarding species towards the growing film, as well as in a more efficient AlCl₃ dissociation. These conditions allow for the growth of dense and phase pure α -Al₂O₃ films with negligible Cl incorporation and elastic properties close to the bulk values at a temperature of 560 ± 10 °C.

4.2 Influence of precursor ratio on the composition-constitution-morphology relationship of PECVD Al₂O₃ thin films

4.2.1 On the plasma composition

The plasma composition has been studied by OES. In addition to the strong lines related to argon and hydrogen species, lines from aluminum-related species such as Al I (309.2 and 396.1 nm), AlO (467.2 nm) and AlCl (261.4 nm) have been observed. Fig. 4-1 shows the evolution of these lines as a function of the AlCl₃ to O₂ ratio (Γ_G). As expected, when increasing Γ_G from 0.40 to 2.50, an increase of the AlCl signal at 261.4 nm and the Al I signal at 396.1 nm and a decrease of the AlO signal at 467.2 nm was observed. Indeed, by increasing the oxygen flow (by decreasing Γ_G), the formation of AlO species is promoted. Therefore, the population of AlO decreases with increasing Γ_G , while those of Al and AlCl increase. Surprisingly, the Al I line at 396.1 nm does not behave similarly to the one at 309.2 nm. The latter exhibits a minimum for $\Gamma_G = 1.28$. This peculiar behavior may be attributed to overlap with a hydroxyl (OH) line at 308.7 nm. The resolution of our spectrometer is ~ 0.5 nm. The measured signal at ~ 309 nm may therefore be associated with both Al I and OH species. At low Γ_G , the high ~ 309 nm signal intensity may be attributed to the high

partial pressure of OH (high O₂ flow), while at high Γ_G , the high ~ 309 nm signal intensity is likely to be due to the high partial pressure of Al (low O₂ flow).

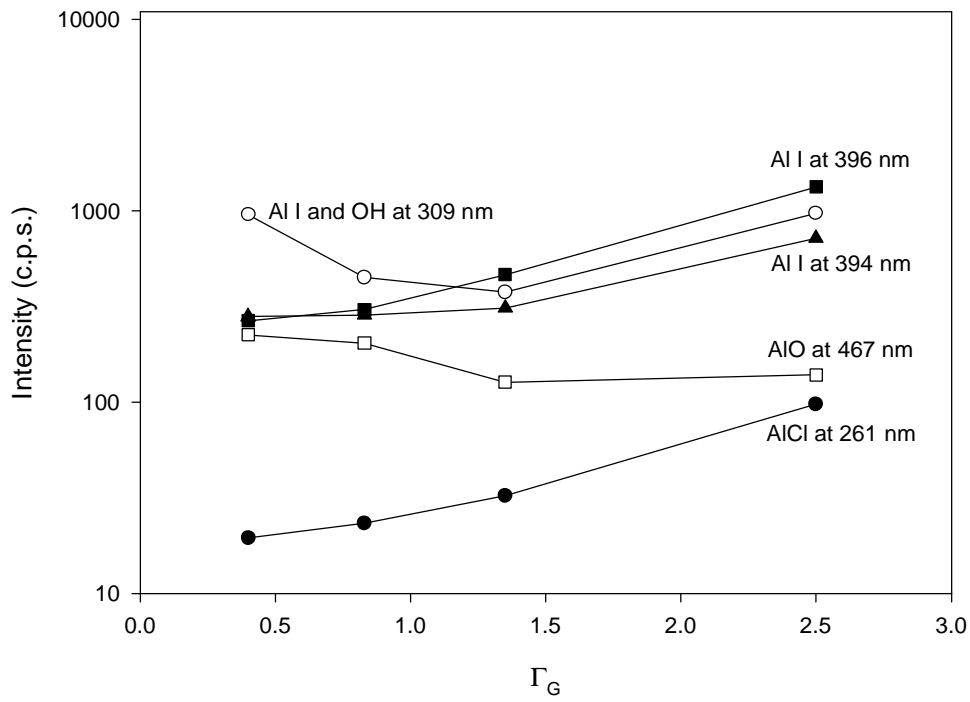


Fig. 4-1 Emission line intensity at ~ 261 nm (AlCl), ~ 309 nm (Al I, OH), ~ 396 nm (Al I) and ~ 467 nm (AIO) versus the chemical precursor ratio (Γ_G).

4.2.2 On the film composition and phase constitutions

Using EDX, the chemical composition of the deposited films was measured. The chlorine concentration (Cl at.%) as well as the stoichiometric ratio ($\frac{\text{O at.}\%}{\text{Al at.}\%}$) are given as a function of Γ_G in Fig. 4-2. The solid horizontal line presents the stoichiometric ratio of 1.5 for Al₂O₃. These results indicate that, within the experimental error margin of EDX, all the deposited films are close to stoichiometric and that the Cl content increases non-linearly as Γ_G is increased. The incorporation of Cl in the films is believed to be related to the incomplete dissociation of AlCl₃ in the plasma. From the OES data, it exhibits an increase of the AlCl population as Γ_G is

increased. Other mechanisms that may affect the amount of incorporated Cl include surface diffusion and ion implantation. Ion bombardment enables dissociation of AlCl based particles adsorbed on the growing film surface before they are incorporated into the film, leading to Cl desorption. It has been shown previously that this mechanism is strongly influenced by Γ_G , with an increase of the so-called normalized ion flux with a decrease of Γ_G ⁷. Another mechanism could be Cl ion implantation, but this is unlikely since the mean ion energy in our process has been estimated to be approximately 100 eV.⁸

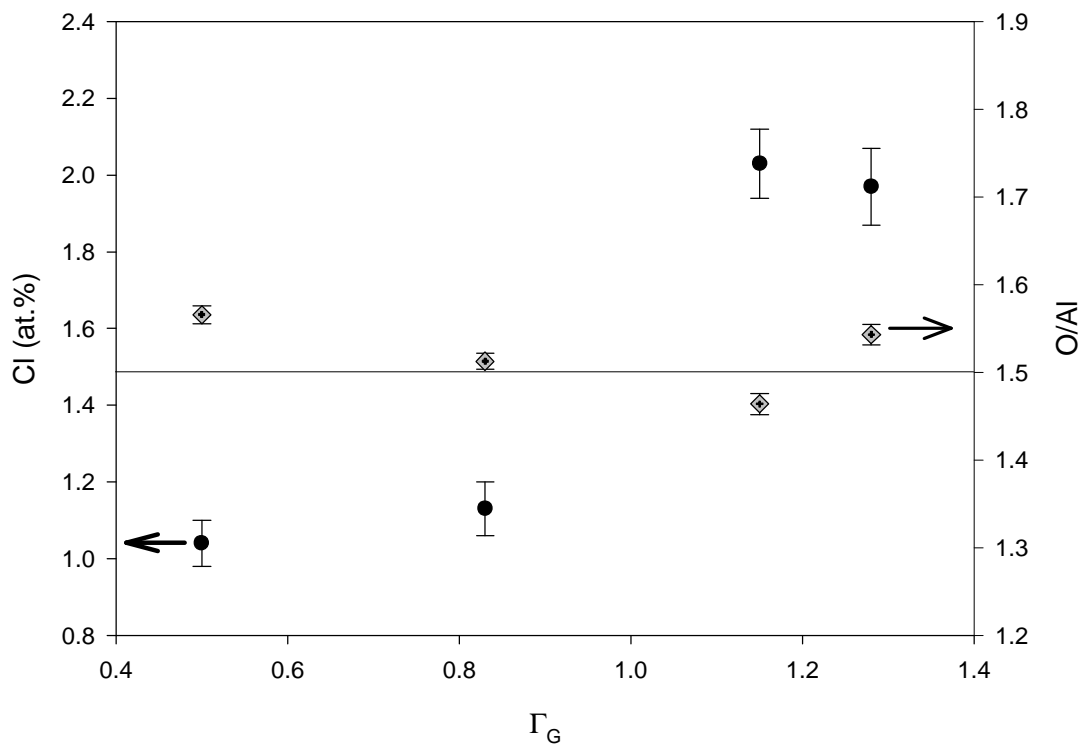


Fig. 4-2 Cl content in the films and O/Al ratio versus the AlCl₃/O₂ chemical precursor ratio (Γ_G). The solid horizontal line represents the O/Al ratio of Al₂O₃.

Fig. 4-3 shows the structure evolution of the deposited films as a function of Γ_G . All the films are crystalline and, depending on Γ_G , correspond to γ - (JCPDS card N° 29-63), α -Al₂O₃ (JCPDS card N°10-173), or a mixture of both. For $\Gamma_G \geq 1.15$, pure γ -Al₂O₃ films are deposited, depicted by the strong diffraction line at about $2\theta = 45.6^\circ$

(400) and $2\theta = 37.6^\circ$ (311). For $0.5 < \Gamma_G < 1.15$, the films consist of pure α - Al_2O_3 with strong diffraction lines at $2\theta = 52.6^\circ$, 43.4° , and 25.6° . Finally, for $\Gamma_G \leq 0.5$, a mixture of γ - or α - Al_2O_3 is observed. Formation of γ - Al_2O_3 at high value of Γ_G and α - Al_2O_3 at low value has already been observed and associated with large normalized ion flux values at low Γ_G ^{2,8}. The additional energy supplied by the ion bombardment enhances the surface mobility of the condensed species and may favour the formation of α - Al_2O_3 . The film constitution appears to be related to the plasma chemistry. It has been suggested that a large OH content favors the formation of γ - Al_2O_3 because hydroxyl groups can be incorporated, which is not the case for α - Al_2O_3 ⁹. Synthesis of pure γ - Al_2O_3 has even been reported for Γ_G as low as 0.3⁹.

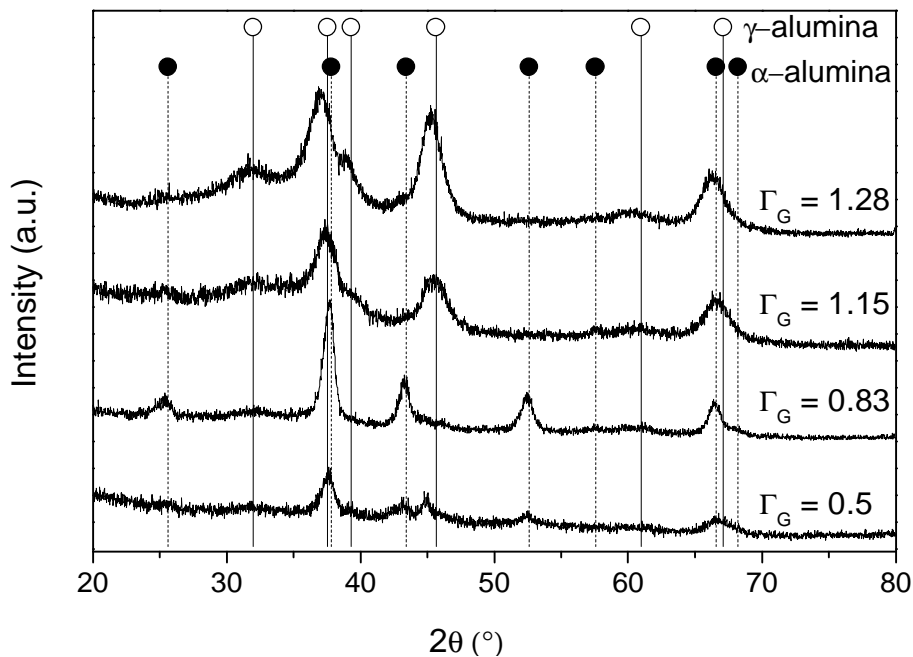


Fig. 4-3 X-ray diffraction data for films grown at different chemical precursor ratios (Γ_G).

Using OES, it is shown that the OH density in the plasma increases when Γ_G decreases (Fig. 4-1) which could therefore explain the appearance of γ - Al_2O_3 at low Γ_G . Indeed, as depicted on Fig. 4-1, the two aluminum lines recorded at 394.4 nm

and 396.2 nm follow the same monotonously increasing trend as Γ_G is increased. However, the aluminum line at 309.2 nm (white circles), presents a different behavior. As Γ_G is increased, the line intensity first decreases to a minimum at $\Gamma_G \sim 1.3$ and then increases. The observed trend may be due to overlapping of the Al line at 309.2 nm with the OH band head present at 308.9 nm. These two lines cannot be separated by the spectrometer employed in this study. The decrease in line intensity as Γ_G is increased can be understood by a decreased oxygen population in the plasma, as a consequence of increasing Γ_G . This notion is consistent with the previously discussed, concomitantly occurring decrease in line intensity of the AlO line at 467.2 nm. These results indicate that the process window for the synthesis of pure α -Al₂O₃ films is quite narrow and is defined by two competitive mechanisms, namely the ion bombardment and the incorporation of hydroxyl groups in the structure.

4.2.3 On the film morphology: role of chlorine content

Cross-sectional images of a pure α -Al₂O₃ (prepared with $\Gamma_G = 0.83$) and of a pure γ -Al₂O₃ sample (prepared with $\Gamma_G = 1.28$) are presented in Fig. 4-4a and 4b, respectively. Both films show a quite porous structure, where pores with different size distributions are observed. Fig. 4-4c and 3d represent magnified sections of Fig. 4-4a and 4b, respectively. In these images, pores with diameters of a few tens of nm, as well as larger pores with diameters of up to 2 μ m were observed. The micrometer size pores are sometimes open towards the surface, resembling the morphology of volcanoes. Actually, these larger pores may be responsible for the defects observed on the surface. If close enough to the surface and still closed, they form domes, while, if open, they form craters. Kurapov *et al.* have suggested that the formation of pores may be due to vacancy generation, migration and subsequent clustering and/or the

incorporation of Cl during growth, migration and subsequent Cl₂ bubble formation². These structures may be explained by gas (Cl₂) bubbles trapped in the film which could “explode” to form crater-like structures.

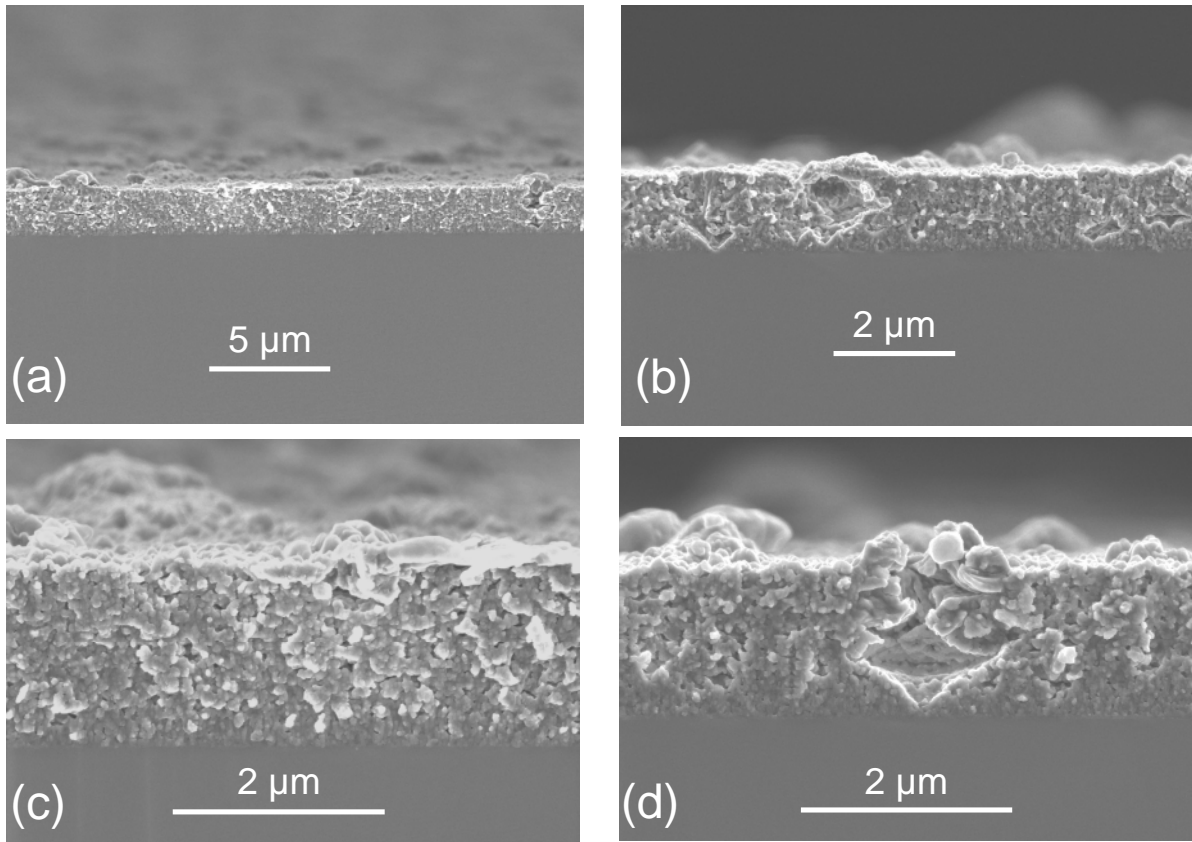


Fig. 4-4 Scanning electron microscopy images of (a) α -Al₂O₃ and (b) γ -Al₂O₃ film cross-sections. Images (c) and (d) represent α - and γ -Al₂O₃ film cross-sections at larger magnification.

To test this proposal, EDX analysis during scanning transmission electron microscopy (STEM) investigations of a γ -Al₂O₃ sample (Fig. 4-5) was performed. The solid lines in the STEM image Fig. 4-5a correspond to EDX line scans made at two different locations of the sample. The resulting concentration profiles are plotted in Fig. 4-5b. The signals of all of the observed chemical species (Al, O, Cl and Ar) as well as the total signal on the HAADF detector follow the same trend along the EDX line scans. The presence of discontinuities may be associated with the porous

4. Process-properties relation in PECVD alumina thin film

structure of the material. During acquisition of the line scan the electron beam traverses pores in the TEM lamellae. Comparing intensities obtained for the nominal thickness of lamellae of about 80-100 nm and in the regions around pores with a size of at least a few tens of nm in diameter, it appears likely that the crossed pores are open and therefore empty. No significant changes in Cl concentration can be seen in any of the 2 line scans. The changes in Al and O intensity reflect the presence of (open) pores, as indicated in the schematic drawing in Fig. 4-5c.

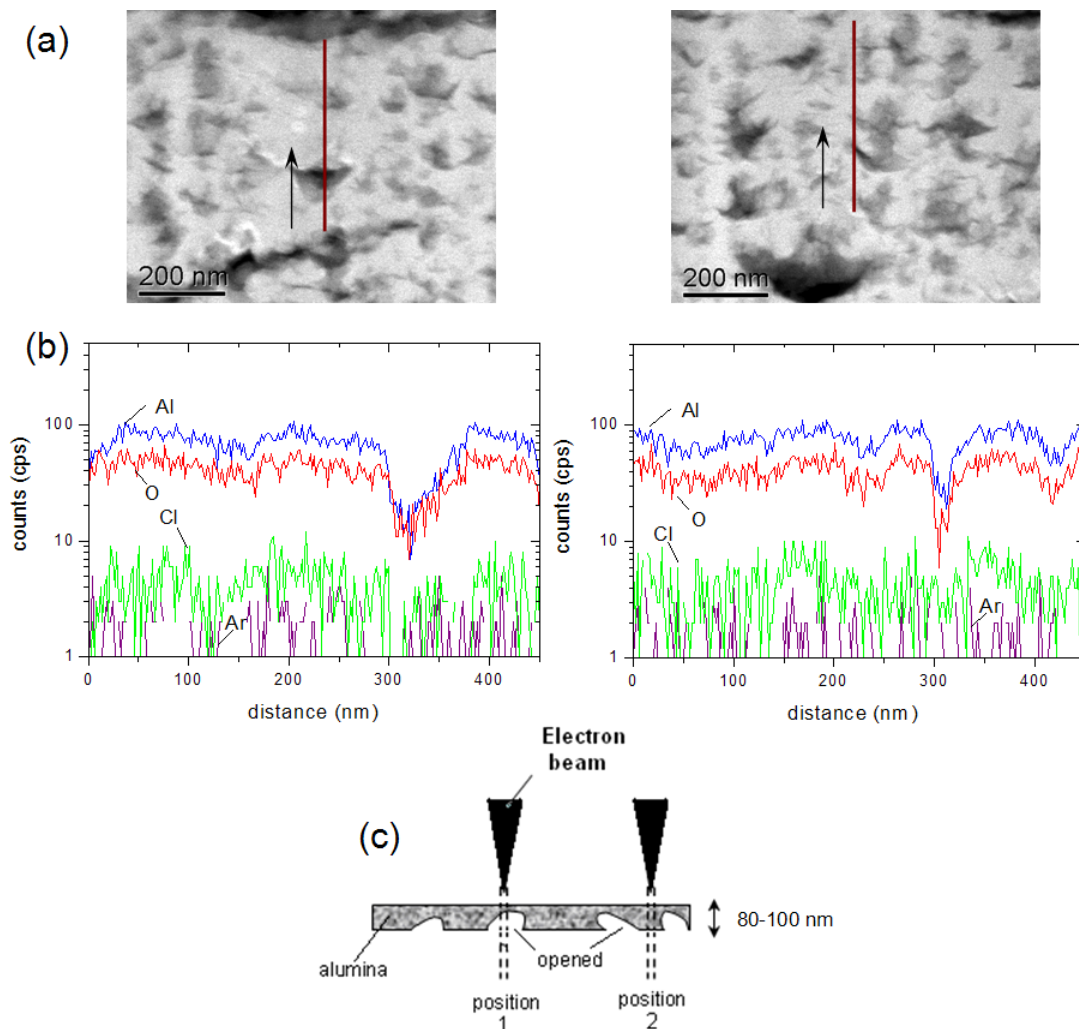


Fig. 4-5 Z-contrast image of the γ - Al_2O_3 sample. The EDX line scans were taken from top to bottom along the path indicated by the solid red lines. The total length of each line scan is 450 nm and a step size of 2 nm and a dwell time of 1 s. The dark regions in the image correspond to pores in the film. (b) Chemical composition data as obtained from the EDX line scans. (c) Schematic representation of the γ - Al_2O_3 sample.

These measurements yield no direct support for the presence of Cl_2 in the pores. Nevertheless, in all measurements a distinct signal indicating the presence of chlorine in the bulk is observed. This result supports the notion of chlorine incorporation in the $\gamma\text{-Al}_2\text{O}_3$ matrix. As suggested in our previous work², the formation of Cl_2 bubbles requires the presence of chlorine in the alumina matrix as well as sufficient energy to enable Cl mobility.

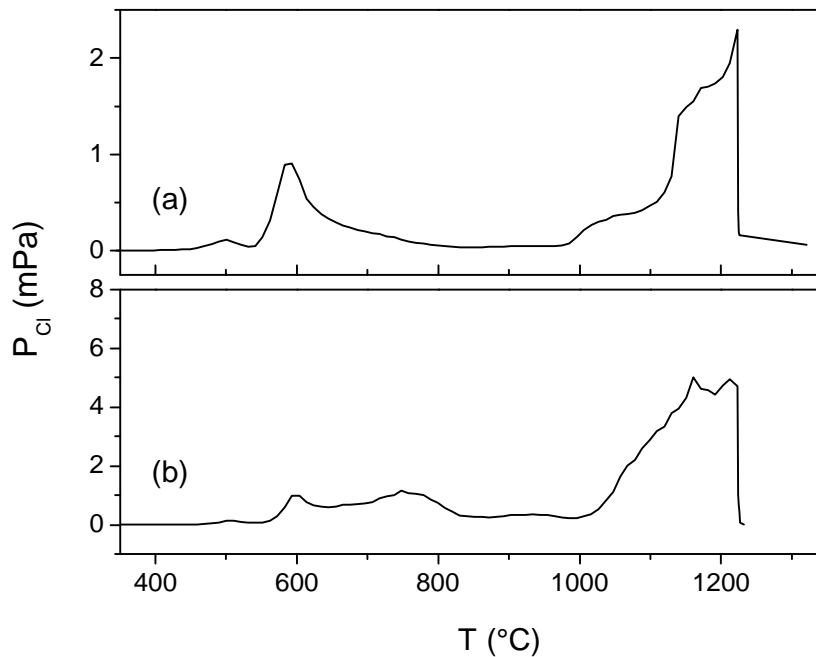


Fig. 4-6 Chlorine partial pressure versus temperature for (a) $\alpha\text{-Al}_2\text{O}_3$ and (b) $\gamma\text{-Al}_2\text{O}_3$ as obtained by Knudsen effusion mass spectrometry.

Desorption measurements were carried out to determine the temperature required for the mobilization and subsequent desorption of any Cl that was incorporated in the alumina films during growth. The chlorine partial pressure was measured versus temperature for both $\alpha\text{-Al}_2\text{O}_3$ (Fig. 4-6a) and $\gamma\text{-Al}_2\text{O}_3$ (Fig. 4-6b). Chlorine release from γ and $\alpha\text{-Al}_2\text{O}_3$ films occurs as the temperature is greater than 550°C , which was the growth temperature. Similar findings were reported by Badisch *et al.*, where Cl desorption was observed at $T > T_{\text{deposition}}$ for TiN films that were grown by PECVD from chloridic precursors¹⁰. In these TiN films, Cl incorporation during growth, as well

as Cl segregation at the grain boundaries have been reported¹⁰. It was demonstrated that the presence of Cl in TiN films enables the formation of a lubricious rutile phase in the tribological contact¹⁰. Chlorine release from γ - and α -Al₂O₃ films occurs additionally at a second onset temperature of approximately 1000 °C. These data support the notion of the presence of at least two different chlorine populations in γ - and α -Al₂O₃. The Cl release at the lower temperature may be related to surface desorption¹¹. It is possible to deconvolute the low-temperature desorption signal for γ -Al₂O₃ into two peaks, centered at ~600 °C and at ~750 °C. This is consistent with the previous absorption experiments of Cl on γ -Al₂O₃ surfaces, where two chlorine populations were reported¹². It has been suggested that these two populations may be due to different possible incorporation sites on γ -Al₂O₃ surfaces¹³. The reported activation energy of the dechlorination is about 10 – 30 kJ/mol^{11,12}. The Cl release at the higher temperature may be related to the activation of bulk diffusion and subsequent formation of Cl₂. The reported activation energy of Cl diffusion in either α -Al₂O₃ or in γ -Al₂O₃ is about 200 – 800 kJ/mol^{13,14}. The here presented desorption data are consistent with our notion of Cl induced formation of pores.

Tab. 4–1 Total energy (E) for all configurations studied

Polymorph	Cell	E (eV/atom)
α -Al ₂ O ₃	Pure	-7.549
	Cl (octahedral)	-7.180
	Cl (oxygen site)	-7.281
γ -Al ₂ O ₃	Pure	-7.505
	Cl (tetrahedral)	-7.179
	Cl (octahedral)	-7.191
	Cl (oxygen site)	-7.236
	2 apart vacancies (pure)	-7.505
	2 close vacancies	-7.445
	2 apart Cl	-6.923
2 close Cl	-7.063	

In order to test this hypothesis further, the energy penalty to incorporate Cl in γ - and α -Al₂O₃ by *ab initio* calculations was evaluated. The results are presented in Table 4–1. α -Al₂O₃ is by 0.044 eV/atom more stable than γ -Al₂O₃. This is consistent with previous work¹⁵. When Cl is incorporated in alumina (γ or α), the energy increases for all Cl positions probed. However, the energy differences obtained are comparable to other metastable phases, such as cubic Ti_{1-x}Al_xN and Cr_{1-x}Al_xN¹⁶, readily obtainable by plasma assisted growth techniques. The energetically most likely scenario for both α -Al₂O₃ and γ -Al₂O₃ is the substitution of an O atom by Cl. In this case, α -Al₂O₃ is still more stable than γ -Al₂O₃, since the energy penalty for incorporation of Cl is approx. 0.27 eV/atom for both phases. On the other hand, the incorporation of Cl on the octahedral of γ -Al₂O₃ (-7.191 eV/atom) is energetically more favorable than in octahedral sites of α -Al₂O₃ (-7.180 eV/atom). Finally, incorporation of Cl on the tetrahedral sites is only possible for γ -Al₂O₃ (-7.179 eV/atom) and is comparable in

stability to octahedral sites of $\alpha\text{-Al}_2\text{O}_3$. Based on these results, it seems that $\gamma\text{-Al}_2\text{O}_3$ can incorporate a larger amount of Cl than $\alpha\text{-Al}_2\text{O}_3$, since Cl can be incorporated at O positions, as well as at tetrahedral and octahedral sites. This is consistent with our EDX measurements.

Next, the interaction of two Cl atoms incorporated during growth was studied. Two vacancies and two chlorine atoms were introduced into the $\gamma\text{-Al}_2\text{O}_3$ cell. When vacancies agglomerate, the system becomes less stable, with an energy difference of 0.061 eV/atom. As the two Cl atoms interact a stability gain with an energy difference of -0.140 eV/atom is calculated. This may be the first step to Cl_2 molecule formation.

4.3 Influence of the pulse width

4.3.1 *On the plasma composition*

OES measurements have been carried out to monitor the plasma composition. The emission intensities related to several species present in the plasma versus Ω are reported in Fig. 4-7. It can be seen that the line intensities of Al and AlCl increase abruptly as Ω increases from 1.6 to 3. Increasing Ω further results only in a marginal intensity increase. The intensity increase measured for Al and AlCl can be interpreted qualitatively as the population increase of these two species in the plasma. It is reasonable to assume that this is due to a more efficient dissociation of the AlCl_3 precursor in the plasma¹⁷, since the H and Ar related line intensities also increase as Ω is increased from 1.6 to 3. Ion-surface interactions that result in the desorption/sputtering of Al and AlCl from the film surface as Ω is increased may also contribute to the intensity increase.

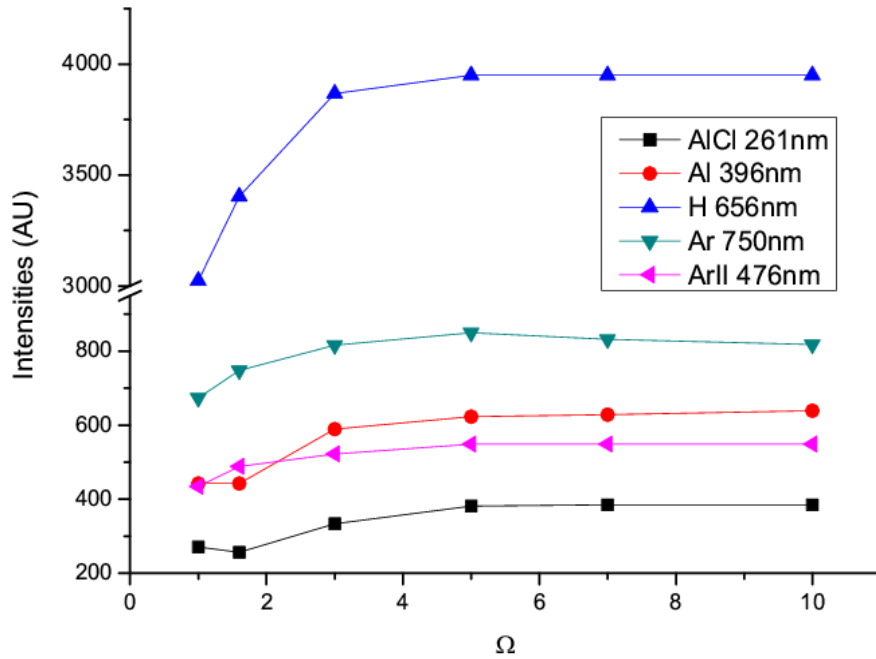


Fig. 4-7 Evolution of the line intensity of several selected plasma species with respect to Ω . The detector is saturated at 4000 with the H line.

4.3.2 On the film composition and phase constitutions

The film composition was obtained by EDX analysis. All the samples are stoichiometric (Al_2O_3) and chlorine is always incorporated. As presented on Fig. 4-8, the chlorine content decreases from ~ 2.4 at.% to 1.2 at.% as the Ω ratio is increased. From the presented measurements it is evident that the largest decrease in chlorine concentration is obtained as Ω is increased from 1.6 to 3. The chlorine content is reduced by $\sim 40\%$. As Ω is increased further, the slope of the Cl content versus Ω is decreased indicating that the reduction of the Cl concentration is less efficient at $\Omega \geq 3$. An approximately 20% concentration decrease is measured as Ω is increased from 3 to 10. This decrease may be understood based on Ω induced changes in plasma chemistry and ion-surface interactions.

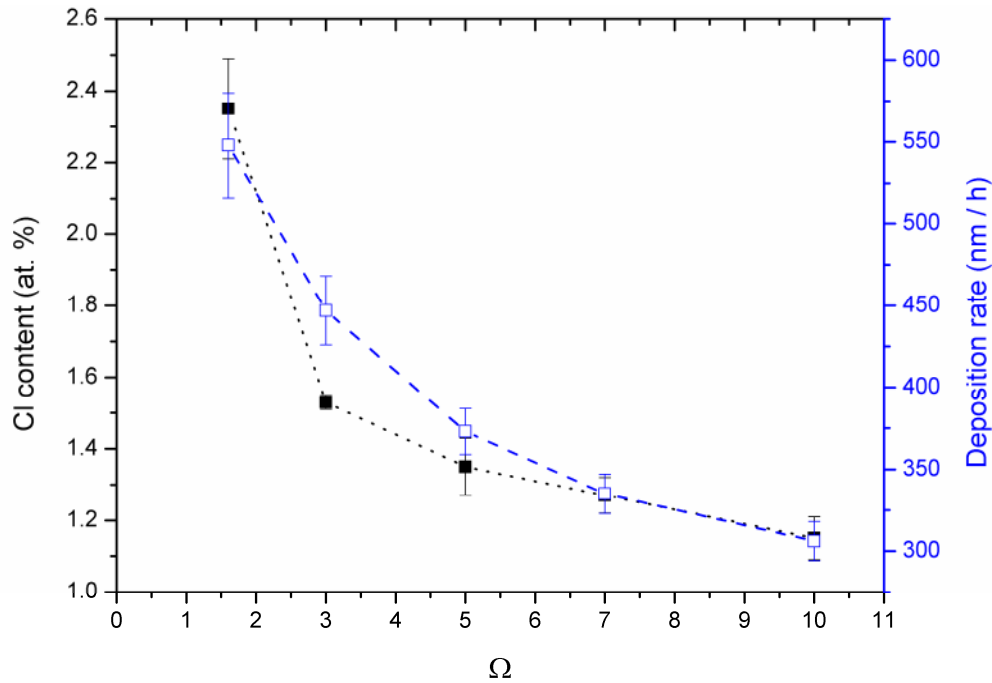


Fig. 4-8 The concentration of chlorine as determined by EDX (back squares) and the deposition rate (hollow squares), both presented as a function of Ω

It is interesting to note that the major population increase of Al and AlCl in the plasma occurs in the same Ω interval as the major decrease of chlorine concentration in the films. It is reasonable to assume that the more efficient precursor dissociation and/or ion-surface induced sputtering cause, at least in part, the reduced incorporation of Cl in the film as Ω is increased. Based on the model of Davis and Vanderslice¹⁸, the average ion energy can be estimated to be approximately 100 eV¹⁹. These ion-surface interactions may stimulate the desorption of Cl and Cl-containing species as well as sputtering thereof and hence reduce the Cl concentration of the as grown film. As Ω is increased the time when ion-surface interactions can occur is increased, resulting in a larger probability for sputtering and desorption of Cl and Cl-containing species. This notion is also consistent with the measured decrease of the Cl concentration in the films as Ω is increased. To validate this notion, a sample containing $\sim 2.4 \pm 0.1$ at.% of Cl was irradiated for a period of 15 minutes in a mixture of Ar – H₂ – O₂ at 150 Pa at room temperature. The discharge voltage was also set

to -900V and the resulting discharge current was 0.6 A. The Cl concentration was reduced to 1.8 ± 0.2 at.% indicating significant chlorine removal during ion bombardment.

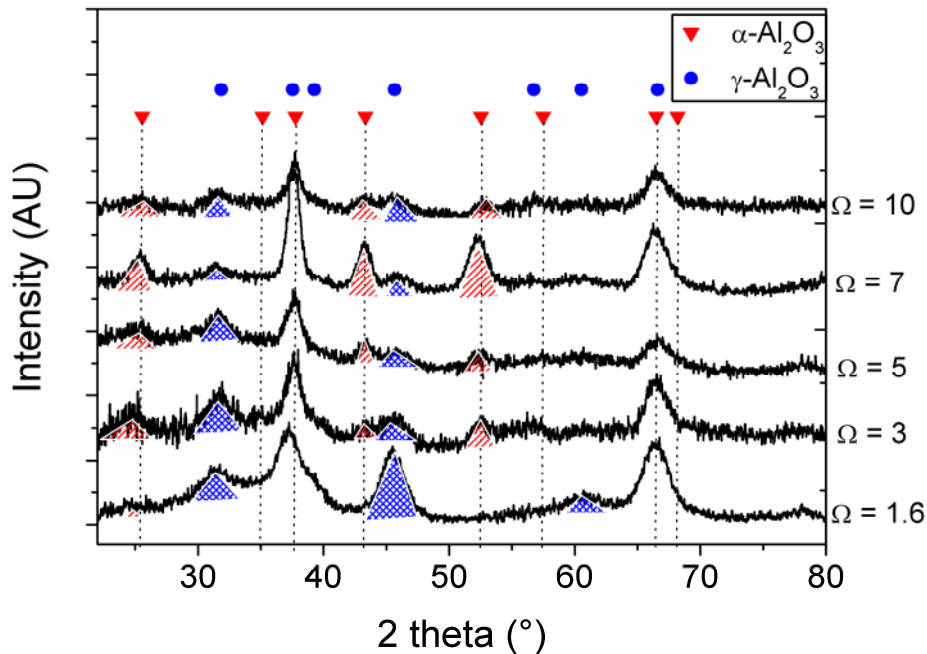


Fig. 4-9 Evolution of the XRD pattern with the Ω ratio. The peaks related to the α -structure are reported using dotted vertical lines.

The phase constitutions of the as deposited films are shown in Fig. 4-9. The Ω ratio clearly affects the phase constitution. A predominance of γ - Al_2O_3 is noticed for $\Omega = 1.6$, while the diffraction peaks originating from α - Al_2O_3 are dominating for $\Omega = 7$. A clear increase of α - Al_2O_3 constitution can be observed once Ω is increased from 1.6 to 7, since the peak intensities from α -phase increases. For the film grown at $\Omega = 10$, the α - Al_2O_3 constitution decreases further. It may be speculated that the ion flux induced formation of defects favours the preferred nucleation of the γ -phase. The grain size was estimated from the Sherrer equation and is approximately ~ 5 nm for both phases. Täschner *et al.*²⁰ reported a crystal size in the range of 10 nm for α - Al_2O_3 at a deposition temperature of 800°C. One should note that the increased Normalized Ion Flux (NIF) can eventually lead to an increase of the stress in the

4. Process-properties relation in PECVD alumina thin film

alumina films which in turn can result in an underestimation of the grain size when using the Sherrer formalism²¹.

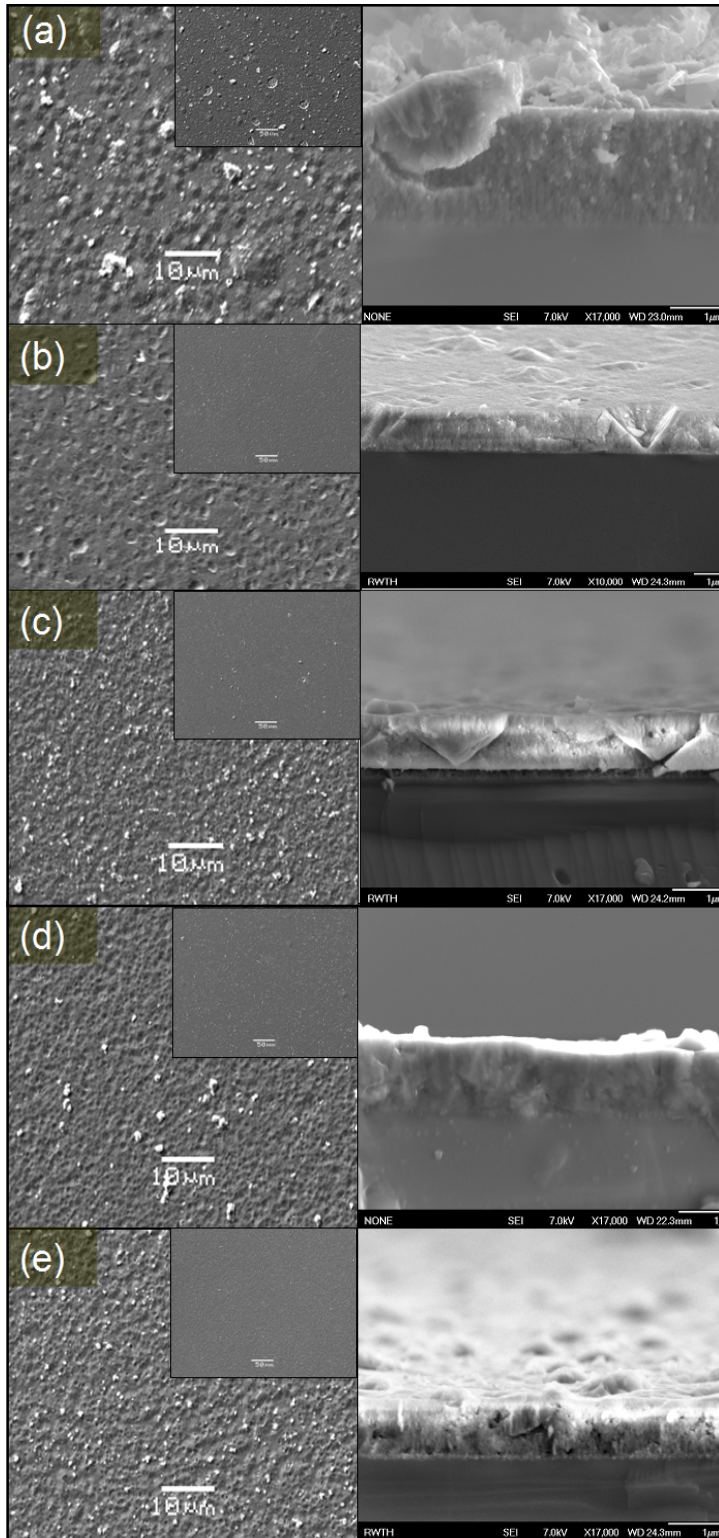


Fig. 4-10 SEM micrographs showing the evolution of the surface structure of the alumina films deposited at different Ω ratios. $\Omega = 1.6$ (a), 3 (b), 5 (c), 7 (d) and 10 (e). The surface topography is shown on the left hand side (lower magnification pictures are placed in insert) and the cross sectional view, as obtained with Field Emission SEM, is presented on the right hand side pictures

In Fig. 4-10 the topography of all films is shown. As Ω and the NIF are increased, the topography evolves from a rough surface featuring hillocks, cracks, and cohesive failure sites (Fig. 4-10a-c) to a surface which appears considerably smoother without growth defects characteristic for the topography of the $\Omega = 1.6$ and 3 films (Fig. 4-10d and 10e). Again, this observation is in accordance with the notion of increased ion bombardment as Ω is increased.

4.4 Low temperature synthesis of α -Al₂O₃ films by high power plasma assisted chemical vapor deposition

4.4.1 Plasma characterization and modeling

Measurements of the time dependent current (I) and voltage (U) of a discharge operating at a pulse width of 80 μ s and a frequency of 5 kHz are shown in Fig. 3-2. Both current and voltage exhibit constant values during the nominal pulse on-time (80 μ s). As the pulse is switched off, current and voltage decay over approx. 70 μ s towards zero. In the following text the magnitudes of current and voltage refer to the values measured during the pulse on-time. The I-U curve of a discharge operating at a pulse width of 80 μ s and a frequency of 5 kHz is presented in the insert in Fig. 4-11. The increase of the voltage results in a close to linear increase of the current in the voltage range from 0.5 to 1.4 kV. The vertical dotted line (insert in Fig. 4-11) separates the previously studied current-voltage-range^{1,8,22} from the range investigated here. The extension of the voltage range from 0.9 kV up to 1.4 kV results in power densities (calculated by dividing the power to the area of the cathode) up to 19 W/cm², which are approx. 4 times larger than those reported previously^{1,8,22}.

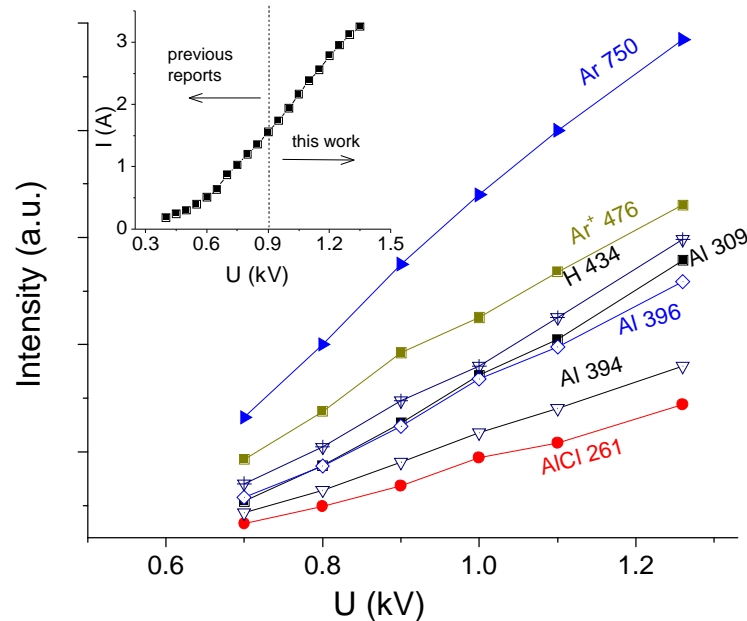
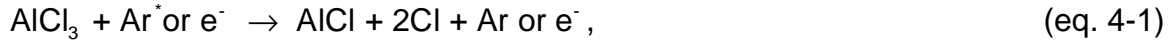


Fig. 4-11 The intensity of the various emission lines versus the discharge voltage. The insert shows current-voltage curves recorded from the discharge operating the pulse width of $80 \mu\text{s}$ and a frequency of 5 kHz.

The increase of the power density affects the plasma composition, as determined from the OES data shown in Fig. 4-11. The emission intensity of all lines increases as the discharge voltage and hence the cathode power density is increased. This may be consistent with an increase of the electron density and/or temperature, since the line intensity is proportional to the number density of excited atoms which in turn is related to the number density of the considered atoms in their ground states and to the density of the energetic particle responsible for the excitation. For instance, the energetic particle can be either an electron or an argon metastable atom (Ar^*). As the voltage is increased, it is reasonable to assume that electrons will acquire more energy from the applied electric field resulting in a more efficient dissociation and ionization of the plasma species. As reported in Fig. 4-11, the line intensity of the Ar 750 nm line versus the applied voltage increases. The low energy level of this transition is related to the $3P_0$ and $3P_2$ metastable levels of the argon atom. Hence it is reasonable to assume that the increase of the line intensity indicates an increased population of metastable Ar (Ar^*) as the discharge voltage is increased.

Consequently, more Ar* would be available for dissociating the precursor. Zheng *et al.* reported that in an inductively coupled discharge the presence of Ar* leads to efficient AlCl₃ precursor dissociation²³. Generally, these dissociation processes can be described by the following reaction:²³



which leads to the formation of Al through the reaction



Therefore, the increase of the emission intensity of precursor related Al and AlCl lines in Fig. 4-11 should not only be attributed to the electron temperature and density increase, but also to the enhancement of the dissociation by impact of Ar*. Enhanced dissociation of BCl₃ has also been reported upon increasing the discharge power in a PECVD plasma²⁴.

Apart from its effect on the plasma composition, the increase of the cathode voltage to 1.3 kV leads to an up to two times larger discharge current as compared to the 0.9 kV discharge, as shown in the insert in Fig. 4-11, increasing the ion flux impinging on the growing film surface. In addition, the increase of the voltage implies a larger potential drop across the cathode sheath which in turn has implications for the energy of the ions impinging on the film. Due to the relatively high pressure of the discharge (175 Pa), ion-neutral and ion-electron collisions occur in the sheath²⁵. Hence, the average ion energy is lower than the energy that can be gained by acceleration across the cathode fall. The ion energy distribution function (IEDF) was estimated based on the Davis and Vanderslice model²⁵ considering charge exchange collisions in the sheath. The ion energy distribution function is then given by the following expression:

$$2\lambda L \cdot \frac{U_c \cdot dN}{N_0 \cdot dU} = \frac{1}{2\sqrt{1-U/U_c}} \cdot \exp\left[-L/\lambda \cdot (1-\sqrt{1-U/U_c})\right], \quad (\text{eq. 4-3})$$

where L/λ is ratio between sheath thickness and mean free path for charge exchange collisions, N_0 is the total number of ions at the sheath edge, and U_c is the potential difference across the sheath, i.e. the cathode potential. Here for simplicity an Ar-H₂ plasma with a pressure of 175 Pa was evaluated, since Ar and H₂ constitute ~97% of the gas atmosphere. IEDFs were calculated using eq. 4-3 for pure Ar and H₂ plasmas and are plotted in Fig. 4-12 (solid lines). For the calculation of λ in eq. 4-3, the cross sections for Ar-Ar⁺ (3×10^{-15} cm²) and H₂-H₂⁺ (8×10^{-16} cm²) charge-exchange collisions were employed for Ar and H₂ plasma, respectively^{26,27}. The sheath thickness L was estimated based on the Child-Langmuir law to be 1 mm and 8 mm for Ar plasma and H₂ plasma, respectively²⁸. The dashed curve in Fig. 4-12 corresponds to a plasma that consists of 85% of H₂ and 15% of Ar and was obtained by averaging the data from the H₂ and Ar plasma IEDFs using the respective weighting coefficients 0.85 and 0.15. These conditions are close to our experimental plasma conditions and show that the IEDF exhibits a low populated high energy tail starting from energies that correspond to a value of $1/3U_c$, while the majority of the species exhibit energies that correspond to values of below $1/4U_c$. Furthermore, the average ion energy determined by integration of the IEDF gives a value of $0.16 U_c$. Therefore, as U_c is increased from 0.9 to 1.3 kV, the mean average ion energy increases from ~140 to ~200 eV. The increase of the energy and the flux of the ions towards the growing film surface result in a more intense energetic bombardment.

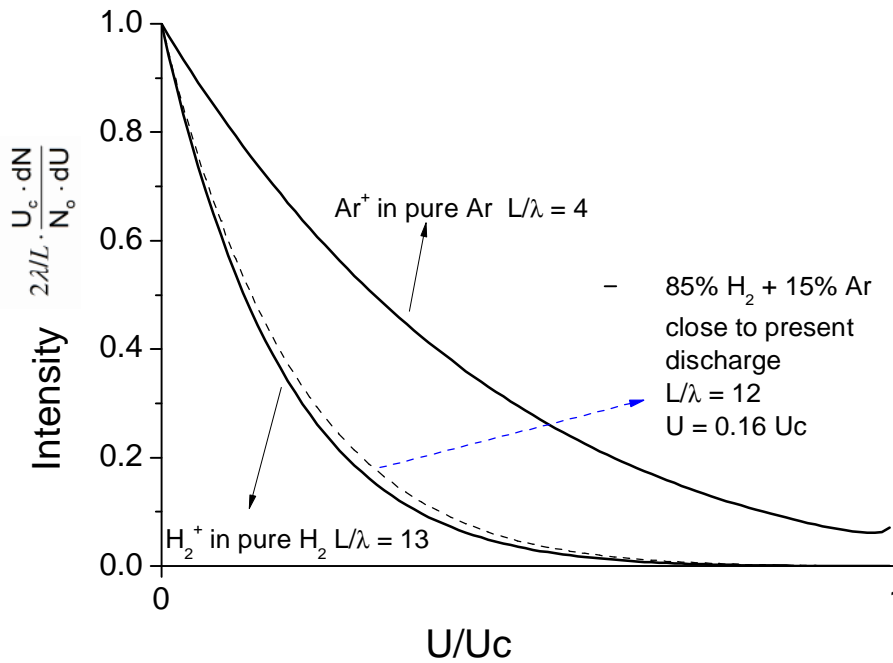


Fig. 4-12 Ion energy distribution functions for pure Ar and H₂ plasmas (solid lines) and a plasma consisting of 85% H₂ and 15% Ar (dashed line).

4.4.2 Structure and elastic properties of films

In Fig. 4-13, the XRD patterns of films grown at various cathode potentials are presented. At 0.9 kV cathode potential the formation of a mixture of γ - and α -Al₂O₃ is observed. As the voltage is increased to 1.1 kV, phase pure α -Al₂O₃ films are obtained. The increase of the voltage enhances the crystallinity of the α -Al₂O₃ phase as manifested by the decrease of the full width at half maximum (FWHM) of the XRD peaks. As shown in Fig. 4-14, FWHMs of peaks at 2θ angular positions of 25.6°, 37.8°, 43.3°, and 52.5°, obtained by Gaussian fitting, show a decrease by 30-50%, when the discharge voltage increases from 0.9 to 1.3 kV. Meanwhile, a clear appearance/separation of peaks at 2θ positions of 35.1° and 68.2° is also observed in Fig. 4-13 at a voltage of 1.1 and 1.3 kV, also indicating improved crystal quality. Furthermore, an increase of the pulse width from 80 to 100 μ s (demonstrated for voltages of 1.1 and 1.3 kV in In Fig. 4-13) leads to a decrease of the FWHM of the α -

Al_2O_3 peaks by 5~10% (see In Fig. 4-14) and subsequently to an improved crystallinity. The $\alpha\text{-Al}_2\text{O}_3$ formation and improvement of crystallinity thereof can be attributed to the increased average ion energy as discussed in the pervious paragraph as well as to the increase in duration of ion bombardment enabling surface diffusion^{6,8,22,29}. It has to be mentioned here that due to the high plasma density at the voltage and pulse width of 1.3 kV and 100 μs , respectively, the substrate temperature was 590 ± 10 °C, although no external heating was applied. The deposition temperature for all other films was 560 ± 10 °C.

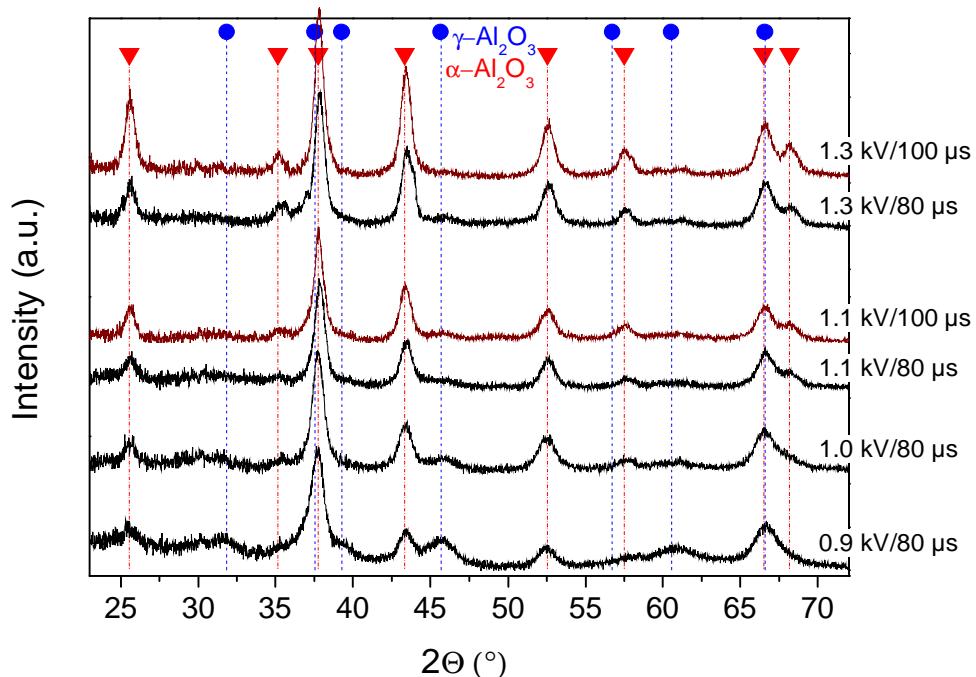


Fig. 4-13 X-ray diffraction patterns of Al_2O_3 films deposited at various discharge voltages and pulse widths. The inverse triangles and the circles indicate the positions of the diffraction peaks associated with the presence of $\alpha\text{-Al}_2\text{O}_3$ and $\gamma\text{-Al}_2\text{O}_3$, respectively.

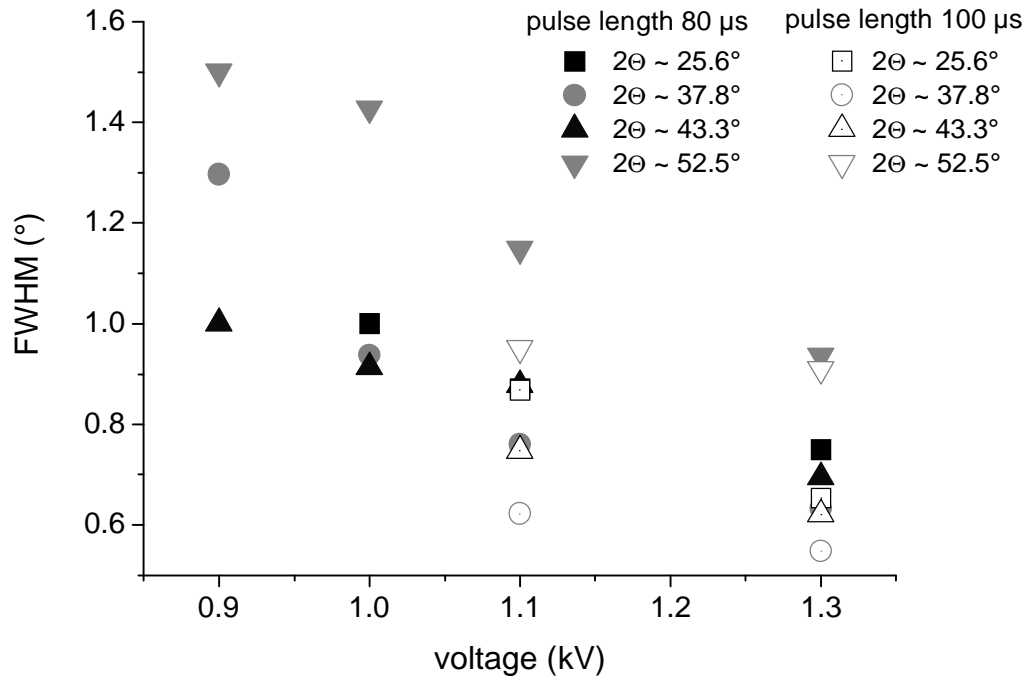


Fig. 4-14 The full width at half maximum (FWHM) of chosen diffraction peaks as a function of various discharge voltages and pulse widths. Due to difficulty of peak fitting, data from sample deposited at 0.9 kV/80 μs at $2\theta \sim 25.6^\circ$ are not shown.

Along with the change of the phase composition and the improvement of the crystallinity, a continuous decrease of the Cl incorporation from 1.1 to 0.5 at.% is observed as the voltage is increased from 0.9 to 1.3 kV. This may be understood by considering recently published Cl desorption data by Snyders *et al.*¹, where Cl release from $\alpha\text{-Al}_2\text{O}_3$ films was measured during annealing at temperatures larger than the deposition temperature. This indicates that desorption of Cl may also be expected during deposition as the energy at the surface of the growing film is increased for example due to enhanced ion bombardment. Cl desorption during growth in turn results in a decreased Cl concentration in the film, which is again consistent with the experimental observation. Recently published *ab-initio* data¹ clearly indicate that the presence of Cl destabilizes $\alpha\text{-Al}_2\text{O}_3$, which underlines the novelty of the here reported process where the Cl concentration could be decreased by an increase of the energy and the flux of the bombarding species towards the growing film, as well as in a more efficient AlCl_3 dissociation. As the discharge

voltage is increased, the Cl incorporation is reduced and the formation of the $\alpha\text{-Al}_2\text{O}_3$ phase is observed. Similar behavior is also obtained for the films grown at a pulse width of 100 μs . At the same time the deposition rate was found to decrease from 0.5 $\mu\text{m/h}$ at a voltage of 0.9 kV to 0.36 $\mu\text{m/h}$ at a voltage of 1.3 kV (pulse width of 80 μs in both cases) which could be associated with the increase of resputtering and density of deposited film at elevated voltage.

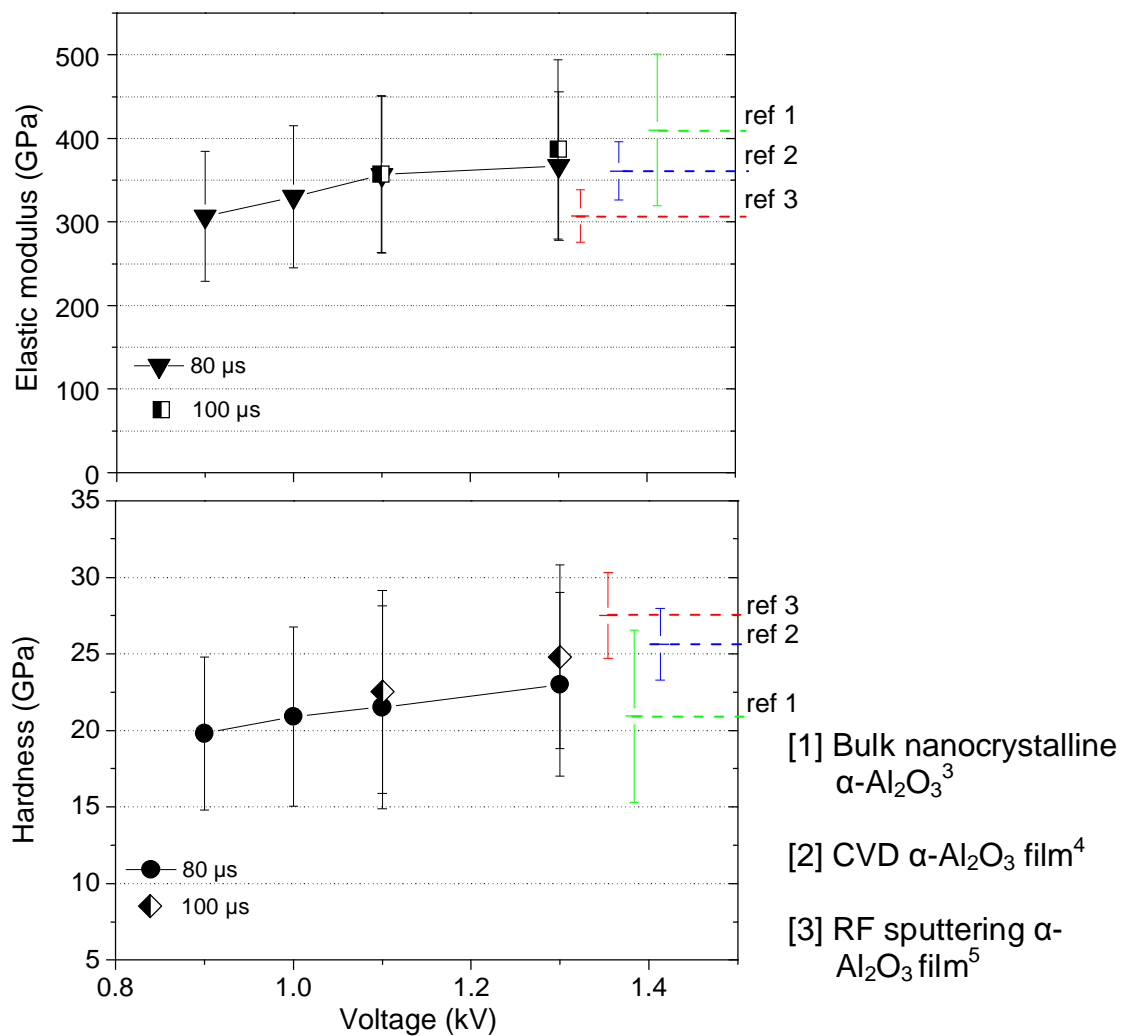


Fig. 4-15 Elastic modulus (upper) and hardness (lower) of Al_2O_3 films as a function of the discharge voltage. The insert is a top view and the cross section SEM micrograph from a film deposited at a discharge voltage of 1.3 kV and a pulse width of 100 μs .

On the other hand, the change of the pulse width from 80 to 100 μs had no measurable implications for the deposition rate. The elastic modulus (E) and hardness (H) of the deposited films are plotted versus the voltage in Fig. 4-15. The quantities E and H increase as the voltage is increased. The highest values for E (~ 380 GPa) are obtained for the films synthesized at a voltage of 1.3 kV and are very similar to that of CVD grown $\alpha\text{-Al}_2\text{O}_3$ ⁴ and bulk ceramic $\alpha\text{-Al}_2\text{O}_3$ ³, as indicated by the horizontal dashed lines in Fig. 4-15. A top view (a) and a cross sectional (b) SEM micrographs of this film are presented in Fig. 4-16a and 16b, respectively. These images show a smooth surface and a dense morphology, which can be understood by the formation of phase pure $\alpha\text{-Al}_2\text{O}_3$ with a density close to the bulk value. This is a consequence of ion bombardment at elevated cathode voltage, causing both a larger flux and larger average ion energy as compared to conventional PECVD synthesis approaches.

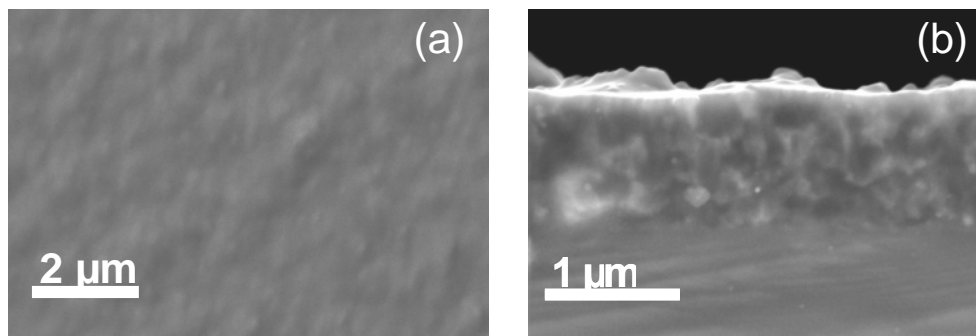


Fig. 4-16 A top view (a) and a cross section (b) SEM micrograph from a film deposited at a discharge voltage of 1.3 kV and a pulse width of 100 μs .

4.5 Conclusions

Depending on the AlCl_3/O_2 precursor ratio employed during PECVD, it has been shown that $\alpha\text{-Al}_2\text{O}_3$ is obtained for a low precursor ratio at large ion bombardment. The α - and $\gamma\text{-Al}_2\text{O}_3$ films contain about 1.0 and 2.0 at.% of residual Cl, respectively.

Using optical emission spectroscopy measurements, it is found that Cl incorporation may be due to incomplete dissociation of the AlCl_3 precursor. With EDX and TEM measurements, the presence of pores and incorporated chlorine in the alumina matrix was observed. Although a direct evidence of Cl_2 in the pores was not observed, the desorption data support the notion of Cl migration and the *ab initio* data show that the agglomeration of two Cl atoms in the matrix results in an energetically more favorable configuration. Hence, the *ab initio* and the desorption data are consistent with the Cl induced pore formation proposal.

As the pulse ON/OFF ratio (Ω) was increased from 1.6 to 10, the Cl concentration was decreased by 50%, to 1.2 ± 0.1 at.%, which may be a consequence of both, more efficient dissociation of the AlCl_3 precursor in the plasma as well as ion bombardment induced desorption of Cl-containing species from the growing film surface. These notions are consistent with Optical Emission Spectroscopy data and with the reduced deposition rate as Ω and hence the NIF are increased. The increase of Ω also leads to the formation of denser films with a smoother surface. For $\Omega = 7$, a film density of $3.85 \pm 0.12 \text{ g/cm}^{-3}$ is measured corresponding to 96.7 % of the bulk density and an elastic modulus of $365 \pm 50 \text{ GPa}$ (corresponding to 83 % of the bulk value) is obtained for a corresponding deposition rate of $335 \pm 12 \text{ nm/h}$. It is shown that the low temperature growth of protective alumina films with increased density and stiffness is enabled by increasing the pulse ON/OFF time ratio (Ω). This can be understood by the Ω induced increase in precursor dissociation and increase in normalized ion flux.

Finally, a novel generator which is able to deliver approx. 4 times larger power densities than those conventionally employed during PECVD was utilized. Plasma analysis and modeling indicate that the larger discharge power density enables a

significant increase of the AlCl_3 precursor dissociation efficiency, as well as an increased ion flux towards the growing film. These conditions enable the deposition of smooth and dense $\alpha\text{-Al}_2\text{O}_3$ films with negligible Cl incorporation and elastic properties similar to those of the bulk $\alpha\text{-Al}_2\text{O}_3$ at a growth temperature of 560 ± 10 °C.

- ¹ R. Snyders, K. Jiang, D. Music, S. Konstantinidis, T. Markus, A. Reinholdt, J. Mayer, J. M. Schneider, Surf. Coat. Technol. **204**, 215-221 (2009).
- ² D. Kurapov, J. Reiss, D. H. Trinh, L. Hultman, J. M. Schneider, J. Vac. Sci. Technol. A **25**, 831-836 (2007).
- ³ J. H. Gong, Z. J. Peng, H. Z. Miao, J. Eur. Ceram. Soc. **25**, 649-654 (2005).
- ⁴ D. Hochauer, C. Mitterer, M. Penoy, C. Michotte, H. P. Martinz, M. Kathrein, Surf. Coat. Technol. **203**, 350-356 (2008).
- ⁵ J. M. Andersson, Z. Czigan, P. Jin, U. Helmersson, J. Vac. Sci. Technol. A **22**, 117-121 (2004).
- ⁶ E. Wallin, E. P. Munger, V. Chirita, U. Helmersson, J. Phys. D: Appl. Phys. **42**, 125302 (2009).
- ⁷ D. Kurapov, Ph.D Thesis, RWTH Aachen University (2005).
- ⁸ O. Kyrylov, D. Kurapov, J. M. Schneider, Appl. Phys. A **80**, 1657-1660 (2005).
- ⁹ C. Täschner, B. Ljungberg, V. Alfredsson, I. Endler, A. Leonhardt, Surf. Coat. Technol. **108-109**, 257-264 (1998).
- ¹⁰ E. Badisch, C. Mitterer, P. H. Mayrhofer, G. Mori, R. J. Bakker, J. Brenner, H. Stori, Thin Solid Films **460**, 125-132 (2004).
- ¹¹ M. Stoiber, E. Badisch, C. Lugmair, C. Mitterer, Surf. Coat. Technol. **163-164**, 451-456 (2003).
- ¹² F. Arena, F. Frusteri, N. Mondello, N. Giordano, A. Parmaliana, J. Chem. Soc., Faraday Trans. **88**, 3353-3356 (1992).
- ¹³ R. J. He, M. Rohner, W. Richarz, Thermochim. Acta **102**, 349-356 (1986).
- ¹⁴ M. C. Rohner, V. K. Sharma, W. Richarz, Can. J. Chem. Eng. **67**, 513-515 (1989).
- ¹⁵ G. Gutiérrez, A. Taga, B. Johansson, Phys. Rev. B **65**, 012101 (2002).

- 16 P. H. Mayrhofer, D. Music, T. Reeswinkel, H. G. Fuss, J. M. Schneider, *Acta Mater.* **56**, 2469-2475 (2008).
- 17 J. Zheng, B. Sun, R. Yang, X. Song, X. Li, Y. Pu, *J. Phys. Chem. B*, 12748–12752 (2008).
- 18 W. D. Davis, T. A. Vanderslice, *Phys. Rev.* **131**, 219 (1963).
- 19 O. Kyrylov, D. Kurapov, J. M. Schneider, *Appl. Phys. A* **80**, 1657-1660 (2005).
- 20 C. Taschner, B. Ljungberg, I. Endler, A. Leonhardt, *Surf. Coat. Technol.* **116-119**, 891–897 (1999).
- 21 T. H. d. Keijser, J. I. Langford, E. J. Mittemeijer, A. B. P. Vogels, *Journal of Applied Crystallography* **15**, 308-314 (1982).
- 22 S. Konstantinidis, K. Jiang, J. M. Schneider, unpublished (2010).
- 23 J. Zheng, B. Sun, R. Yang, X. B. Song, X. G. Li, Y. K. Pu, *J. Phys. Chem. B* **112**, 12748-12752 (2008).
- 24 R. Ramos, G. Cunge, M. Touzeau, N. Sadeghi, *J. Phys. D: Appl. Phys.* **41**, 115205 (2008).
- 25 W. D. Davis, T. A. Vanderslice, *Phys. Rev.* **131**, 219 (1963).
- 26 G. Ecker, K. G. Müller, *Z. Naturforsch., A: Phys. Sci.* **16**, 246-252 (1961).
- 27 J. A. Dillon, W. F. Sheridan, H. D. Edwards, S. N. Ghosh, *J. Chem. Phys.* **23**, 776-779 (1955).
- 28 I. Langmuir, *Phys. Rev.* **21**, 419-435 (1922).
- 29 T. Kohara, H. Tamagaki, Y. Ikari, H. Fujii, *Surf. Coat. Technol.* **185**, 166-171 (2004).

5 ON THE STABILITY OF γ -ALUMINA

*The thermal stability of γ -Al₂O₃ films grown by PECVD and Filtered Cathodic Arc (FCA) approaches has been investigated using annealing experiments. In addition, *ab initio* calculations of the phase stability and electronic structure for γ -Al₂O₃ with different alloying elements are also presented.*

5.1 Introduction

In the present study, the phase stability of γ -Al₂O₃ films is explored experimentally as well as theoretically. On one side, the high temperature stability of γ -Al₂O₃ films deposited on Ti_{0.33}Al_{0.67}N coated WC-Co cutting inserts was investigated. The choice of Ti_{0.33}Al_{0.67}N/WC-Co as a substrate is motivated by its wide utilization in cutting and forming processes. γ -Al₂O₃ films are deposited using two industrially relevant plasma based deposition techniques, namely FCA and PECVD. A variety of characterization techniques are employed in order to investigate the effect of temperature, chemical composition, microstructure and morphology on the stability of Ti_{0.33}Al_{0.67}N coated WC-Co cutting inserts. The results of these investigations are combined with studies of the phase stability of γ -Al₂O₃ in the form of film and powder. This research strategy enables us to elucidate the effect of the γ -Al₂O₃ film and the substrate on the high temperature stability of γ -Al₂O₃/substrate systems. For operation at high temperatures the challenge is to identify ways to impede or exclude structural transitions. Doping metastable polymorphs has been explored experimentally and it was found that additives in the γ -Al₂O₃ structure affected the thermal stability thereof. Therefore, on the other hand, *ab initio* calculations are performed to evaluate the

influence of Si, Sc, Ti, Cr, and Y additives on the phase stability and electronic structure of γ - and α - Al_2O_3 using density functional theory. Due to importance of stiffness from an application point of view, the elastic properties of alloyed γ - Al_2O_3 are also investigated. Regarding the γ - Al_2O_3 structure, a comparison between two structure proposals based on cubic spinel and tetragonal hausmannite was carried out.

5.2 On the high temperature stability of vapor deposited γ - Al_2O_3 films

5.2.1 Thermal stability of the film/substrate system

The effect of the temperature on the phase stability of the film/substrate system was investigated by annealing samples grown on $\text{Ti}_{0.33}\text{Al}_{0.67}\text{N}$ coated WC-Co cutting inserts in air for 1 hour at temperatures ranging from 800 to 1000 °C. The grazing incident X-ray diffraction patterns (GIXRD) recorded from as deposited and annealed FCA and PECVD grown films are presented in Fig. 5-1a and 1b, respectively. Maxima (peaks) in the scattered x-ray intensity at angular (2θ) positions of 45.7° and 66.5° can be seen in the patterns of the as deposited FCA and PECVD films. These peaks are assigned to the (400) and (440) diffraction planes of the γ - Al_2O_3 crystal structure, respectively¹. In addition, peaks that originate from the $\text{Ti}_{0.33}\text{Al}_{0.67}\text{N}$ interlayer and the WC substrate² are also observed. As $\text{Ti}_x\text{Al}_{1-x}\text{N}$ forms a metastable solid solution, its diffraction peaks are located between those of the cubic- AlN ³ and the cubic- TiN ⁴. Peaks of the γ - phase are the only Al_2O_3 peaks in the patterns of the FCA films up to an annealing temperature of 900 °C, while annealing at 1000 °C results in the appearance of α - Al_2O_3 ⁵ peaks at 2θ values of 25.5°, 35.1°, 43.3°, 57.5°,

5. On The stability of alumina

and 68.2°. In the case of PECVD grown films the γ -phase peaks are the only Al_2O_3 peaks up to a temperature of 800 °C. Both γ - and α - Al_2O_3 peaks can be observed at 900 °C, while the α - Al_2O_3 peaks dominate the XRD pattern at 1000 °C. Moreover, at 1000 °C strong peaks at 27.4°, 36.1°, 41.2°, 54.3°, and 56.6° that can be assigned to the rutile- TiO_2 phase² are detected for both FCA and PECVD samples.

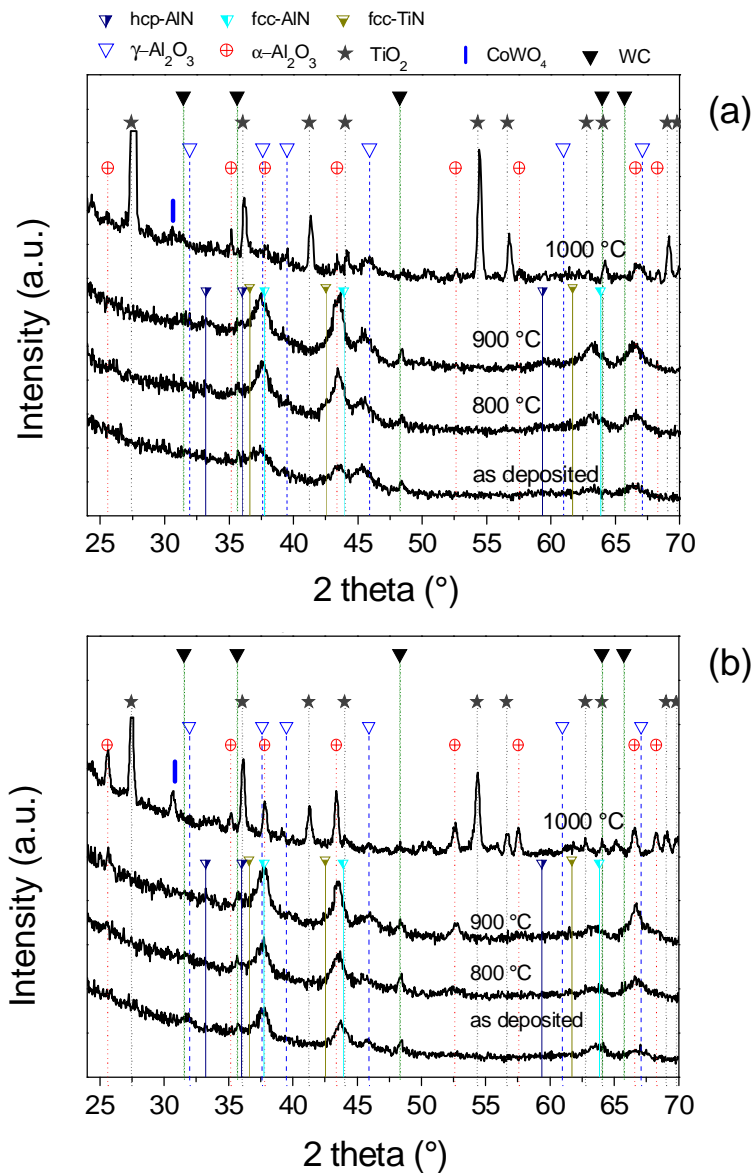


Fig. 5-1 Grazing incidence XRD patterns of as deposited and annealed in air (a) FCA and (b) PECVD films. The horizontal lines indicate the peak position in unstrained bulk γ - Al_2O_3 , α - Al_2O_3 , cubic-TiN, cubic-AlN, rutile- TiO_2 , WC, and CoWO_4 (see legend for more information).

Additional information regarding the morphology, structure as well as the chemical composition of the films and the substrate was obtained by the SEM and TEM analysis. The cross-sectional SEM images of as deposited FCA and PECVD grown films are presented in Fig. 5-2a and 2b, respectively. The FCA film exhibits a dense microstructure and a smooth surface, while the PECVD film exhibits a porous morphology with rough topography.

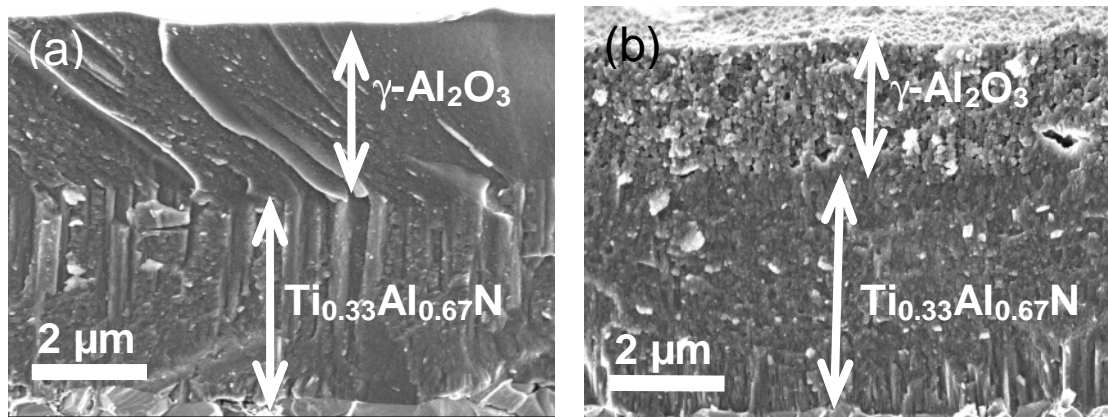


Fig. 5-2 Cross sectional SEM images as deposited (a) FCA sample (b) PECVD sample.

The cross sectional TEM images of the FCA and PECVD samples after annealing at 900 °C are presented in Fig. 5-3a and 3b, respectively. Both films retain their original morphology with a sharp $\text{Al}_2\text{O}_3/\text{Ti}_{0.33}\text{Al}_{0.67}\text{N}$ interface. Selected area electron diffraction (SAED) patterns recorded from the marked regions of the film and the film/substrate interface are also shown in Fig. 5-3. For the FCA film (region 1 in Fig. 5-3a) diffraction rings that correspond to the $\gamma\text{-Al}_2\text{O}_3$ phase are observed. No evidence for the presence of $\alpha\text{-Al}_2\text{O}_3$ was observed by SAED or XRD. In the PECVD case (region 1 in Fig. 5-3b) diffraction rings and single crystal diffraction patterns are observed corresponding to the $\gamma\text{-Al}_2\text{O}_3$ phase and electron diffractions along with $[\bar{1}82]$ zone axis of $\alpha\text{-Al}_2\text{O}_3$, respectively. In addition, in region 1 in Fig. 5-3b an $\alpha\text{-Al}_2\text{O}_3$

Al_2O_3 grain with a size of ~ 100 nm in the $\gamma\text{-Al}_2\text{O}_3$ matrix can be seen (zoomed in insert). This is an indication for nucleation and abnormal growth of $\alpha\text{-Al}_2\text{O}_3$ grains in the $\gamma\text{-Al}_2\text{O}_3$ matrix. These findings are consistent with the results obtained by the GIXRD measurements (Fig. 5-1). However, the present observations do not support Bobzin's suggestion that the transformation of γ to α starts at the interface of $\gamma\text{-Al}_2\text{O}_3/\text{Ti}_x\text{Al}_{1-x}\text{N}$ ⁶. At the same time, SAED patterns recorded at the $\text{Al}_2\text{O}_3/\text{Ti}_{0.33}\text{Al}_{0.67}\text{N}$ interface for both FCA and PECVD films (region 2 in Fig 5-3a and 3b, respectively) exhibit Al_2O_3 rings as well as rings that correspond to the cubic-TiN and the hexagonal-AlN phase, indicating decomposition of the $\text{Ti}_{0.33}\text{Al}_{0.67}\text{N}$ interlayer. These data are in consistence with the previous reports that $\text{Ti}_x\text{Al}_{1-x}\text{N}$ decomposes into cubic-TiN and cubic-AlN, which finally transforms into the hexagonal-AlN⁷⁻⁹. It has to be mentioned here that the temperature at which hexagonal-AlN is detected (900°C) is significantly lower than the values reported in the literature ($<1030^\circ\text{C}$) for $\text{Ti}_{0.33}\text{Al}_{0.67}\text{N}$ films^{7,10}. It is suggested that this may be due to the long isothermal heating stage employed in our annealing experiments as well as due to the low heating and cooling rate of 5 K min^{-1} as compared to 50 K min^{-1} from ref.7.

Fig. 5-3 (c) shows the results of the STEM-EDX line scan across the $\text{Al}_2\text{O}_3/\text{Ti}_{0.33}\text{Al}_{0.67}\text{N}$ interface of a PECVD film annealed at 900°C . There it is to be seen that ~ 100 nm before the transition from the Al_2O_3 to the $\text{Ti}_{0.33}\text{Al}_{0.67}\text{N}$ film, which occurs at a relative position of ~ 200 nm, the Al signal decreases gradually, while the Ti signal increases. Our observation is consistent with previous reported data on the oxidation of $\text{Ti}_x\text{Al}_{1-x}\text{N}$ films. McIntyre *et al.*¹¹ reported that the oxidation of $\text{Ti}_x\text{Al}_{1-x}\text{N}$ films initiated via out-diffusion of Al which leads to the formation of a TiN-rich layer close to the substrate and the AlN-rich one closer to the surface of the

film.

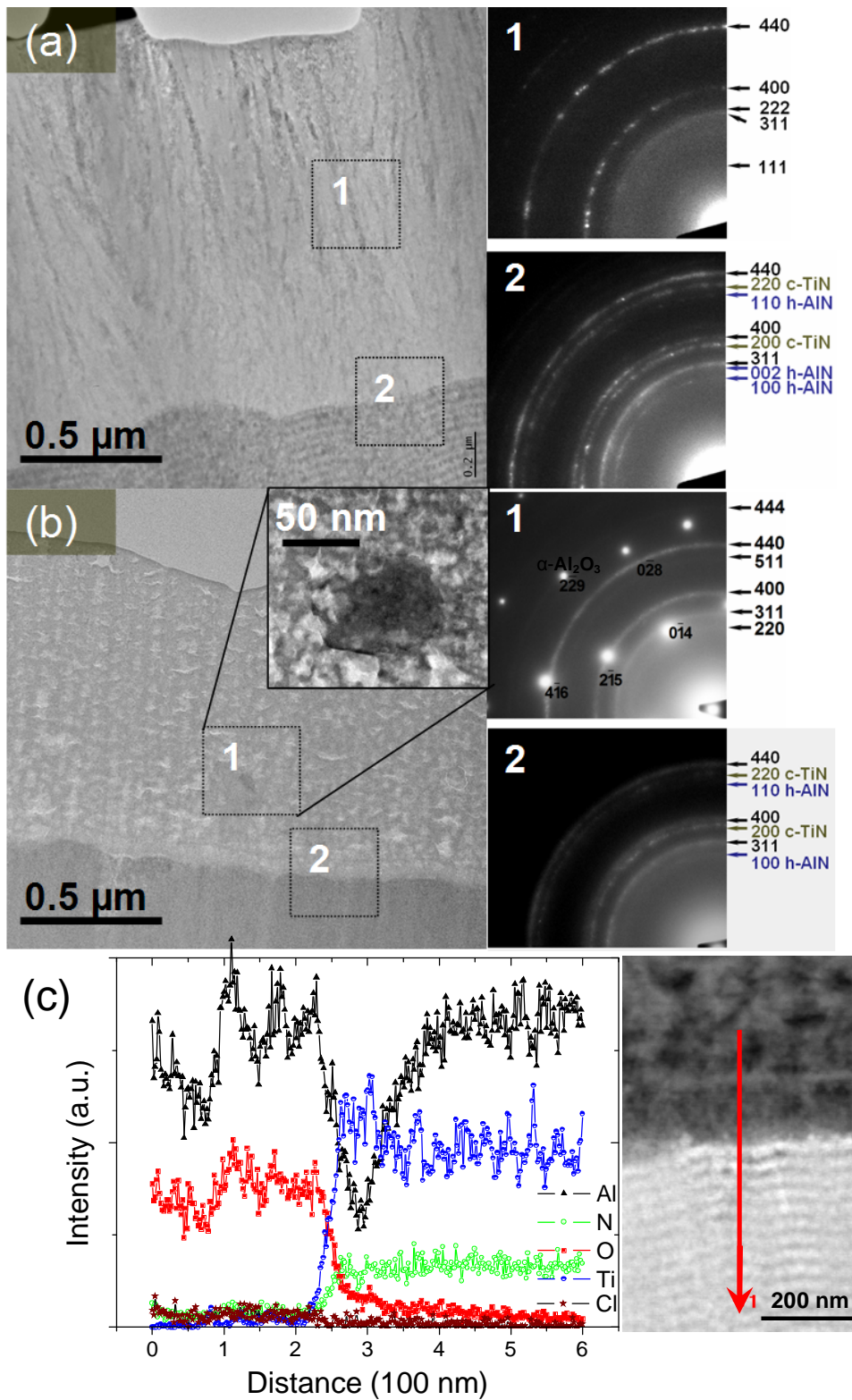


Fig. 5-3 TEM images of 900 °C annealed FCA sample (b) TEM images of 900 °C annealed PECVD samples. The indexed SAED patterns correspond to the remarked regions in the TEM images. The γ - Al_2O_3 diffraction rings are indexed in black. (c) EDX line scan across the γ - $\text{Al}_2\text{O}_3/\text{Ti}_{0.33}\text{Al}_{0.67}\text{N}$ interface of a PECVD film annealed at 900 °C. The red arrow marks the position and direction of the line scan.

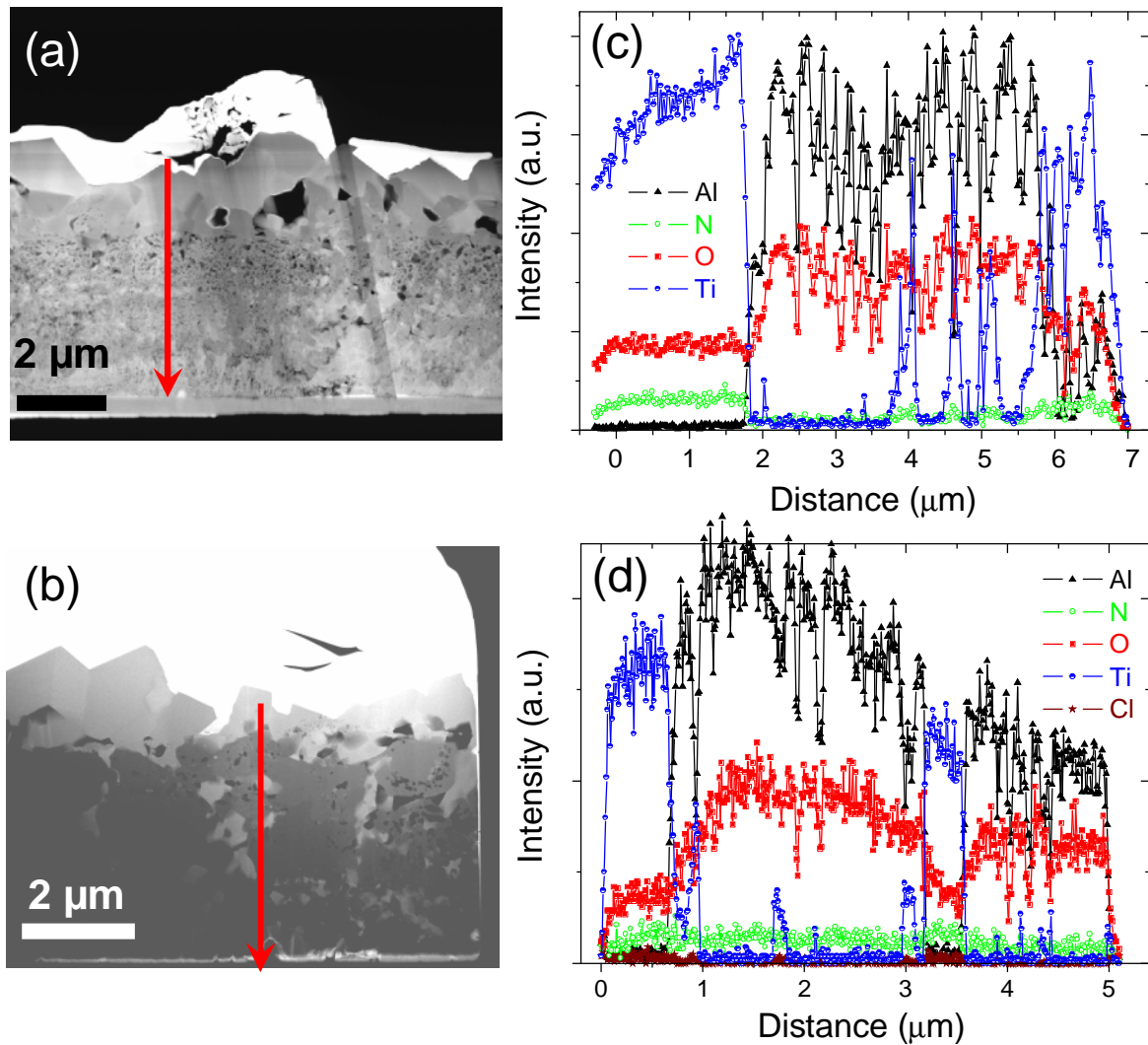


Fig. 5-4 (a) The STEM-HAADF image of FCA sample annealed at 1000 °C. (b) The STEM-HAADF image of PECVD sample annealed at 1000 °C. (c) EDX line scan on the FCA sample. (d) EDX line scan on the PECVD sample. The arrow marked corresponds to the position and direction of the line scan.

A constant Cl signal is also observed throughout the whole Al_2O_3 layer, suggesting Cl incorporation in the PECVD Al_2O_3 film consistent with previous reports¹⁹.

The cross sectional STEM-HAADF image from FCA and PECVD films annealed at 1000 °C are presented in Fig. 5-4a and 4b, respectively. The $\text{Al}_2\text{O}_3/\text{Ti}_{0.33}\text{Al}_{0.67}\text{N}$ interfaces for both samples are no longer visible. The whole coating system exhibits

a porous structure. The STEM-EDX line scans from these films are presented in Fig. 5-4c and 4d, respectively. In accordance with the cross section images no sharp $\text{Al}_2\text{O}_3/\text{Ti}_{0.33}\text{Al}_{0.67}\text{N}$ interfaces can be observed. Furthermore, the presence of Ti is observed along the growth direction of the film and at the surface. The Ti signal is no longer related to the presence of Al and N, but scales with the O population and a small N signal, while the Al signal scales exclusively with the O signal. This is consistent with the presence of TiO_2 and $\alpha\text{-Al}_2\text{O}_3$ as indicated by XRD data in Fig.1(b). It may be speculated that as the temperature is increased also the mobility of oxygen in the $\gamma\text{-Al}_2\text{O}_3$, which contains pores, is increased. This may result in the oxidation of already partly decomposed $\text{Ti}_{0.33}\text{Al}_{0.67}\text{N}$. Upon oxidation TiN transforms into the rutile TiO_2 phase, while AlN transforms into metastable Al_2O_3 phases such as $\gamma\text{-Al}_2\text{O}_3$ ^{12,13}. The AlN (molar volume: 12.4 cm^3) to $1/2\text{ Al}_2\text{O}_3$ (molar volume: 25.5 cm^3) transformation is accompanied by a volume-change per molar reaction of +2.3%, while the corresponding volume change during the TiN (molar volume: 11.4 cm^3) to TiO_2 (molar volume: 18.9 cm^3) transformation is +65.8 %. McIntyre *et al.*¹¹ suggested that the latter leads to the generation of internal stresses in the TiN-rich layer and to crack formation which facilitates the extrusion of TiO_2 towards the film surface. This is in agreement with our results, since TiO_2 is detected in both PECVD and FCA grown films annealed at $1000\text{ }^\circ\text{C}$. The larger porosity of the PECVD $\gamma\text{-Al}_2\text{O}_3$ films as well as their higher tendency to form pores upon heating may facilitate a faster diffusion of O_2 towards the $\text{Ti}_{0.33}\text{Al}_{0.67}\text{N}$ interlayer resulting in a faster oxidation of the TiN, which in turn can explain the more pronounced extrusion of TiO_2 in the PECVD case (Fig. 5-4b) as compared to FCA (Fig. 5-4a).

5.2.2 Thermal stability of the γ - Al_2O_3 film

The DSC and TGA results are presented in Fig. 5-5a and 5b, respectively. The DSC measurements for the powders originating from both the FCA (dotted red line) and PECVD (solid black line) grown films show broad asymmetric exothermic peaks in the temperature range 300 to 1000 °C. In addition, it can be seen that the enthalpic change associated with the PECVD coating is about 3 times larger than the one of FCA coating, which may be associated with the chemical surface desorption of the Cl in PECVD sample. In the same temperature range (300-1000 °C) the TGA analysis reveals a continuous mass loss of 2.7 and 2.9 wt.% for FCA and PECVD powders, respectively. Increasing the temperature to above 1000 °C results in sharp exothermic peaks for both FCA and PECVD powders at the respective positions of 1230 and 1070 °C. To determine the onset of these peaks, a tangential construction¹⁴ is employed as shown in Fig 5-5c. The PECVD powder exhibits an onset temperature of ~1023 °C which is ~50 K lower than that of the FCA one. Moreover, the TGA curve reveals an abrupt mass loss of about 3 wt.% for the PECVD powder between 1000 and 1100 °C.

The BB-XRD patterns of the powders used for the DSC measurements at various temperatures are presented in Fig. 5-6. The diffraction pattern of the powder prepared from the FCA grown film (Fig. 5-6a) at an annealing temperature of 1140 °C exhibits peaks that are attributed to the γ - as well as to the α - Al_2O_3 phase. In the case of the powder prepared from the PECVD film (Fig. 5-6b), only peaks of the γ - Al_2O_3 phase are present at temperatures up to 900 °C. Increase of the temperature to 1000 °C results in the appearance of weak α - Al_2O_3 peaks, while the diffraction pattern that corresponds to a temperature of 1070 °C consists of a mixture of γ - and

5. On The stability of alumina

α - Al_2O_3 peaks. At an annealing temperature of 1200 °C the XRD pattern exhibits exclusively α - Al_2O_3 peaks. These BB-XRD data show a direct γ -to- α - Al_2O_3 transformation for both FCA and PECVD, as opposed to the study by Edlmayr *et al.*¹⁵ which reported the presence of an intermediate δ - Al_2O_3 phase. This could be attributed to differences in the powder particle size which is known to affect the nature (i.e. direct or indirect) of the phase transformation^{16,17}.

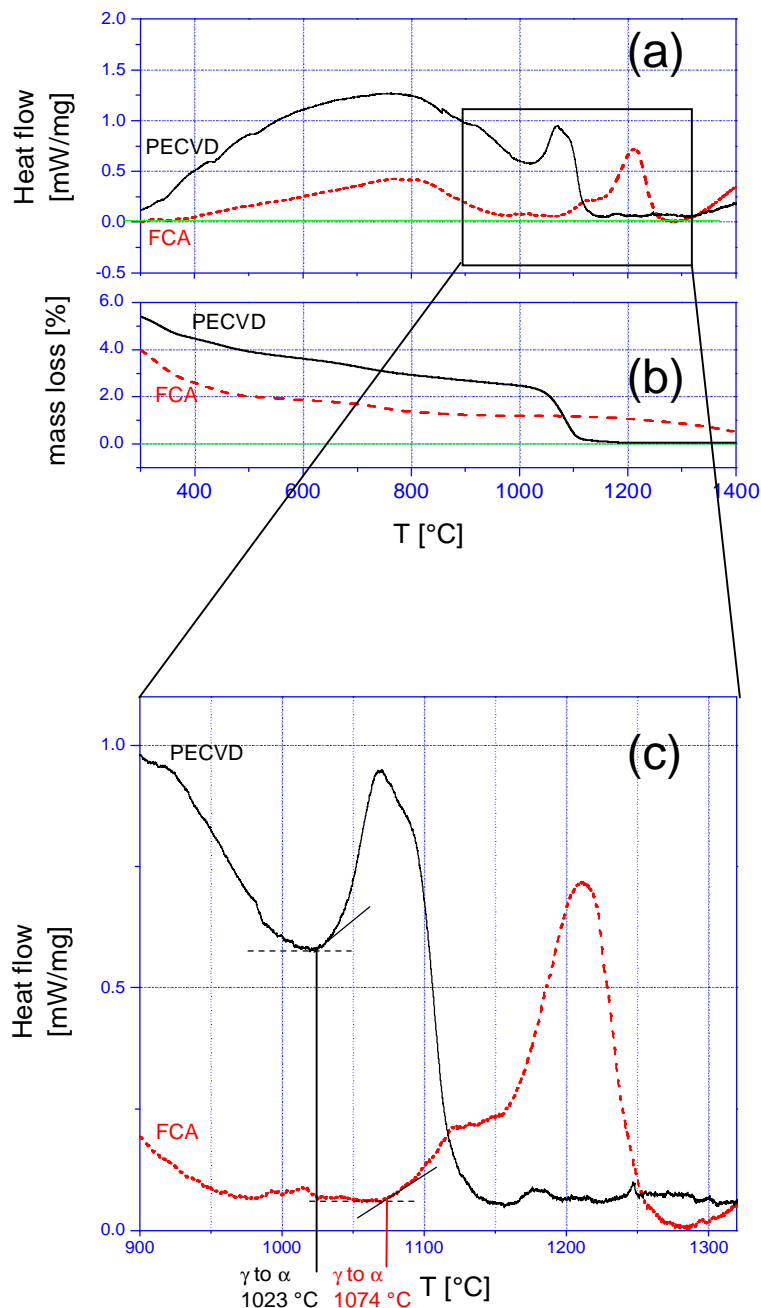


Fig. 5-5 (a) DSC and (b) TGA traces of the different sources of: PECVD films (black solid) and FCA films (red dash) (c) Onset temperature of transformation temperature of different γ alumina by a tangential rule.

5.2.3 Effect of morphology on the γ to α - Al_2O_3 transformation

The thermally induced γ to α - Al_2O_3 transformation proceeds via rearrangement of the O sub-lattice which is facilitated by diffusion of Al and O atoms within the individual grains as well as between the grains¹⁸. The presence of lattice vacancies and voids (pores) can enhance these diffusion processes. Our results (Fig. 5-2) show that the PECVD grown γ - Al_2O_3 films exhibit a larger porosity than the FCA ones. This is consistent with the fact that the γ to α - Al_2O_3 transformation in the PECVD films is faster and occurs at lower temperatures in comparison to the FCA films as demonstrated in Figs. 5-1, 5-3, 5-5, and 5-6. As mentioned in section 2 in the PECVD process AlCl_3 is used as a precursor. It has been shown that the dissociation of AlCl_3 in the PECVD discharge is incomplete which in turn leads to incorporation of Cl in the films¹⁹⁻²¹. Snyders *et al.*¹⁹ have suggested that during growth diffusion incorporated Cl atoms may cause the porosity observed in the PECVD grown films. As the annealing temperature is raised above the growth temperature, diffusion of Cl may further enhance the γ - to α - Al_2O_3 transformation via nucleation and abnormal growth of α - Al_2O_3 in the γ - Al_2O_3 matrix as shown SAED in Fig. 5-3b. This is particularly pronounced at annealing temperatures above 1000 °C as manifested by the abrupt mass loss observed in the TGA curves in Fig. 5-5b. The abrupt mass loss at temperatures higher than 1000 °C is consistent with previously reported Knudsen effusion mass spectrometry measurements¹⁹. Moreover, *ab initio* calculations by Snyders *et al.*¹⁹ suggested that the presence of Cl in Al_2O_3 results in a decrease of the energy difference between γ - and α - Al_2O_3 , as compared to the energy difference in the Cl free configurations. The latter implies that release of Cl from the γ - Al_2O_3 film provides an additional driving force for the γ to α - Al_2O_3 transformation to occur.

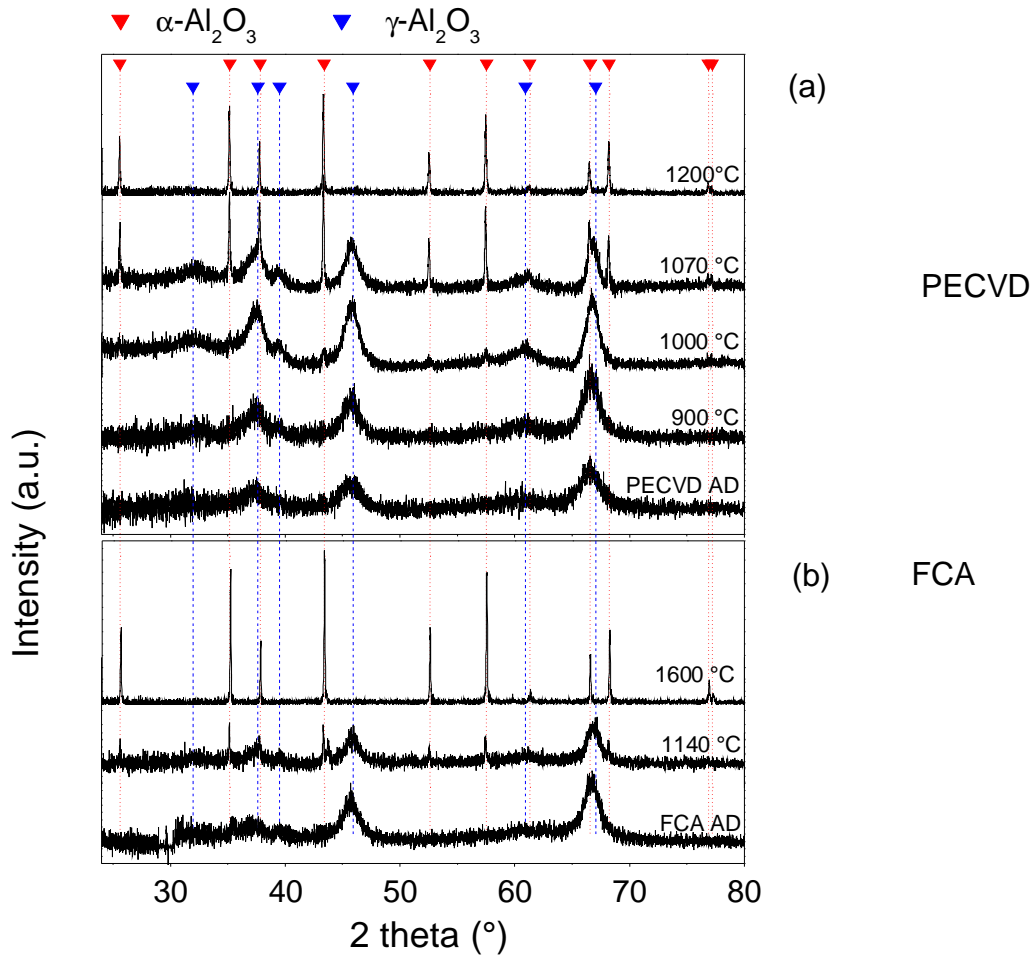


Fig. 5-6 X-ray diffraction patterns of (a) PECVD film and (b) FCA film. Each sample was measured before DSC and after different annealed temperatures

5.3 *Ab initio* study of effects of substitutional additives on the phase stability of γ -alumina

5.3.1 Crystal structure

The crystallographic parameters of spinel and tetragonal hausmannite γ -Al₂O₃ as well as hexagonal α -Al₂O₃ are given in Tab. 5-1. The lattice constants obtained here by VASP are all within 0.8% of the literature values. Fig. 5-7 illustrates the total energies of relaxed tetragonal hausmannite γ -Al₂O₃ with different vacancy configurations as compared to that of cubic spinel. It turns out that the tetragonal hausmannite

structure with octahedral vacancies separated (O+O separated) is energetically favorable with respect to other vacancy distributions. Our finding shows a similar trend as reported for the spinel $\gamma\text{-Al}_2\text{O}_3$ structure^{19,22}. Wolverton and Hass reported that a variety of vacancy-configurations in the spinel $\gamma\text{-Al}_2\text{O}_3$ gave energy differences within a range of 0~9 meV/atom and the most stable spinel structure was with separated octahedral vacancies²². Snyders *et al.* also reported that the agglomeration of one octahedral and one tetrahedral vacancy leads to a rise of total energy in spinel $\gamma\text{-Al}_2\text{O}_3$ ¹⁹. The tetragonal hausmannite structure explored here results in an energy difference of -8 meV/atom with respect to the spinel structure suggesting that the tetragonal hausmannite structure is a suitable description for $\gamma\text{-Al}_2\text{O}_3$. As the tetragonal description by Paglia *et al.*²⁴ was not explored in this work, a direct comparison is not possible. Assuming that the spinel description of Gutiérrez *et al.*²³ allows a meaningful comparison to the one employed here, the tetragonal hausmannite would be the stable configuration. Further work is needed to determine the ground state of $\gamma\text{-Al}_2\text{O}_3$. The energy differences between the various $\gamma\text{-Al}_2\text{O}_3$ structural proposals are rather small and challenging to explore experimentally.

5. On The stability of alumina

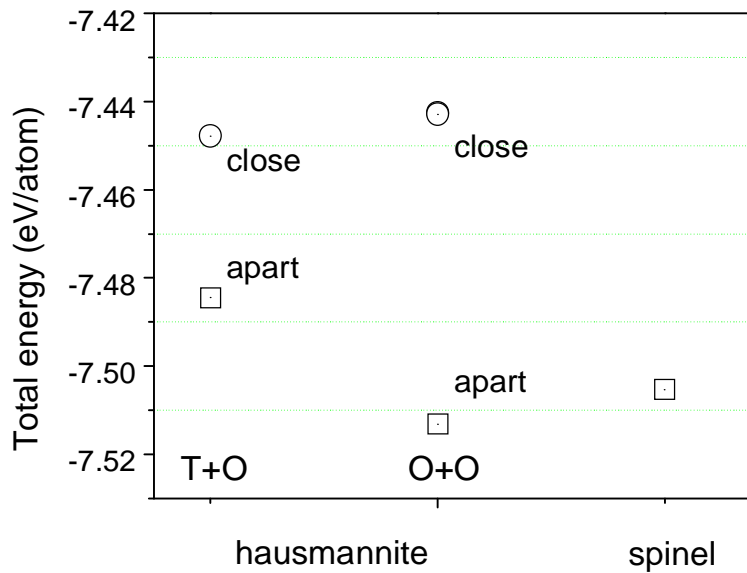


Fig. 5-7 Calculated total energy of different γ - Al_2O_3 configurations. T and O stand for the tetrahedral and octahedral vacancy site, respectively.

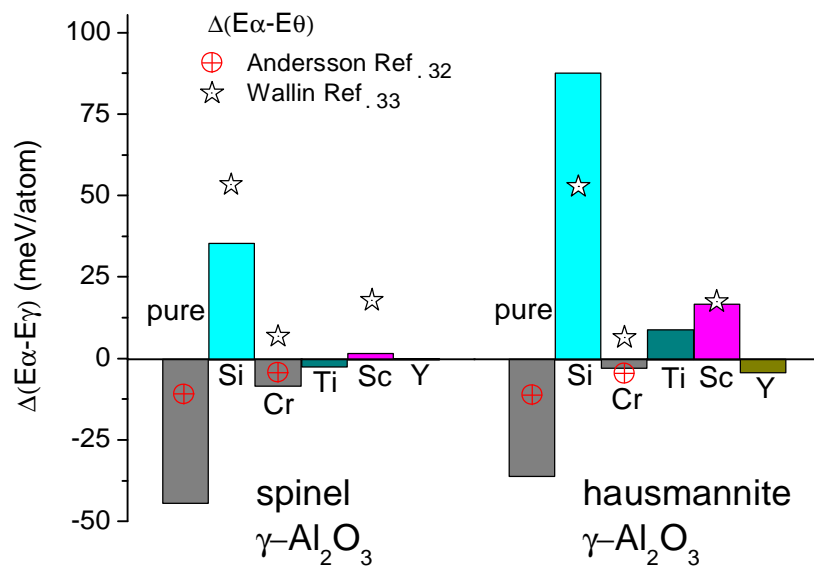


Fig. 5-8 Effect of different additives on the total energy difference, $\Delta(E_\alpha - E_\gamma)$, between the γ - and α - Al_2O_3 . Literature data from Ref.32 and 33 for the total energy difference between θ - and α - Al_2O_3 , $\Delta(E_\alpha - E_\theta)$, are also provided for comparison.

Tab.5-1 Crystallographic data for α - and γ -Al₂O₃

phase	space group	Wyckoff notation	lattice parameters (Å)	
			literature	this work
γ -Al ₂ O ₃ (spinel)	Fd $\bar{3}$ m	Al 8(a)		
		Al 16(d)	a = 7.911(Ref. ²³)	a = 7.9614
		O 32 (e)		
γ -Al ₂ O ₃ (hausmannite)	I4 ₁ /amd	Al 4(a)	a = 5.600	a = 5.632
		Al 8(d)	c/a = 1.403(Ref. ²⁴)	c/a = 1.411
		O 16(h)		
α -Al ₂ O ₃	R $\bar{3}$ c	Al (4c)	a = 4.760	a = 4.796
		O (6e)	c/a = 2.731(Ref. ²⁵)	c/a = 2.747

5.3.2 Influence of additives on the phase stability

Tab. 5-2 shows the total energies in eV/atom for the calculated cells. For the spinel and hausmannite structures, all the other additives except the Si additions reduce the total energies as compared to their unalloyed structures while for the α -Al₂O₃ structure, only Ti and Sc additives reduce the total energies. To investigate the relative stabilities of α - and γ -Al₂O₃, the total energy difference between α - and γ -Al₂O₃, $\Delta(E_{\alpha}-E_{\gamma})$, is plotted in Fig. 5-8. A negative value of $\Delta(E_{\alpha}-E_{\gamma})$ implies a larger stability of the α -phase as compared to the γ -phase. $\Delta(E_{\alpha}-E_{\gamma})$ for the unalloyed phases are in the range of 37 to 46 meV/atom. The obtained calorimetrically values range from 25 to 48 meV/atom^{26,27}. Hence, our data are within the experimentally obtained γ to α transformation enthalpy range. As presented in Fig. 5-8, $\Delta(E_{\alpha}-E_{\gamma})$ is

affected as additives are introduced. For both spinel and tetragonal hausmannite based γ -phases, Si additions significantly stabilize these structures with > 35 meV/atom as compared to the Si alloyed α -Al₂O₃. Experimentally it was observed that Si additives retard the χ to α transformation²⁸. Due to the structural similarity of cubic χ and γ -Al₂O₃¹⁸, our calculations may be relevant in this context. Furthermore, from Fig. 5-8 it is evident that the addition of Cr stabilizes the α -phase. These data are in agreement with the experimental observation, where higher Cr solubility in α -Al₂O₃ is observed than that in γ -Al₂O₃²⁹.

The data on the relative phase stability for other additives, Ti, Sc, and Y, are less conclusive. For instance, Ti stabilizes α -Al₂O₃, if the spinel description is taken into account, while it stabilizes γ -Al₂O₃, if the tetragonal hausmannite is assumed. The magnitude of these $\Delta(E\alpha-E\gamma)$ values are significant to determine phase stability. For instance, the energy difference between hexagonal graphite and cubic diamond was calculated to be 3 meV/atom³⁰ and the stability of fcc/hcp Fe-Mn random alloys is influenced by few meV/atom³¹. The fact that Ti and Y additions result in inconsistent stability prediction for the two γ -structures studied here is at first unexpected. However, it is reasonable to assume that this apparent inconsistency is caused by subtle and significant differences between the alloyed spinel and hausmannite structures. The experimental investigation of γ to α transformation for Ti and Y alloyed γ -Al₂O₃ could be a key experiment in this context. Nevertheless, some general trends can be discussed. Upon increasing the valence electron concentration of the additive from Sc to Cr, the relative stability is shifted from γ to α -Al₂O₃. The increase in size from Sc to Y yields a similar effect, which is not expected due to the lower density of γ -Al₂O₃. The total energy difference between θ - and α -Al₂O₃, $\Delta(E\alpha-E\theta)$ ^{32,33} is plotted in Fig. 5-8. For the undoped system, $\Delta(E\alpha-E\theta)$ is smaller than $\Delta(E\alpha-$

E γ). This is consistent with transformation sequences of $\gamma \rightarrow \theta \rightarrow \alpha$ observed experimentally¹⁸. Furthermore, a similar effect of Si additions on the stability of the γ -phases studied here is observed as compared to the previously studied θ -phases^{32,33}. The energy difference between Cr alloyed α -Al₂O₃ and γ -Al₂O₃ is < -10 meV/atom, which is comparable to the value reported in Ref. 28. Those data are, however, inconsistent with Ref. 29, where Cr additions are reported to stabilize the θ -phase.

Tab.5-2 Total energies (eV/atom) of different cell structures for α - and γ -Al₂O₃

	α -Al ₂ O ₃	spinel	hausmannite
pure	-7.5493	-7.5050	-7.5132
Si	-7.4103	-7.4456	-7.4978
Cr	-7.5236	-7.5152	-7.5208
Ti	-7.5559	-7.5535	-7.5647
Sc	-7.5752	-7.5767	-7.5919
Y	-7.5488	-7.5487	-7.5446

5.3.3 Influence of additives on the electronic structure

Since the most striking difference in the relative phase stability is observed for Si additions, the electronic structure of this configuration is further studied and is compared to the Cr alloyed α -Al₂O₃ configuration. The electron density distributions for α -Al₂O₃ and γ -Al₂O₃ crystals, i.e. both spinel and hausmannite, are shown in Fig. 5-9 and Fig. 5-10. In pure α - and γ -Al₂O₃, a high electron density is observed around the O nuclei, while a low electron density is located around the Al nuclei (Fig. 5-9a and Fig. 5-10a). This is expected and consistent with ionic bonding. There is also some electron density shared between cations and anions, suggesting covalent contributions to the overall bond character. Adding Si and Cr to α - and γ -Al₂O₃, differences in the electronic structure for these two polymorphs are observed.

However, the general bonding nature of Al_2O_3 does not change. In both spinel and hausmannite $\gamma\text{-Al}_2\text{O}_3$ with Si additions, more charge is transferred from Si to the surrounding O, indicating an enhanced ionic character, while in Si alloyed $\alpha\text{-Al}_2\text{O}_3$ less charge is transferred from Si to O. Strong Si-O bonding can therefore be indicative of increased relative phase stability of $\gamma\text{-Al}_2\text{O}_3$ with Si additions.

In the case of Cr substitution, the high electron density around the Cr atom probably originates from the presence of 3d electrons. Hence, it is difficult to discuss the charge transfer from Cr to the surrounding O. Furthermore, a strongly asymmetric charge distribution can be observed in $\gamma\text{-Al}_2\text{O}_3$ with Cr additions, which could contribute to the lower stability in Cr alloyed $\gamma\text{-Al}_2\text{O}_3$.

Since the bond strength of ionic crystals is inversely proportional to the bond length, the bond lengths of the cation to the nearest and the next nearest oxygen anion is presented in Tab. 5-3. The bond length between an additive atom and oxygen (M-O) is compared to the corresponding length of the Al-O bond in an unalloyed configuration. Si in the tetragonal hausmannite $\gamma\text{-Al}_2\text{O}_3$ results in a decrease of the nearest and the next nearest bond lengths on the order of ~2% and Si in the spinel $\gamma\text{-Al}_2\text{O}_3$ shortens the nearest bond distance by ~4%. In contrast, Si increases the nearest and the next nearest bond lengths in the α -structure by 1.5 and 4.5%, respectively. Furthermore, the symmetry of the nearest bonds remains unchanged in the spinel $\gamma\text{-Al}_2\text{O}_3$ with Si additions. These results suggest that Si exhibits stronger bonding with the adjacent oxygen in the γ -structure than that in the α -structure. This is consistent with the electron density distribution data discussed above. In the case of Cr additions, the Cr-O bond lengths in all structures increase which is possibly associated with the large radius of the Cr ion. The length increase in the spinel structure is approx. by a factor two larger than in the α -structure. Also, for the

tetragonal hausmannite $\gamma\text{-Al}_2\text{O}_3$, Cr increases the bond length more than in the α -structure. Hence, Cr is expected to stabilize the α -structure instead of the γ -structure.

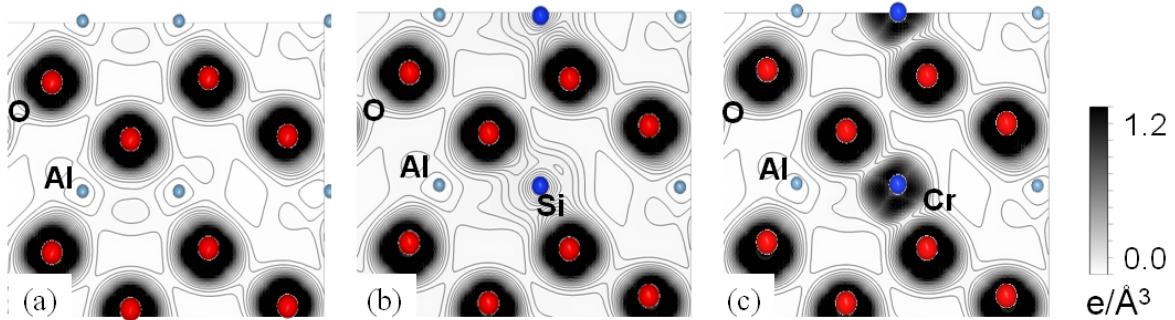


Fig. 5-9 Electron density distributions for (a) pure, (b) Si-containing and (c) Cr-containing $\alpha\text{-Al}_2\text{O}_3$ in the (01-10) planes.

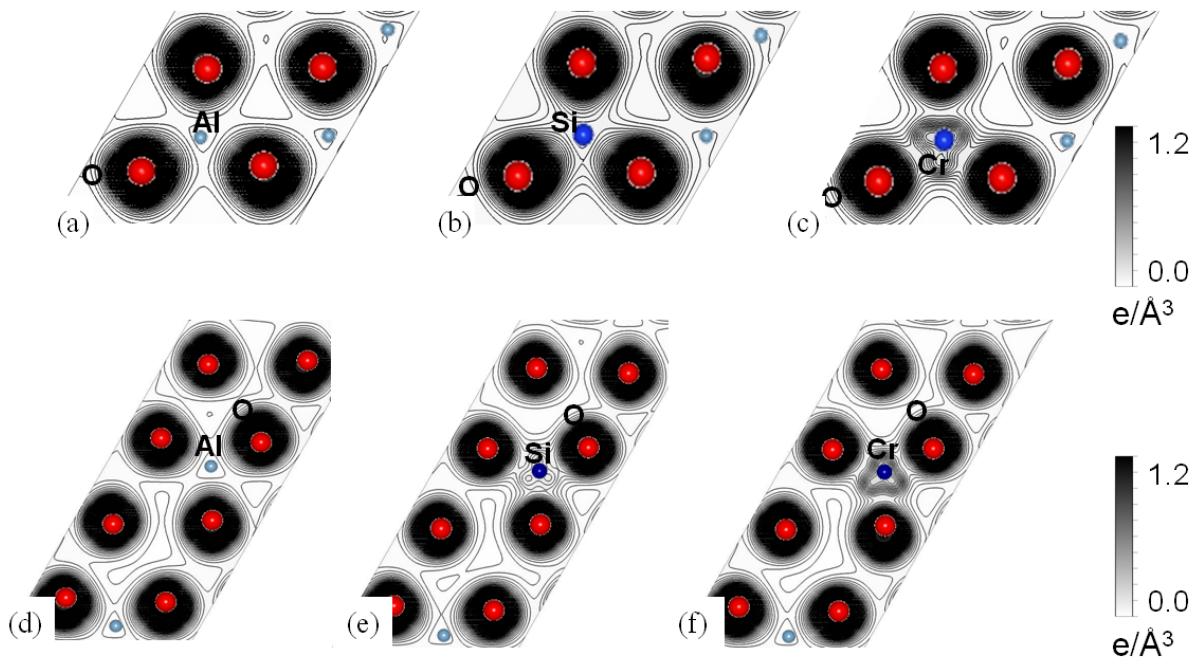


Fig. 5-10 Electron density distributions for (a) pure, (b) Si-containing (c) Cr-containing spinel $\gamma\text{-Al}_2\text{O}_3$ in the (100) planes, and (d) pure, (e) Si-containing (f) Cr-containing hausmannite $\gamma\text{-Al}_2\text{O}_3$ in the (100) planes.

Tab.5-3 Comparison of Al-O and M-O bond lengths in Al₂O₃ (M refers to doping element). The M-O bond length is compared to the corresponding Al-O bond.

spinel	bond length	change (%)	hausmannite	bond length	change (%)	alpha	bond length	change (%)
pure	Al-O		pure	Al-O		pure	Al-O	
	1.76			1.76			1.87	
	1.76			1.77			1.98	
	1.83			1.84				
Si	Si-O		Si	Si-O		Si	Si-O	
	1.69	-4.3		1.72	-2.4		1.90	1.5
	1.69	-4.3		1.74	-1.7		2.07	4.5
	1.86	1.4		1.83	-0.6			
Cr	Cr-O		Cr	Cr-O		Cr	Cr-O	
	1.91	8.5		1.84	4.6		1.94	3.7
	1.81	2.8		1.85	4.5		2.07	1.8
	1.99	8.8		1.90	3.3			

5.3.4 Influence of additives on the elastic properties

The calculated bulk moduli of all γ -configurations are presented in Fig.5-11. For both types of γ -structures, similar values and the same trends of bulk moduli are observed. Pure γ -Al₂O₃ exhibits a bulk modulus of approx. 213 GPa, which is consistent with those reported in literature^{23,34}. Apart from the introduction of Y which results in a ~5% decrease in the bulk modulus value (compared to unalloyed γ -Al₂O₃), the addition of other elements shows no significant influence on the stiffness. This is consistent with the electronic structure data presented above. From the application point of view, adding Si into γ -Al₂O₃ may result in a promising material for the application at elevated temperatures such as high temperature forming and cutting operations, because of the Si induced enhanced stability while maintaining the high stiffness.

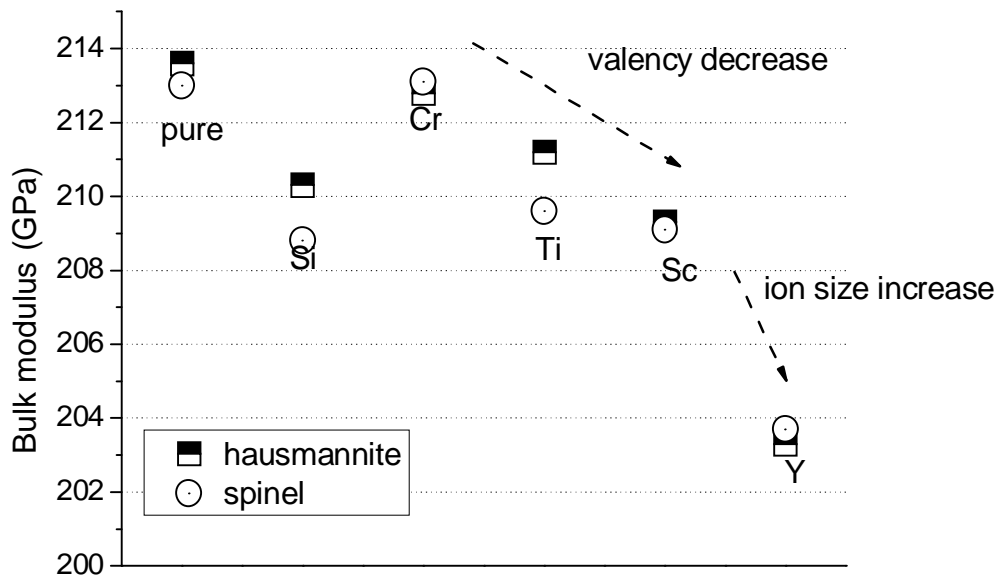


Fig. 5-11 Bulk modulus of γ - Al_2O_3 with or without additional elements.

5.4 Conclusions

Effects of composition and microstructure on the stability of γ - Al_2O_3 films grown by FCA and PECVD on TiAlN coated WC-Co cutting inserts have been investigated. The as deposited PECVD films are porous with Cl incorporation, while the FCA films exhibit a dense microstructure. After 1 hour annealing in air, the presence of a large α - Al_2O_3 grain in a PECVD sample at 900 °C is observed, while no phase change in FCA γ - Al_2O_3 was detected. SAED patterns recorded at the Al_2O_3 /TiAlN interface for both FCA and PECVD films exhibit the presence of hexagonal-AlN phases indicating the decomposition of the $\text{Ti}_{0.33}\text{Al}_{0.67}\text{N}$ interlayer. At 1000 °C, no Al_2O_3 / $\text{Ti}_{0.33}\text{Al}_{0.67}\text{N}$ interfaces can be identified for both samples which could be a consequence of the oxidation of the $\text{Ti}_{0.33}\text{Al}_{0.67}\text{N}$ interlayer and the extrusion of TiO_2 towards the film surface due to large volume expansion of TiO_2 . It appears that the interlayer oxidation is enabled by both inward diffusion of O via γ - Al_2O_3 at elevated temperatures and

decomposition of $\text{Ti}_{0.33}\text{Al}_{0.67}\text{N}$ into TiN and AlN domains. Concerning the phase stability of $\gamma\text{-Al}_2\text{O}_3$, DSC and X-ray diffraction analysis of both films also imply an earlier and fast $\gamma \rightarrow \alpha\text{-Al}_2\text{O}_3$ transformation of PECVD films with onset of 1023 °C, while onset of FCA films is 1074 °C. TGA data show a mobilization of Cl at ~1000 °C indicating an enhancement of out-diffusion process of Cl which consequently enhances the transformation. The present study suggests that not only the morphology and composition of the film but also the stability of the substrate and/or interlayer determines the high temperature performance of $\gamma\text{-Al}_2\text{O}_3$ coatings. Therefore the choice of a proper substrate material is equally important as growing dense and stoichiometric thin films.

Using *ab initio* calculations, we have evaluated two structural descriptions of $\gamma\text{-Al}_2\text{O}_3$, spinel and tetragonal hausmannite, and explored the relative stability of $\gamma\text{-Al}_2\text{O}_3$ with respect to $\alpha\text{-Al}_2\text{O}_3$ with 2.5 at.% of Si, Cr, Ti, Sc, and Y additives to identify alloying element induced electronic structure changes that impede the γ to α transition. The total energy calculations indicate that Si stabilizes $\gamma\text{-Al}_2\text{O}_3$, while Cr stabilizes $\alpha\text{-Al}_2\text{O}_3$. As Si is added, a bond length increase in $\alpha\text{-Al}_2\text{O}_3$ is observed, while strong and short Si-O bonds are formed in $\gamma\text{-Al}_2\text{O}_3$, consequently stabilizing this phase. On the other hand, Cr additions induce a smaller bond length increase in $\alpha\text{-Al}_2\text{O}_3$ than in $\gamma\text{-Al}_2\text{O}_3$, therefore stabilizing the α -phase. The bulk moduli of $\gamma\text{-Al}_2\text{O}_3$ with these additives show no significant changes. The here discussed phase stability and elastic property data underline the application potential of Si alloyed $\gamma\text{-Al}_2\text{O}_3$ for applications at elevated temperatures. Furthermore, it is evident that the tetragonal hausmannite structure is a suitable description for $\gamma\text{-Al}_2\text{O}_3$.

- 1 in *International Centre for Diffraction Data JCPDS Powder Diffraction File No*
10-425. (1999).
- 2 in *International Centre for Diffraction Data JCPDS Powder Diffraction File No*
21-1276. (1999).
- 3 in *International Centre for Diffraction Data JCPDS Powder Diffraction File No*
25-1495. (1999).
- 4 in *International Centre for Diffraction Data JCPDS Powder Diffraction File No*
38-1420. (1999).
- 5 in *International Centre for Diffraction Data JCPDS Powder Diffraction File No*
10-173. (1999).
- 6 K. Bobzin, N. Bagcivan, P. Immich, M. Ewering, *Adv. Eng. Mater.* **11**, 590-594
(2009).
- 7 R. Rachbauer, E. Stergar, S. Massl, M. Moser, P. H. Mayrhofer, *Scr. Mater.* **61**,
725-728 (2009).
- 8 P. H. Mayrhofer, L. Hultman, J. M. Schneider, P. Staron, H. Clemens, *Int. J.*
Mater. Res. **98**, 1054-1059 (2007).
- 9 P. H. Mayrhofer, F. D. Fischer, H. J. Bohm, C. Mitterer, J. M. Schneider, *Acta*
Mater. **55**, 1441-1446 (2007).
- 10 P. H. Mayrhofer, A. Horling, L. Karlsson, J. Sjolen, T. Larsson, C. Mitterer, L.
Hultman, *Appl. Phys. Lett.* **83**, 2049-2051 (2003).
- 11 D. McIntyre, J. E. Greene, G. Hakansson, J. E. Sundgren, W. D. Munz, *J. Appl.*
Phys. **67**, 1542-1553 (1990).
- 12 Y. Masashi, S. Yukichi, I. Hiroki, O. Hitoshi, S. Noriyoshi, *Journal of the*
Society of Materials Science, Japan **55**, 785-789 (2006).
- 13 R. F. Yue, Y. Wang, Y. X. Wang, C. H. Chen, *Appl. Surf. Sci.* **148**, 73-78
(1999).
- 14 N. C. Parasnis, K. Ramani, *J. Therm. Anal. Calorim.* **55**, 709-719 (1999).
- 15 V. Edlmayr, M. Moser, C. Walter, C. Mitterer, *Surf. Coat. Technol.* **204**, 1576-
1581 (2010).
- 16 R. S. Zhou, R. L. Snyder, *Acta Crystallogr., Sect. B: Struct. Sci.* **47**, 617-630
(1991).
- 17 J. M. McHale, A. Navrotsky, A. J. Perrotta, *J. Phys. Chem. B* **101**, 603-613
(1997).
- 18 I. Levin, D. Brandon, *J. Am. Ceram. Soc.* **81**, 1995-2012 (1998).

- 19 R. Snyders, K. Jiang, D. Music, S. Konstantinidis, T. Markus, A. Reinholdt, J. Mayer, J. M. Schneider, *Surf. Coat. Technol.* **204**, 215-221 (2009).
- 20 K. Jiang, K. Sarakinos, S. Konstantinidis, J. M. Schneider, *J. Phys. D: Appl. Phys.* **43**, 325202 (2010).
- 21 S. Konstantinidis, K. Jiang, J. M. Schneider, unpublished (2010).
- 22 C. Wolverton, K. C. Hass, *Phys. Rev. B* **63**, 024102 (2001).
- 23 G. Gutiérrez, A. Taga, B. Johansson, *Phys. Rev. B* **65**, 012101 (2002).
- 24 G. Paglia, A. L. Rohl, C. E. Buckley, J. D. Gale, *Phys. Rev. B* **71**, 224115 (2005).
- 25 Villars, L. D. Calvert, *Pearson's Handbook of Crystallographic Data for Intermetallic Phases*, Vol. 2 (American Society for Metals, 1997).
- 26 A. Navrotsky, B. A. Wechsler, K. Geisinger, F. Seifert, *J. Am. Ceram. Soc.* **69**, 418-422 (1986).
- 27 J. M. McHale, A. Auroux, A. J. Perrotta, A. Navrotsky, *Science* **277**, 788-791 (1997).
- 28 O. Mekasuwandumrong, P. Tantichuwet, C. Chaisuk, P. Praserttham, *Mater. Chem. Phys.* **107**, 208-214 (2008).
- 29 D. D. Ragan, T. Mates, D. R. Clarke, *J. Am. Ceram. Soc.* **86**, 541-545 (2003).
- 30 J. Furthmüller, J. Hafner, G. Kresse, *Phys. Rev. B* **50**, 15606-15622 (1994).
- 31 T. Gebhardt, et al., *J. Phys.: Condens. Matter* **22**, 295402.
- 32 J. M. Andersson, E. Wallin, V. Chirita, E. P. Munger, U. Helmersson, *Phys. Rev. B* **71**, 014101 (2005).
- 33 E. Wallin, J. M. Andersson, V. Chirita, U. Helmersson, *J. Phys.: Condens. Matter* **16**, 8971-8980 (2004).
- 34 A. Schütze, D. T. Quinto, *Surf. Coat. Technol.* **162**, 174-182 (2003).

6 UP-SCALING OF A LOW TEMPERATURE PECVD PROCESS

Based on the previous laboratory studies, the thin film synthesis / properties relationship is investigated in an industrial-scale pulsed PECVD reactor. The low temperature process, which was developed in the laboratory, was scaled up. The α/γ - Al_2O_3 coated moulds were utilized in steel thixocasting at temperatures of ~ 1400 °C.

6.1 Introduction

Although substantial progress in Al_2O_3 processing has been achieved on the laboratory scale as discussed in chapter 2, upscaling to an industrial reactor enabling the deposition onto large and/or complex three dimensional tools has not yet been accomplished. This may be due to a variety of industrial reactor inherent factors including temperature and flux distributions within the reactor volume, etc. Thus, low temperature α - Al_2O_3 deposition in an industrial reactor remains a challenging task. The objective of this work is to develop a processing strategy to deposit protective Al_2O_3 coatings onto large Semi-Solid Processing (SSP) dies at a substrate temperature of < 600 °C. Special attention has been paid to the optimization of the coating homogeneity in a 384 liter PECVD reactor. Based on a systematic study of the process-conditions/coating-constitutions relationship, a phase formation diagram for alumina coatings as a function of pulse length and cathode voltage was compiled.

6.2 Industrial PECVD deposition system

The bipolar pulsed PECVD system is shown in Fig. 6-1. The cylindrical vacuum chamber has a volume of 384 liter with 700 mm in diameter and 1000 mm in height. The chamber seal is equipped with auxiliary heating elements and a fan cooling system to control the wall temperature. To monitor the temperature variation during the processes, four Ni-Cr-Ni thermocouples are placed at different positions in the chamber (see Fig. 6-1) including the height corresponding to the substrate location. Two stainless steel electrodes (400 mm in diameter), separated by tubular ceramic supports (35 mm), are mounted in the centre of the chamber. The bottom electrode is the cathode and the upper electrode as well as the chamber is the anode. Hence the plasma is confined to the region between the two electrodes. The thixoforming tools are placed on the lower cathode. Apart from O₂, which is introduced into the chamber from the top, all other gases are mixed and introduced into the chamber through the gas shower located between the two electrodes. Using two separated gas inlets, reactions inside or in the vicinity of the gas shower can be avoided, thus inhibiting blocking of the gas inlet.

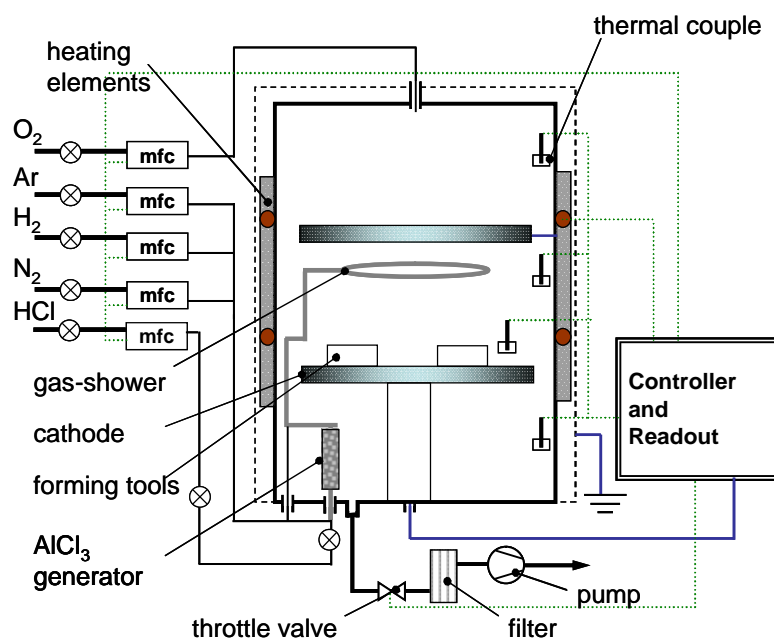


Fig. 6-1 Cross-sectional schematic view of the PECVD deposition chamber.

6.3 Results and discussions

6.3.1 Coating homogeneity

To achieve a homogenous coating thickness distribution over the entire forming tool a suitable gas injection system has been developed. It is well known that in PECVD deposition systems, particularly in such large chambers, the distribution of all gaseous species crucially influences the coating uniformity. Here, three gas-shower designs were investigated. A gas shower is a metal tube where gas is transported and distributed through multiple outlets into the reactor volume. The corresponding flow density ρ , calculated from the flow through each outlet per outlet size, is listed in Table 2. Samples are placed at four different circular locations as well as at the centre of the substrate holder as indicated in Fig. 6-2a. The deposition rate profile over the entire holder surface area, based on thickness measurements, is given in Fig. 6-2b and 2c. The results reveal that $\rho = 1.14 \times 10^{-2}$ sccm/mm², i.e. outlet sizes of 0.8 mm and an outlet number of 50, yields the optimal gas flow uniformity. Under these conditions the deviation in the deposition rate measured across the substrate holder surface is within $\pm 7\%$. Large thickness deviation of 35% is observed at $\rho = 2.3 \times 10^{-3}$ sccm/mm², while no coating was obtained at ρ values as low as 4×10^{-3} sccm/mm². Hence, non-uniform gas distribution within the reactor volume results in thickness variations across the cathode surface. Higher deposition rates are observed close to the entrance of the gas shower, while lower rates were obtained at a greater distance to the gas shower. This observation indicates that more precursor gas reaches the substrate surface close to gas inlet side. The flow rate distribution in multi-outlet straight pipes has been studied by Mokhtari *et al.*¹ Using computational fluid dynamics (CFD), the authors reported that the flow homogeneity is affected by the inlet flow rate and the aspect ratio between the main pipe and the outlet diameter.

An inhomogeneous flow distribution, where most of the gas flows out of the first set of outlets, is obtained at very low inlet flows of 0.34 l/min, i.e. a low Reynolds number of 100, and an aspect ratio of 11. Taking into account the inlet flow of 0.58 l/min employed here, corresponding to a Reynolds number of 125, the inhomogeneities observed herein (see Fig. 6-2a and 2b) are attributed to the comparatively large outlet sizes and resulting low diameter aspect ratio in the experimental setup, being consistent with these simulation results. At even lower flow density, the gas only flows out of the first few outlets and is dispersed over the chamber, thus leading to an increase of precursor population in the vicinity of first few outlets. Considering the process employed here, where the pressure-distance product is large, homogeneous gas reactions between precursor AlCl₃ and O₂, which is relatively light and distributed all over the chamber volume, are likely to happen. As reaction products Al₂O₃-clusters or particles aggregate in the gas phase and subsequently accumulate on the chamber wall or exhaust outlet. Consequently, this results in a very small amount of precursor gas reaching the substrate surface and hence in a small deposition rate. Therefore, the decrease of the outlet sizes of the gas shower allows for a homogeneous gas distribution and an increase in the fraction of heterogeneous reactions on the substrate surface. Thus, an improvement of the coating homogeneity and an increase of the deposition rate are expected.

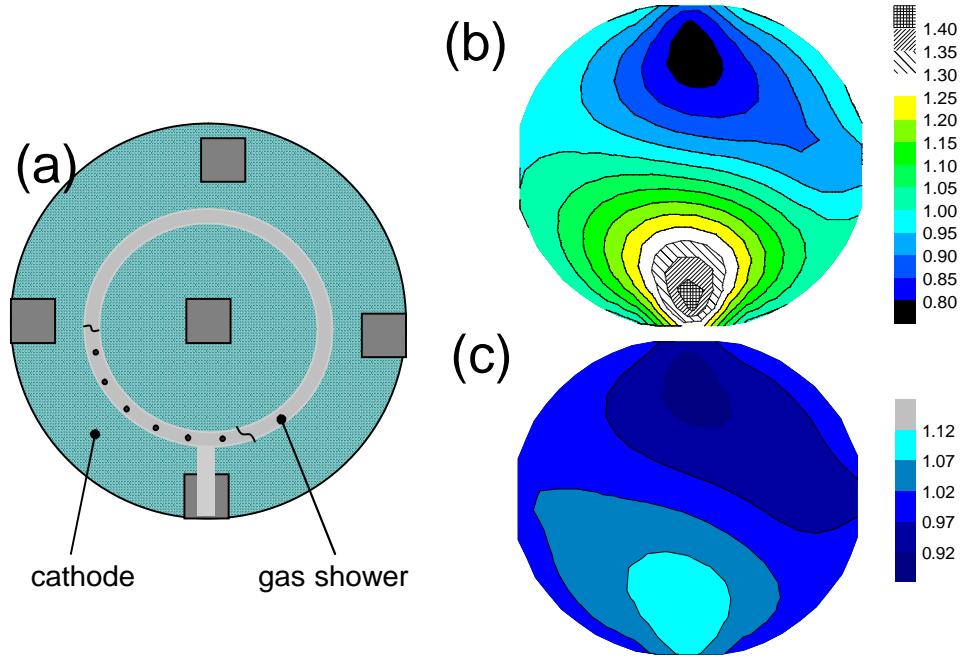


Fig. 6-2 (a) Deposition rate measurements at different locations of the holder edge and centre of the substrate holder. (b) deposition rate distribution across the substrate holder at flow density $\rho = 1.1 \times 10^{-2}$ sccm/mm² (c) deposition rate distribution across the substrate holder at $\rho = 1.1 \times 10^{-3}$ sccm/mm².

Table.2 The effects of flow density on the deposition rate over the substrate holder at 175 Pa/ 590 °C).The gas shower inlet diameter is 10 mm for all parameter sets.

hole diameter	number	flow density (sccm/mm ²)	remarks
2.5	50	4.0×10^{-3}	very low deposition rate, high amount of white power on chamber wall and gas shower
2.5	30	2.3×10^{-3}	$\pm 36\%$, highest rate at locations close to gas let point
0.8	50	1.1×10^{-2}	$\pm 7\%$, smallest variation of deposition rate over substrate holder

On the basis of these results, forming tools with complex geometry have been coated by PECVD applying a flow density of 1.1×10^{-2} sccm/mm². Coating thickness homogeneity was estimated by sampling of cross sections at different locations on the tool surface using SEM as shown in Fig. 6-3. An average coating thickness of

3.5 ± 0.3 μm was determined. At position 1 and 2, which correspond to locations at the bottom of the form channel, the substrate surface is comparably rough with a peak to valley distance of up to 10 μm due to limitations of the machining process. However, the surface is homogeneously covered with a ~3.5 μm thick coating. The transition zone indicates good attachment of the coating to the substrate. Besides the thickness, the constitution homogeneity was also investigated by micro-diffraction. Fig. 6-4 depicts the results of this GADDS analysis at different positions on the tool. No significant variation in constitution was observed for the three different positions investigated, indicating a homogenous constitution over the whole tool surface.

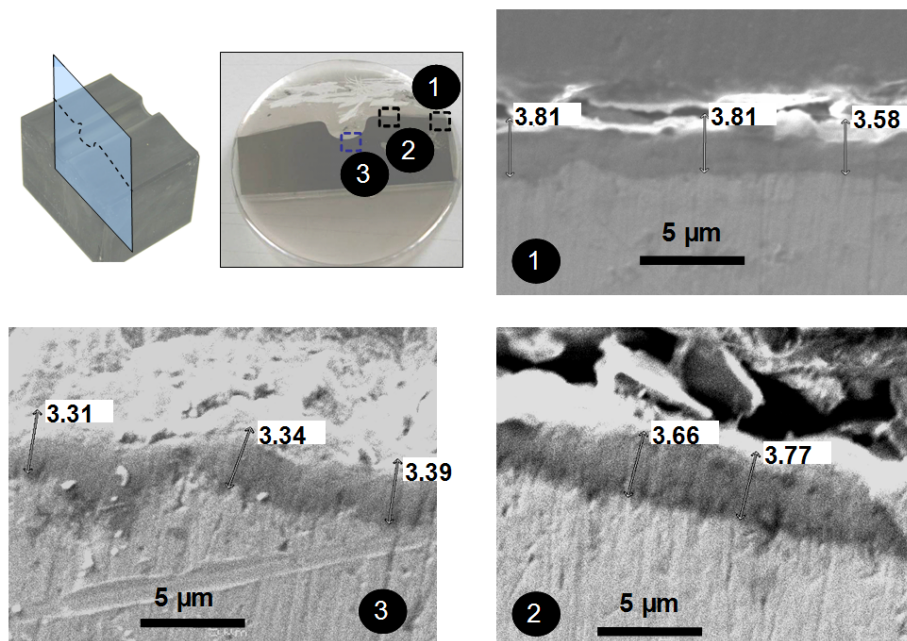


Fig. 6-3 Different positions of cross-sectional SEM images of α/γ-Al₂O₃ mixture coating grown on thixoforming tool segment. The tool segment was cut and imbedded in a plastic form shown at upper-left corner. The mixture coating was grown at pulse voltage of -750V, pulse length of 250 μs temperature of 590 °C.

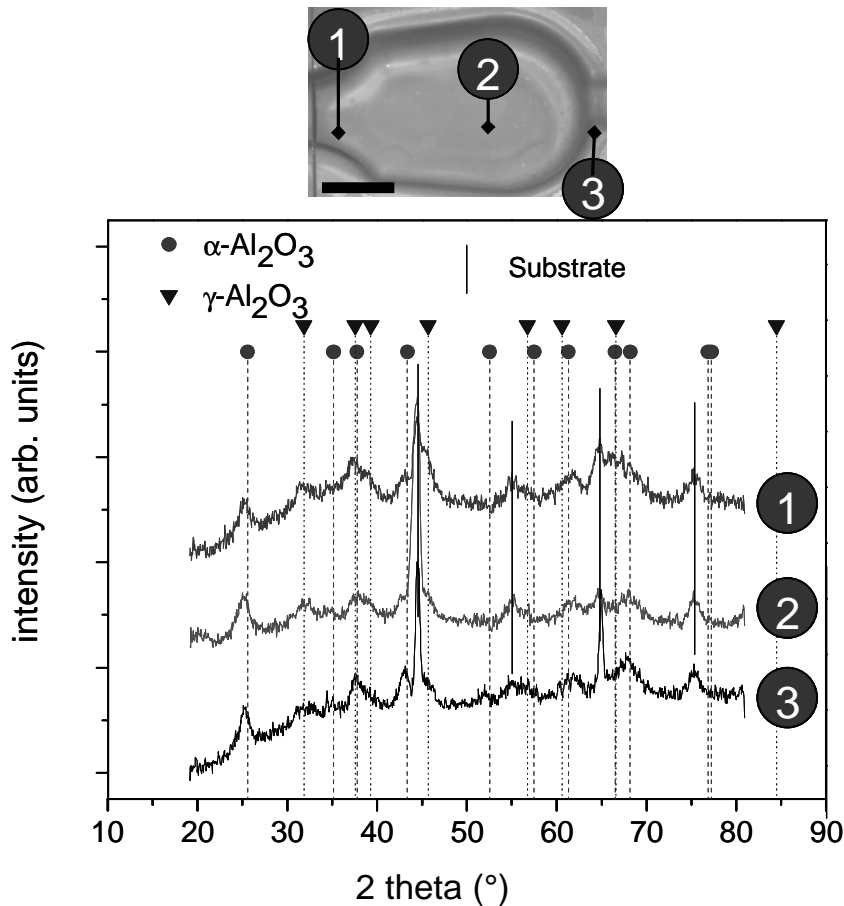


Fig. 6-4 X-ray micro-diffraction (GADDS) at different positions of the alumina coated thixoforming tool segments. The coating was grown at pulse voltage of -750V, pulse length of 250 μ s temperature of 590 $^{\circ}$ C.

6.3.2 Phase constitution

The major difference between the laboratory-scale and this industrial PECVD system lies in the specific generator employed here, limiting the adjustable frequency to <10 Hz and the pulse time and the off time to > 50 μ s. A set of experiments was carried out to identify a process window yielding high plasma density and hence sufficient ion bombardment. The phase formation data was compiled into one diagram correlating (negative) pulse length (L), cathode voltage (V) and the phase constitution (Fig. 6-5). In this diagram, three regions are identified according to the constitution of the coatings, namely region (i) consisting of amorphous Al₂O₃, (ii) consisting of pure γ -Al₂O₃, and region (iii) consisting of an α/γ -Al₂O₃ phase mixture. It is clearly observed

that the α -Al₂O₃ formation is enabled by increasing the energy or duration of particle bombardment on the growing coatings. This result is consistent with previous studies,^{2,3} where it was demonstrated that increasing the plasma density stimulates efficient precursor dissociation.

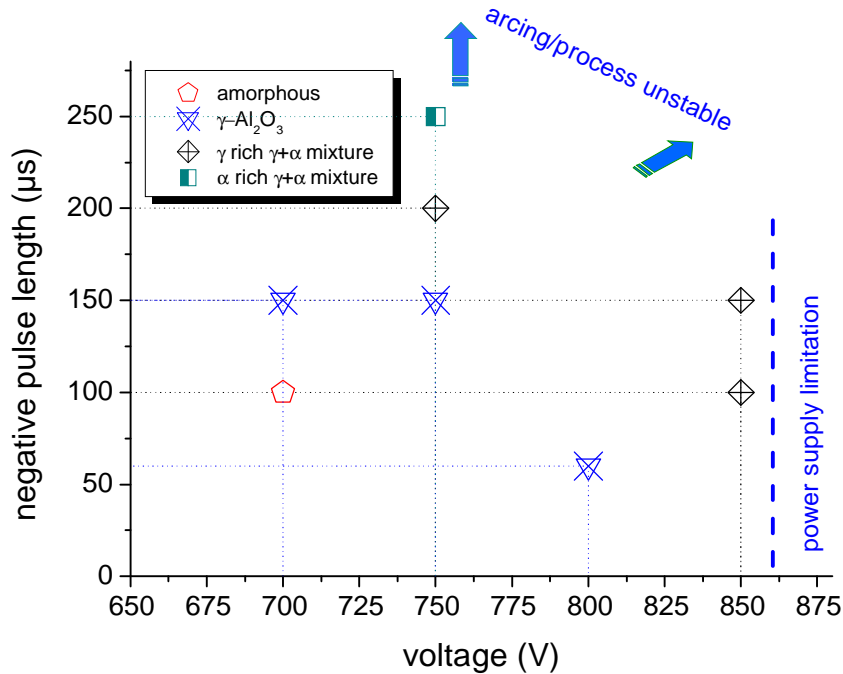


Fig. 6-5 Phase-formation diagram of alumina films deposited by PECVD as functions of cathode voltage and negative pulse length. The substrate temperature was controlled at 590 °C.

As already shown in section 4.3, it was found that an increase of the pulse length led to a decrease of the Cl content and a densification of the coatings. The prolonged interaction time of the plasma with the precursor molecules and the growing coating surface enhances the efficiency of the AlCl₃ molecules dissociation and Cl surface desorption by the energetic bombardment of the growing coating. However, in the present study, pulse length and cathode potential could not be increased over 250 μ s and 850 V due to power supply limitations. Arcing and unstable processing were the consequence of increasing the pulse length and cathode potential further. The optimum process parameters yielding a high α -Al₂O₃ content are a pulse length of 250 μ s and a cathode voltage of -750 V.

6.3.3 Chemical composition and coating morphology

EDX-analysis of the chemical composition of all deposited coatings shows no dependence on the pulse length and cathode voltage. The Al/O ratio was measured to be 0.59 ± 0.02 for all. Cl-incorporation originating from incomplete decomposition of the AlCl₃ molecule may cause coating porosity^{3,4}. In this study, the AlCl₃+O₂-precursor content of the gas mixture was reduced to 2% from 2.7%, as reported in reference³. A Cl content of 1.71 ± 0.05 at.% and 1.20 ± 0.05 at.% in coatings containing an α/γ -Al₂O₃ phase mixture was observed. This process modification results in an increase of the coating density. Cross-sectional SEM micrographs of a coating consisting of an α/γ -Al₂O₃ phase mixture and a pure γ -Al₂O₃ coating grown on flat 1.2343 steel are shown in Fig. 6-6a and b, respectively. The measured surface roughness of γ -Al₂O₃ is 0.4 μm and 0.1 μm for the α/γ -Al₂O₃ phase mixture coating. The calculated deposition rate of γ -Al₂O₃ is 0.53 $\mu\text{m}/\text{h}$, which is significantly higher than that of the α/γ -Al₂O₃ phase mixture with 0.28 $\mu\text{m}/\text{h}$. The smooth surface with the low deposition rate observed in α/γ -Al₂O₃ phase mixture coatings is attributed to the intensified ion bombardment during deposition and an increased resputtering rate, consequently increasing the coating density by enhancing the adatom mobility⁵.

6.3.4 Performance in X35CrMo17 (1.2208) steel thixocasting

The performance of the PECVD alumina-coated tools was investigated at the Foundry Institute, RWTH Aachen University, in high pressure thixocasting experiments at ~ 1400 °C, using the high melting point steel X35CrMo17 (1.2208). This application has been selected since the load profile on forming moulds in semi-solid processing of steel are among the harshest in metal forming due to the

combined presence of the solid and the liquid phase. Detailed information on the experimental setup and process conditions are given elsewhere⁶.

The α/γ -Al₂O₃-coated tools were used as inserts in forming moulds for small-scale thixocasting series. During the forming processes, the coated tools were subjected to semi-solid steel at temperatures of ~1400 °C for 15-20 s. A detailed description of the test parameters is given in reference⁶. The main wear mechanisms in this application are erosive/abrasive caused by the solid steel fraction, and corrosive attack by the liquid fraction. Furthermore adhesion and abrasion were expected during ejection of the solidified part.

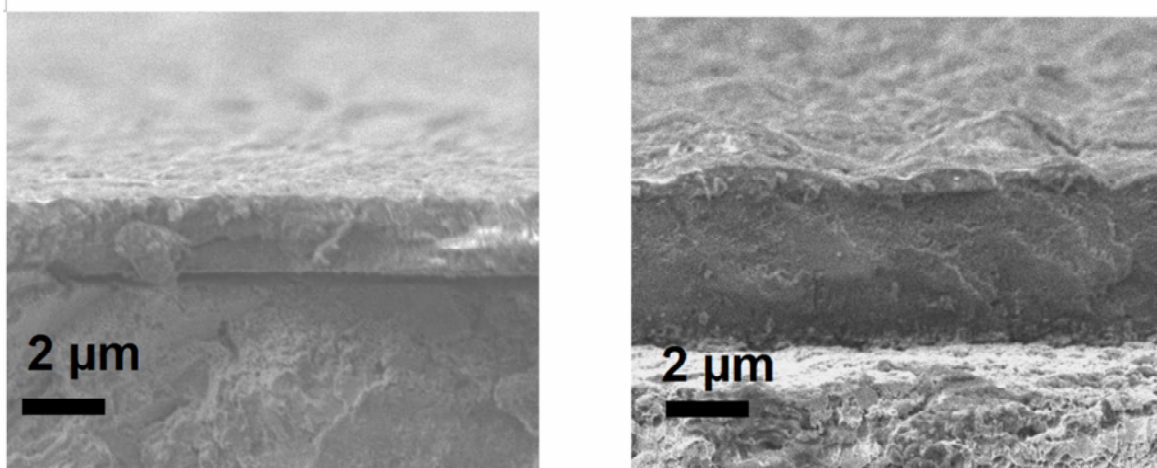


Fig. 6-6 Cross-sectional SEM images of (a) an α/γ -Al₂O₃ phase mixture and (b) a γ -Al₂O₃ coating grown on 1.2343 steel. The γ -Al₂O₃ coating was grown at pulse voltage of -750 V, pulse length of 150 μ s temperature of 590 °C. The mixture coating was grown at pulse voltage of -750 V, pulse length of 250 μ s temperature of 590 °C.

Fig. 6-7 shows a photograph of the mould surface after 10 thixocasting operations. No indications for large scale coating failure can be discovered. The coating remained intact. No delamination of the coating is observed. The nitriding treatment prior to coating deposition increased the Vickers hardness of the steel substrate from 200 to 800, providing efficient load support for the α/γ -Al₂O₃ mixture. Cross-sectional

SEM analyses of moulds after thixocasting reveal a coating thickness of ~3 μm. Also in this length scale no indications for adhesive or cohesive failure could be detected indicating that the coating remains intact, providing efficient protection during the thixocasting operations. In Fig. 6-8 X-ray diffraction data obtained from coated tools prior and after thixocasting provide no evidence for changes in the phase constitution as a consequence of casting.

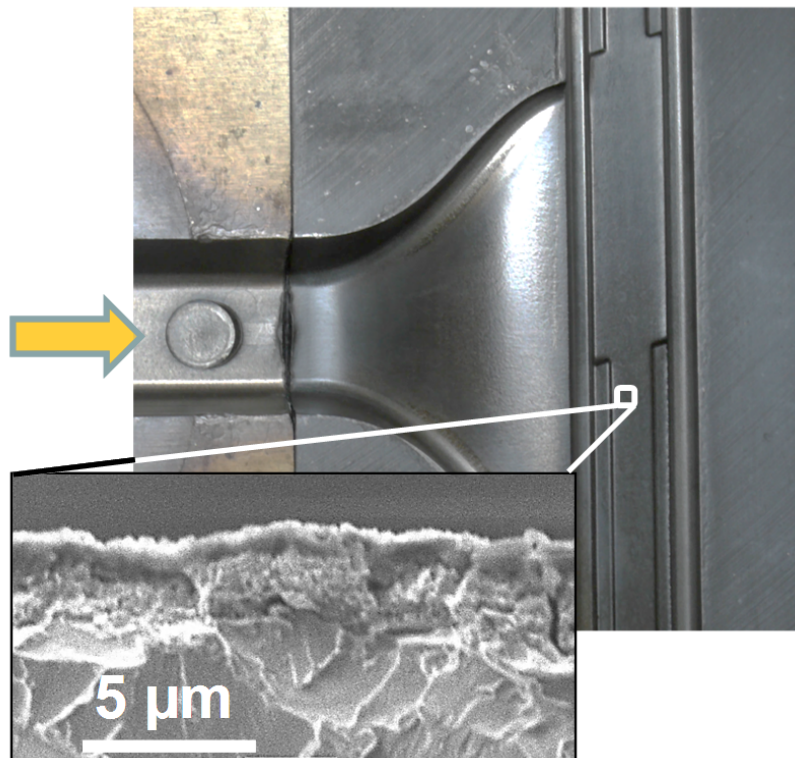


Fig. 6-7 α/γ -Al₂O₃ coated mould after 10 thixocasting operations at 1400 °C. The insert presents the cross-sectional SEM image of the marked position, where the intact coating with a thickness of ~3 μm can be seen.

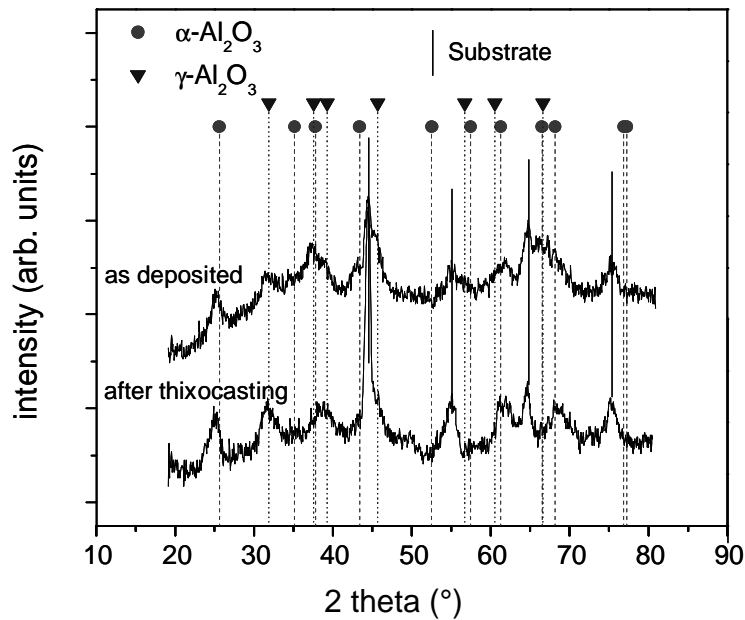


Fig. 6-8 X-ray diffraction data of the as deposited α/γ -Al₂O₃ coated mould and after thixocasting. The measured area corresponds to the region marked in Fig. 6-7.

6.4 Conclusions

An industrial-scale pulsed plasma-enhanced chemical vapor deposition (PECVD) process for crystalline alumina growth was developed. In contrast to the laboratory-scale process, our results indicate that the gas injection is of critical importance for the coating thickness distribution. By modifying the gas shower, in particular the outlet size and number, a coating thickness uniformity ($\pm 7\%$) was obtained at a flow density of $\rho = 1.14 \times 10^{-2}$ sccm/mm². A phase formation diagram for alumina coatings as a function of pulse length and cathode voltage has been compiled. Dense coatings with a comparatively low Cl-incorporation, consisting of an α/γ -Al₂O₃ phase mixture, were synthesized at substrate temperatures of 590 °C. Moulds coated with an α/γ -Al₂O₃ coating were employed in steel thixocasting operations at temperatures of ~1400 °C. The coatings were intact after casting. No evidence for adhesive or

cohesive failure of the coatings was obtained, indicating efficient protecting of the tools during thixocasting.

- ¹ S. Mokhtari, V. V. Kudriavtsev, M. Danna, in *The 1997 ASME pressure vessels and piping conference; Vol. 355*, edited by K. Karima Panahi (Orlando, Florida, 1997), p. 113.
- ² O. Kyrylov, D. Kurapov, J. M. Schneider, *Appl. Phys. A* **80**, 1657-1660 (2005).
- ³ R. Snyders, K. Jiang, D. Music, S. Konstantinidis, T. Markus, A. Reinholdt, J. Mayer, J. M. Schneider, *Surf. Coat. Technol.* **204**, 215-221 (2009).
- ⁴ D. Kurapov, J. Reiss, D. H. Trinh, L. Hultman, J. M. Schneider, *J. Vac. Sci. Technol. A* **25**, 831-836 (2007).
- ⁵ O. Auciello, R. Kelly, *Ion Bombardment Modification of Surfaces: Fundamentals and Applications* (Elsevier Science Ltd, Amsterdam, 1984).
- ⁶ M. Bünck, E. Subasic, A. Buhrig-Polaczek, K. Jiang, S. Munstermann, J. M. Schneider, K. Fickert, H. J. Gunther, *Steel Res. Int.* **81**, 581-588 (2010).

7 SUMMARY & FUTURE WORK

The goal of this work is to contribute towards the understanding of the synthesis-structure-properties (elastic and thermal) of vapor deposited alumina thin films, especially for those deposited using PECVD. Based on this understanding, new low temperature synthesis strategies may be defined. To achieve this goal, three tasks have been executed:

1. Investigation of the synthesis-property relationship of the PECVD grown Al_2O_3 thin films in order to obtain a dense $\alpha\text{-Al}_2\text{O}_3$ structure.

Various parameters for the PECVD process including precursor AlCl_3/O_2 ratio, pulse length, and power density were investigated. It has been shown that $\alpha\text{-Al}_2\text{O}_3$ is obtained at a low precursor ratio, long pulse length and high power density. These conditions allow for more efficient precursor dissociation as suggested by plasma OES data as well as for larger flux of bombarding ions. When these conditions are not fulfilled, $\gamma\text{-Al}_2\text{O}_3$ is formed. Due to the use of a chloridic precursor, the as deposited films contain Cl which may in turn significantly affect the film morphology and the phase formation. It is found that $\alpha\text{-Al}_2\text{O}_3$ films present a Cl content < 1.0 at.%, while $\gamma\text{-Al}_2\text{O}_3$ films contain ~ 2.0 at.% of residual Cl. The Knudsen desorption data indicate the notion of Cl migration at ~ 1000 °C and the *ab initio* data show that the agglomeration of two Cl atoms in the matrix results in an energetically more favorable configuration. These data suggest the Cl induced pore formation as presented in the

as deposited films. Applying a novel generator that allows for the operation of a PECVD discharge at approx. 4 times larger power density than those utilized conventionally, smooth and dense α -Al₂O₃ films with negligible Cl incorporation and elastic properties similar to those of the bulk α -Al₂O₃ are deposited at a growth temperature of 560 ± 10 °C.

2. Investigation of thermal stabilities of γ -Al₂O₃ thin films and bulk material

Both the annealing experiments and the DSC data suggest that the γ to α -Al₂O₃ transformation in the PECVD films is faster and occurs at lower temperatures in comparison to the FCA films. This could be due to the porous structure of the PECVD grown films which enhance diffusion processes during the phase transformation. The porous structure of PECVD films further enables the oxidation of a TiAlN interlayer and extrusion of TiO₂ towards the film surface due to large volume expansion from TiO₂, leading to a complete failure of the coating system.

The relative stability of γ -Al₂O₃ with respect to α -Al₂O₃ with 2.5 at.% of Si, Cr, Ti, Sc, and Y additives is also explored using *ab initio* calculations, indicating that Si stabilizes γ -Al₂O₃, while Cr stabilizes α -Al₂O₃. This explains electronic structure changes induced by the alloying element. As Si is added, a bond length increase in α -Al₂O₃ is observed, while strong and short Si-O bonds are formed in γ -Al₂O₃, consequently stabilizing this phase. On the other hand, Cr additions induce a smaller bond length increase in α -Al₂O₃ than in γ -Al₂O₃, therefore stabilizing the α -phase.

3. Up-scaling of a low temperature PECVD process

Up-scaling of lab-scale PECVD process to an industrial reactor has been successfully conducted allowing the growth of crystalline alumina on large thixocasting tools at substrate temperatures of 590 °C. Steel thixocasting operations on the coated moulds indicate that the coatings are intact after thixocasting. No

evidence for adhesive or cohesive failure of the coatings was obtained, indicating efficient protecting of the tools during thixocasting.

More studies should be done in order to address the exiting questions posed in this work. In the present work, the plasma composition was probed by OES analysis, which only offers qualitative information. Quantitative information as well as energy distribution functions are essential to understand the relationship between plasma properties and film growth. Therefore, mass spectrometry should be employed to study the dissociation of AlCl_3 molecular as well as Cl incorporation.

Based on the stability results from *ab initio* calculations, Si and Y alloyed $\gamma\text{-Al}_2\text{O}_3$ films should be grown to evaluate this design proposal by experimental investigating of the γ to α transformation thereof.

To investigate of the stability of $\gamma\text{-Al}_2\text{O}_3$ most studies have been done on commercial powders. However, the here presented results indicate a different transition sequence for thin films as compared to commercial powders. As the reason is unclear it may be interesting to investigate the role of free surfaces on the transition kinetics of metastable alumina.

Curriculum Vitae

Personal data

Name Kaiyun Jiang 蒋开云
Birth Nov. 05th, 1982, Ningbo, China
Nationality Chinese
Family married
Parents Decheng Jiang 蒋德成
Aiqin Qian 钱爱琴

Work

11/2010 - R&D Gebr. Schmid GmbH + Co., Freudenstadt,
now Engineer Germany

Education

09/2001 - Bachelor Materials Sci.& Tech. Eng., University of Sci. &
07/2005 Tech. Beijing (USTB), Beijing, China
10/2005 - Master Physical Metallurgy and Materials, RWTH
07/2007 Aachen University, Germany
08/2007 - Ph.D. Chair of Materials Chemistry, RWTH
10/2010 Candidate Aachen University, Germany

School

09/1990 - 07/1995 Hongxin Primary school, Shanghai
09/1995 - 07/1998 Baidu Middle School, Zhejiang
09/1998 - 07/2001 Fenghua No.1 High school, Zhejiang

Awards

07/2006 - 07/2007 RWTH Scholarship for International Master's
Students